

# **sBelle Design Study Report**

---

*Year 2008 Supplemental Update to the Detector LoI*

sBelle Design Group



## sBelle Design Study Report

I. Adachi,<sup>1</sup> M. Danilov,<sup>2</sup> K. Hara,<sup>3</sup> T. Hara,<sup>4</sup> T. Higuchi,<sup>1</sup> K. Inami,<sup>3</sup> H. Ishino,<sup>5</sup>  
 N. Katayama,<sup>1</sup> T. Kawasaki,<sup>6</sup> A. Kibayashi,<sup>1</sup> P. Križan,<sup>7,8</sup> P. Krokovny,<sup>1</sup> Y. Kuroki,<sup>4</sup>  
 A. Kuzmin,<sup>9</sup> I. Nakamura,<sup>1</sup> E. Nakano,<sup>10</sup> M. Nakao,<sup>1</sup> S. Nishida,<sup>1</sup> H. Ozaki,<sup>1</sup>  
 P. Pakhlov,<sup>2</sup> R. Pestotnik,<sup>8</sup> Y. Sakai,<sup>1</sup> C. Schwanda,<sup>11</sup> S. Shinomiya,<sup>4</sup> K. Sumisawa,<sup>1</sup>  
 O. Tajima,<sup>1</sup> K. Trabelsi,<sup>1</sup> T. Tsuboyama,<sup>1</sup> S. Uehara,<sup>1</sup> S. Uno,<sup>1</sup> and Y. Ushiroda<sup>1</sup>

<sup>1</sup>*High Energy Accelerator Research Organization (KEK), Tsukuba*

<sup>2</sup>*Institute for Theoretical and Experimental Physics, Moscow*

<sup>3</sup>*Nagoya University, Nagoya*

<sup>4</sup>*Osaka University, Osaka*

<sup>5</sup>*Tokyo Institute of Technology, Tokyo*

<sup>6</sup>*Niigata University, Niigata*

<sup>7</sup>*University of Ljubljana, Ljubljana*

<sup>8</sup>*J. Stefan Institute, Ljubljana*

<sup>9</sup>*Budker Institute of Nuclear Physics, Novosibirsk*

<sup>10</sup>*Osaka City University, Osaka*

<sup>11</sup>*Institute of High Energy Physics, Vienna*

### Abstract

In this note, we compile results of various simulation studies for the upgrade of the Belle detector. Based on these studies, we propose a set of optimum or appropriate parameters for the detector.

## Contents

<b>I. Introduction</b>	1
<b>II. Expected beam background</b>	2
A. Origins of beam-induced backgrounds	2
B. Background composition for the present KEKB / Belle	3
C. Machine parameters for each stage of the upgrade	5
D. Simulation study of the radiative Bhabha background contributions	6
E. Trends in the background levels	6
<b>III. Baseline Design</b>	11
A. SVD	11
B. CDC	13
C. PID	14
D. ECL	17
E. KLM	18
<b>IV. SVD performance</b>	20
A. Inner radius and resolution	20
B. Beam background effect on the readout chip	22
C. Outer radius and $K_S^0$ vertex reconstruction efficiency	24
D. S/N ratio and track matching efficiency	28
E. Readout pitch of outer layers	31
F. Slant angle	35
G. Summary of recommendations for SVD	37
<b>V. CDC performance</b>	39
A. Tracking efficiency and mass resolution	39
1. Result for $B^0 \rightarrow J/\psi K_S^0$	40
2. Result for $B^0 \rightarrow D^{*+} D^{*-}$	41
B. Summary of CDC performance	42
<b>VI. PID performance</b>	43
A. TOP counter	43
1. Overview	43
2. GaAsP photocathode	43
3. Focusing system	45
4. TOP configurations	47
5. $\phi$ coverage	47
B. Aerogel RICH Performance	48
C. Impact on $B \rightarrow \rho\gamma$ analysis	50
1. TOP and ARICH performance with the simulator	50
2. Luminosity gain in $B \rightarrow \rho\gamma$	51
<b>VII. ECL performance</b>	57
A. Partition of endcaps	57
B. Study of $B \rightarrow K_S^0 \pi^0 \gamma$ decays	58

C. Full reconstruction of $B$	58
<b>VIII. <math>K_L^0</math> reconstruction</b>	62
A. Impact of $K_L^0$ reconstruction improvement to $B \rightarrow \tau\nu$	62
B. Possibility of $K_L^0$ reconstruction improvement	62
C. Summary	64
<b>IX. Material effects</b>	65
A. Track and vertex reconstruction	65
1. Tracking Performance	66
2. Vertexing Performance	68
3. Effect of the additional layers	72
B. Calorimetry	73
<b>X. Beam Energy Asymmetry</b>	76
A. $B^0 \rightarrow \phi K_S^0$ and the beam energy asymmetry	76
B. $B \rightarrow \tau\nu$ and the beam energy asymmetry	77
C. Summary of the beam energy asymmetry studies	77
<b>XI. Closing Remarks</b>	79
<b>References</b>	79

## I. INTRODUCTION

The long awaited upgrade of Belle, which is referred to as sBelle<sup>1</sup> in this note, has become increasingly realistic and is very likely to happen in the near future. We have proposed a set of detectors in the Letter of Intent (LoI) [1] in 2003, which should work in the harsh beam background environment of the upgraded KEKB collider. Since the LoI, we have continued the R&D studies mainly in hardware in order to realize such a detector. As the design becomes more realistic and more concrete, we found several open questions concerning the parameters of the detector design.

Indeed, there will be several possible parameters such as geometry, structure materials, fundamental performance of sensors; and there is room to improve the overall performance by finding the best set of parameters. When the best set is not feasible either technologically or financially, we may need to compromise to some extent. In such a case, we must understand what will result. Finally, we require that the minimal performance of the new detector be at least as good as that of Belle, which is not very conservative because of the extremely harsh beam background.

In May 2007, a task force was formed to lead such discussions in a scientific way, and make proposals for the detector parameters from the viewpoint of physics analysis. The task force was asked to prepare a report of its studies in one year, which is the present report. Since we do not have an integrated simulation software tool for sBelle (one is under development based on Geant 4 and will require some more time to be ready), we began by preparing the simulation environments. One powerful tool is the Belle Geant 3 based full simulator (gsim) in which the parameters such as sensor configurations, material densities, and background immunities are modified to represent the sBelle detector. Another tool is a fast simulator called fsim6 [2], which gives detector responses based on a priori probability density functions; where the PDFs are retuned for sBelle. In addition, there are standalone Geant 4 simulators for certain sub-detectors, and a simple track simulator named trackerr. Using those tools we simulated events of various complexity, from simple single tracks to full  $B\bar{B}$  and  $\tau^+\tau^-$  events in which the real background data obtained from Belle can be overlaid to simulate the level of expected conditions at sBelle.

Benchmark physics modes in this report are selected mainly because of their importance in the sBelle era and sensitivity to the detector parameters to be examined, but also because analysis code and the person in charge were available. In spite of very limited manpower, we included the following important modes in this report:  $B^0 \rightarrow \phi K^0$ ,  $B^0 \rightarrow K_S^0 \pi^0 \gamma$ ,  $\tau \rightarrow \mu \gamma$ ,  $B \rightarrow \tau \nu$ , and  $B \rightarrow \rho \gamma$ . Studies of other decay modes that are underway will be compiled in a special report.

In the following sections, we first discuss the beam background (section II), then we recapitulate the design of the sBelle detector that we consider as the baseline (section III), and present the studies done for each sub-detector (IV to VIII). Specially added are sections about the effect of the detector material IX and the beam energy asymmetry X that are the key parameters in the overall consideration of the detector.

---

<sup>1</sup> The name of the new collaboration/detector has not been determined as we write this document. 'sBelle' is not an authorized name, but will be used for simplicity in this report.

## II. EXPECTED BEAM BACKGROUND

In the forthcoming KEKB upgrade, the luminosity will be improved by increasing the number of bunches and the beam currents, and by optimizing the beam optics in the interaction region (IR) as will be discussed in section II C. Some of these changes will also increase the level of the beam-induced background for the sBelle detector. A realistic estimation of the beam-induced background level compared to the present level is important for the new detector design. By estimating the occupancy, the radiation damage and the dead time for each sub-detector, we will be able to deduce the impact of the beam-induced background on physics analyses. Note that all these analyses have to be updated once more when we fix the design of the interaction region.

### A. Origins of beam-induced backgrounds

We can divide the beam-induced background into five types according to its origin: scattering of the beam on residual gas<sup>2</sup>, Touschek scattering, synchrotron radiation (SR) from the high energy ring (HER) upstream direction, backscattering of SR from HER downstream and those from electron-positron interactions at the interaction point (IP). A brief explanation for each of them follows (details can be found in the LoI [1]).

*a. Beam-Gas* Beam-gas scattering (bremsstrahlung and Coulomb scattering) changes the momenta of beam particles, which then hit the walls of vacuum chambers and magnets. The shower particles then produced are the main source of the beam-induced background. This component is proportional to the product  $I \times P$ , where  $I$  is the beam current and  $P$  is the pressure in the ring.

*b. Touschek* Touschek scattering is intra-bunch scattering. This type of background is proportional to the bunch current and the number of bunches, and inversely proportional to the beam size. The contribution from the HER can be ignored, because the rate of Touschek scattering is proportional to  $E^{-3}$ , where  $E$  is the beam energy, and also to the bunch current density, which is less than in the LER because the HER current is smaller than the low energy ring (LER) current.

*c. SR from upstream (SR Upstream)* Since the energy of radiation is in the keV range, the contribution from SR is negligible except for the innermost detector, the vertex detector. The level of this type of background is proportional to the HER current. It also depends on various parameters, magnet positions, bending radii and beam orbits. However, as a rough estimate, we can assume that the intensity is proportional to the HER current. The SR power is proportional to  $E^2 B^2$ , where  $E$  is the beam energy and  $B$  is the magnetic field strength [3]. The power is lower for the LER as  $E$  is smaller and  $B$  is designed to be smaller in our case. The net contribution from the LER is negligible in the present IR configuration. Careful simulation studies both for the HER and the LER will be performed for the upgraded IR.

*d. Backscattering of SR from downstream (SR Backscattering)* The final focusing magnet for the HER downstream side is called 'QCS-R', where R stands for the right hand side in the schematic drawing. The magnet QCS-R provides the final focusing of the LER beam. It also works as a bending magnet to separate the outgoing HER beam from the LER beam. Strong SR is emitted because of this bending. This SR hits the downstream chamber, which is  $\sim 9$  m away from the IP, then it backscatters in the detector again through the IP region. Careful simulation studies both for the HER and the LER will also be performed for the backscattering component.

---

<sup>2</sup> In what follows, we will use the expression 'beam-gas scattering' or just 'beam-gas' for this kind of scattering.

*e. Radiative Bhabha scattering* The rate of the radiative Bhabha events is proportional to the luminosity. Photons from the radiative Bhabha scattering propagate along the beam axis direction and interact with the iron of the magnets. In these interactions, neutrons are copiously produced via the giant photo-nuclear resonance mechanism [3]. These neutrons are the main background source for the outer-most detector, the  $K_L$  and muon detector (KLM) in the instrumented return yoke of the spectrometer. Figure 1 shows the measured radiation levels along the beam lines in the HER downstream of the Belle detector. It indicates that neutrons are generated along the beam lines within 11 m from the IP.

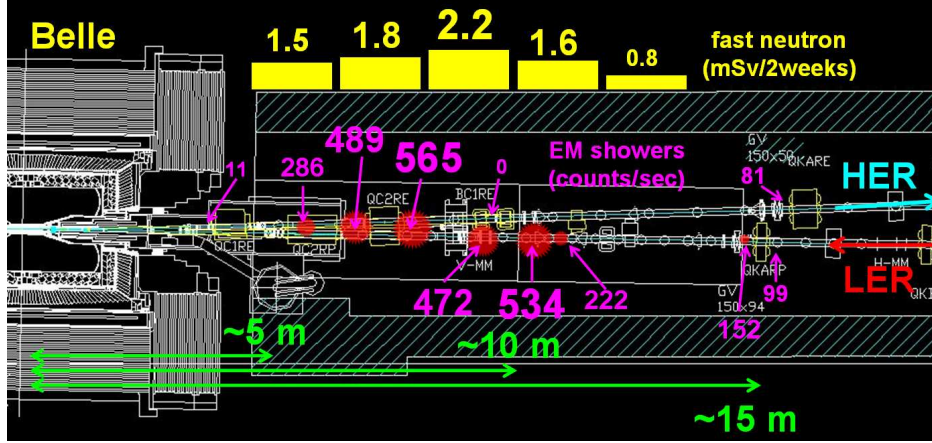


FIG. 1: Measured radiation levels around the beam lines in the HER downstream of the Belle detector. Neutron dose rates were measured outside of the concrete shield in 2003. The electromagnetic (EM) shower rates were measured with a scintillation counter in the same year. The position resolution of a movable EM shower counter is a 150 mm diameter circle along the beam lines; the counter is surrounded by a 200 mm thick lead shield and has a window diameter of 20 mm.

In addition, in the radiative Bhabha events both electron and positron energies decrease. The scattered particles are therefore over-bent by the QCS magnets and hit the wall of magnets where electromagnetic showers are generated. In the present Belle spectrometer, this type of background has not been observed yet. However, it is expected that the level of this kind of background will increase in the upgraded KEKB collider because of the considerably different interaction region design. A simulation study for this background is described in section II D.

## B. Background composition for the present KEKB / Belle

The relative contributions of background components are summarized in Table I for the case of the present configuration. Here, SVD-A (B) means inner (outer) side of the SVD sensors with respect to the KEKB rings. This table is based on various background studies described in the LoI [1]. We have observed a background contribution originating from radiative Bhabhas only in the KLM; for other sub-detectors, the contributions are estimated by Monte Carlo (MC) studies as will be described in subsection II D.



TABLE I: Relative contributions for individual detector components in the present KEKB / Belle

	SVD ( $A$ , $B$ )	CDC	PID	ECL	KLM ( $Barrel$ , $E.C.-Fwd$ , $E.C.-Bwd$ )
Beam-Gas (HER)	0.56 , 0.42	0.25	0.45	0.40	0.15 , 0.00 , 0.25
(LER)	0.20 , 0.13	0.40	0.40	0.40	0.12 , 0.20 , 0.00
Touschek	0.04 , 0.03	0.10	0.10	0.10	0.03 , 0.05 , 0.00
SR Backscattering	0.18 , 0.40	0.24	–	–	–
SR Upstream	0.02 , 0.02	–	–	–	–
Radiative Bhabha	–	0.01	0.05	0.10	0.70 , 0.75 , 0.75

### C. Machine parameters for each stage of the upgrade

The machine parameters that are used for the estimation of the beam-induced background are summarized in Table II for each stage of the upgrade: present collider (labeled as '200X'), initial stage of the upgrade (labeled as '201X') and ultimate stage of the upgrade (labeled as '202X'). They are based on the previous LoI [1] design and recent discussions with the KEKB upgrade design group. In the '201X' version, the luminosity improvement will be achieved by reducing the value of the  $\beta$  function at the IP, by reducing the electron cloud density in the beam pipe, and by making use of a crab crossing. In this first stage, the beam currents will not be increased significantly, but we will increase the number of bunches in the storage ring aiming to increase the beam currents at a later stage. To reduce the electron cloud density and residual gas pressure in the beam pipe, all vacuum chambers will be replaced and equipped with ante-chambers<sup>3</sup>. Note that the increase of the pressure in the ring is related to the increase in SR power; in the initial stage of operation, this effect is enhanced because the vacuum chambers will not yet be degassed well.

In order to reduce the value of the  $\beta$  function, the position of the focusing magnets will be changed. A smaller horizontal beam size at the IP requires a larger beam size in its immediate vicinity near the IR, and this, in turn, requires larger focusing magnets (QC1 and QC2 in Fig. 2). Since, in addition, the two beams must be well separated to avoid the influence of the magnets of one of the beams on the other beam, the beam crossing angle has to be increased from 22 mrad to 30 mrad. Due to these modifications, the critical energy of SR in QCS-R will almost double ( $\sim 40$  keV); we need to consider a better IR configuration so that the SR fan does not hit the components near the IR.

TABLE II: Assumed machine parameters for beam-induced background estimation.

	200X	201X	202X
$E$ : Beam Energy (GeV; HER / LER)	8.0 / 3.5	8.0 / 3.5	8.0 / 3.5
$I$ : Beam Current (A; HER / LER)	1.2 / 1.6	1.4 / 2.6	4.1 / 9.4
$N$ : Number of Bunches	1300	5000	5000
$i$ : Bunch Current for LER (mA)	1.2	0.5	1.9
$l$ : Bunch length (mm)	7	3	3
$\sigma$ : Beam Size in the Ring (scale factor)	1	1	1
$\theta$ : Beam crossing angle (mrad)	22	30	30
$W$ : Power of SR from QCS-R (kW)	30	61	179
$P$ : Pressure in the Ring ( $\times 10^{-7}$ Pa)	1.25	3.0	5.0
$L$ : Peak Luminosity (/nb/sec)	17	100	500

We estimate how much more background the sBelle detector will receive for each component during each run period based on the machine parameters summarized in Table II and following the formulae listed in Table III. The results are summarized in Table III. We observe that the background level increases predominantly due to the increase of the beam currents.

<sup>3</sup> Ante-chambers will also help to dispose of high power SR as heat.

TABLE III: Background scale factors normalized to '200X'.

	Scaling Formula	201X	202X
Beam-Gas (HER)	$I \times P$	3	14
(LER)	$I \times P$	4	24
Touschek	$N \times i \times i / (\sigma^2 \times l)$ uncertainty in dynamic aperture: 1 – 2	2 – 3	23 – 46
SR Backscattering	$W$	2	6
SR Upstream ( $r_{min} = 2.0$ cm)	$I$	1.2	3.4
( $r_{min} = 1.5$ cm)	<i>simulation</i>	14	40
Radiative Bhabha	$L$	6	30

#### D. Simulation study of the radiative Bhabha background contributions

In Fig. 2, the trajectories of electrons and positrons that have lower momenta than the momentum at the nominal beam orbit, and are hence over-bent by magnets, are shown for the cases of the present and upgraded designs. In the upgraded KEKB, both the rate and the energy of the showers from the over-bent particles are expected to increase, because of the larger crossing angle. The top-half view of the detector and QCS magnets are shown in Fig. 3. Over-bent particles hit the edge of the QCS magnets. The QCS magnets are located outside of the endcaps in the configuration of the present Belle and KEKB; most of the shower particles from QCS do not hit the detector. The QCS magnets will be located closer to the IP in the upgraded detector; hence the shower particles will tend to enter the detector volume.

This background source was studied by MC simulation. The over-bent electrons and positrons are generated by the MC simulator for radiative Bhabha scattering, BBBREM [4]. The development of electromagnetic showers of over-bent particles and the detector responses are simulated with Geant 4 [5]. In Fig. 4, the hit rate of CsI(Tl) calorimeter cells is plotted as a function of cell ID for the Belle and sBelle configurations. In the present configuration, the contribution from radiative Bhabhas is only around 4 % of the total background. It is difficult to observe such a small contribution in the real data. Indeed we have confirmed that there is no background component in the calorimeter that is proportional to the luminosity. On the other hand, radiative Bhabhas will be a serious background source in the new IR configuration. A solution to suppress its contribution is to place heavy metal shields inside and outside of the QCS magnets; the contribution can be suppressed to the same level as in the present configuration for the case of the same luminosity. Thus, we can simply extrapolate this background as a component proportional to the luminosity. The background rates on the backward side are an order of magnitude smaller than on the forward side as seen from Fig. 2; nevertheless, for safety reasons QCS-L will be shielded as well.

#### E. Trends in the background levels

The expected beam-induced background level for each detector is estimated from the scale factors (Table III), the relative contributions of components (Table I), and the assumed machine parameters (Table II). The estimated trend is shown in Fig. 5, which is based on the most conservative constant funding scenario with a very gradual increase in beam currents. Relative to the present values, we expect several to ten times higher background levels in the initial stage of

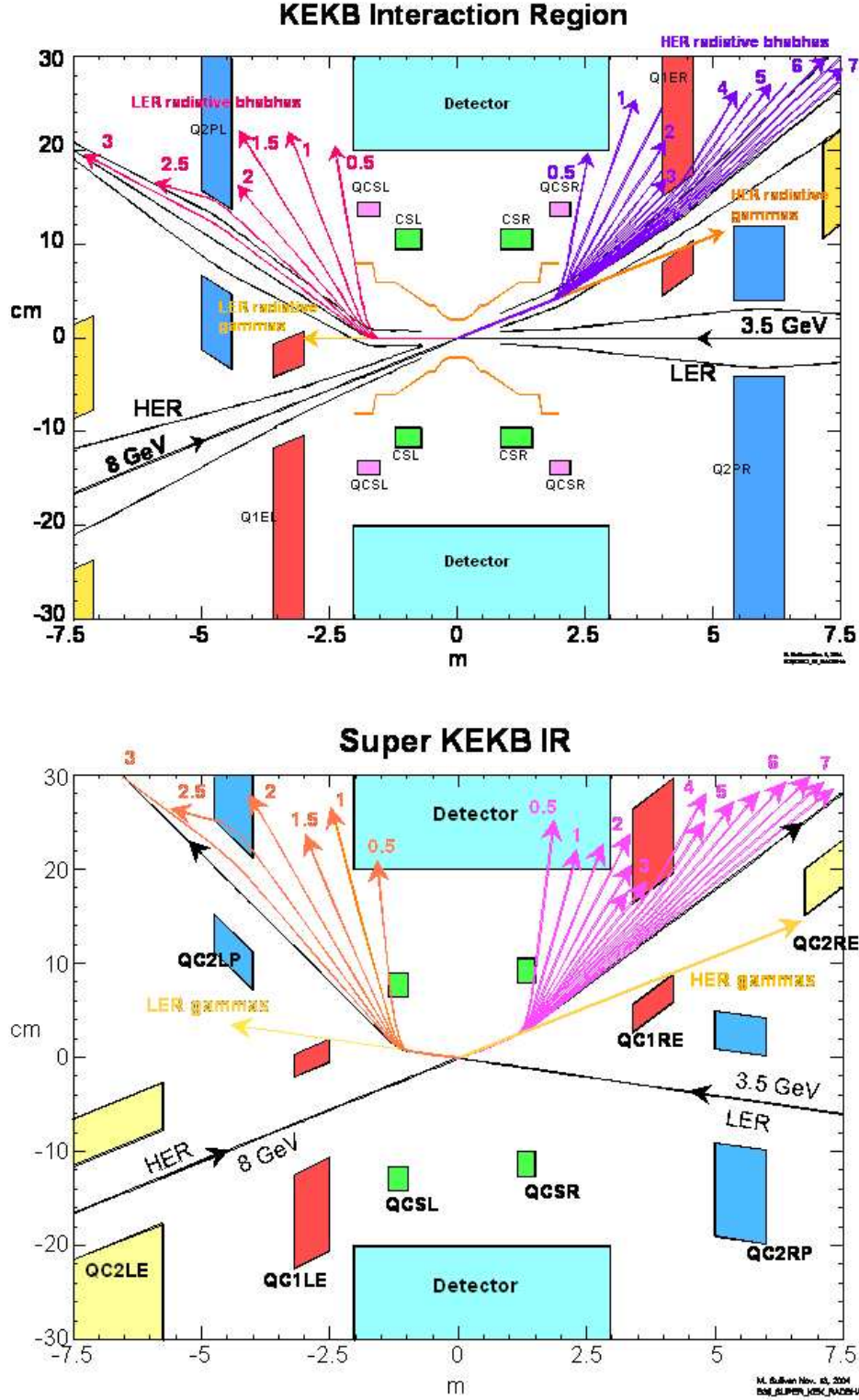


FIG. 2: Trajectories of electrons and positrons of radiative Bhabha events in the  $x - z$  view of the IR. Since their momenta are lower than those of the beams, those particles are over-bent by QCS magnets and enter into the detector volume. With the new IR design that has a larger beam crossing angle, high momentum particles from the HER, namely electrons by default, over 1 GeV can hit the walls of the magnets or the detector. This results in a background term proportional to luminosity.

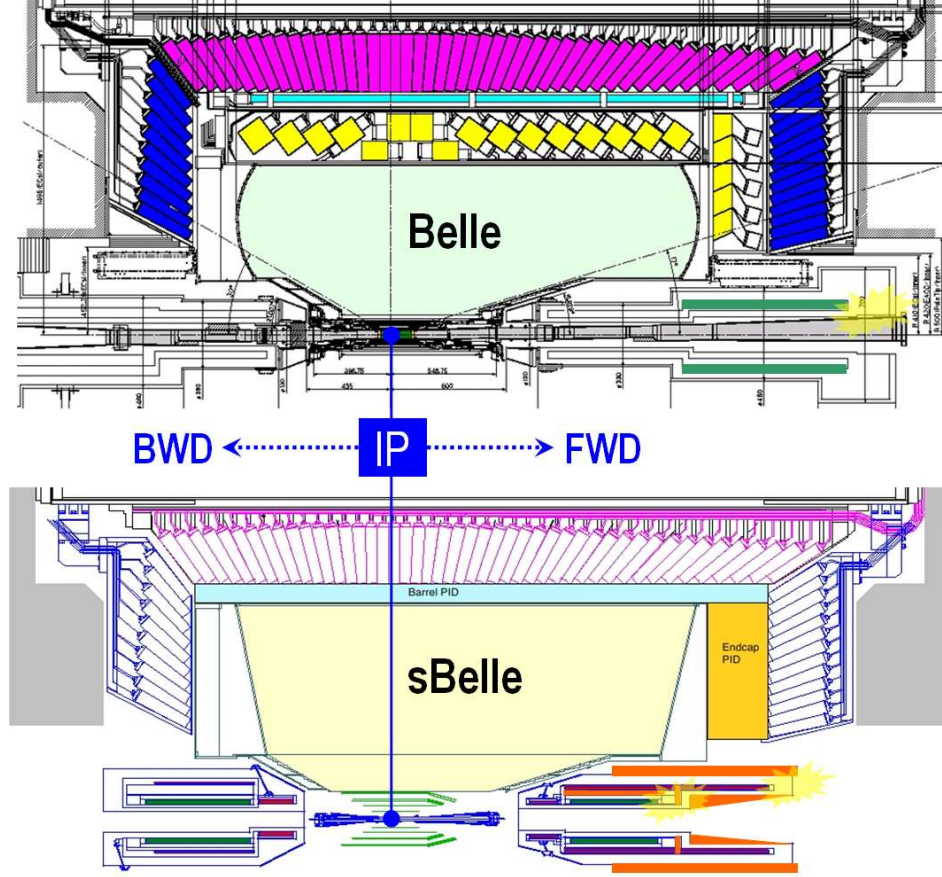


FIG. 3: Top-half views of the Belle with the present QCS configuration (upper) and the sBelle with the new QCS configuration (lower). The star marks indicate where the over-bent particles hit. In the upper configuration, most of the over-bent HER particles due to radiative Bhabha scattering hit the edge of the QCS magnet. On the other hand, most of the over-bent HER particles strike the inner edge of the QCS magnet due to the larger crossing angle in the lower configuration (sBelle).

the upgrade, and larger factors as the beam currents increase. Beam-gas scattering is the dominant background source for most detectors, while radiative Bhabhas are the dominant one for the KLM. General improvements of the beam-gas background from 2013 to 2018 are based on the additional assumption that the vacuum will improve with the degassing of the beam chambers.



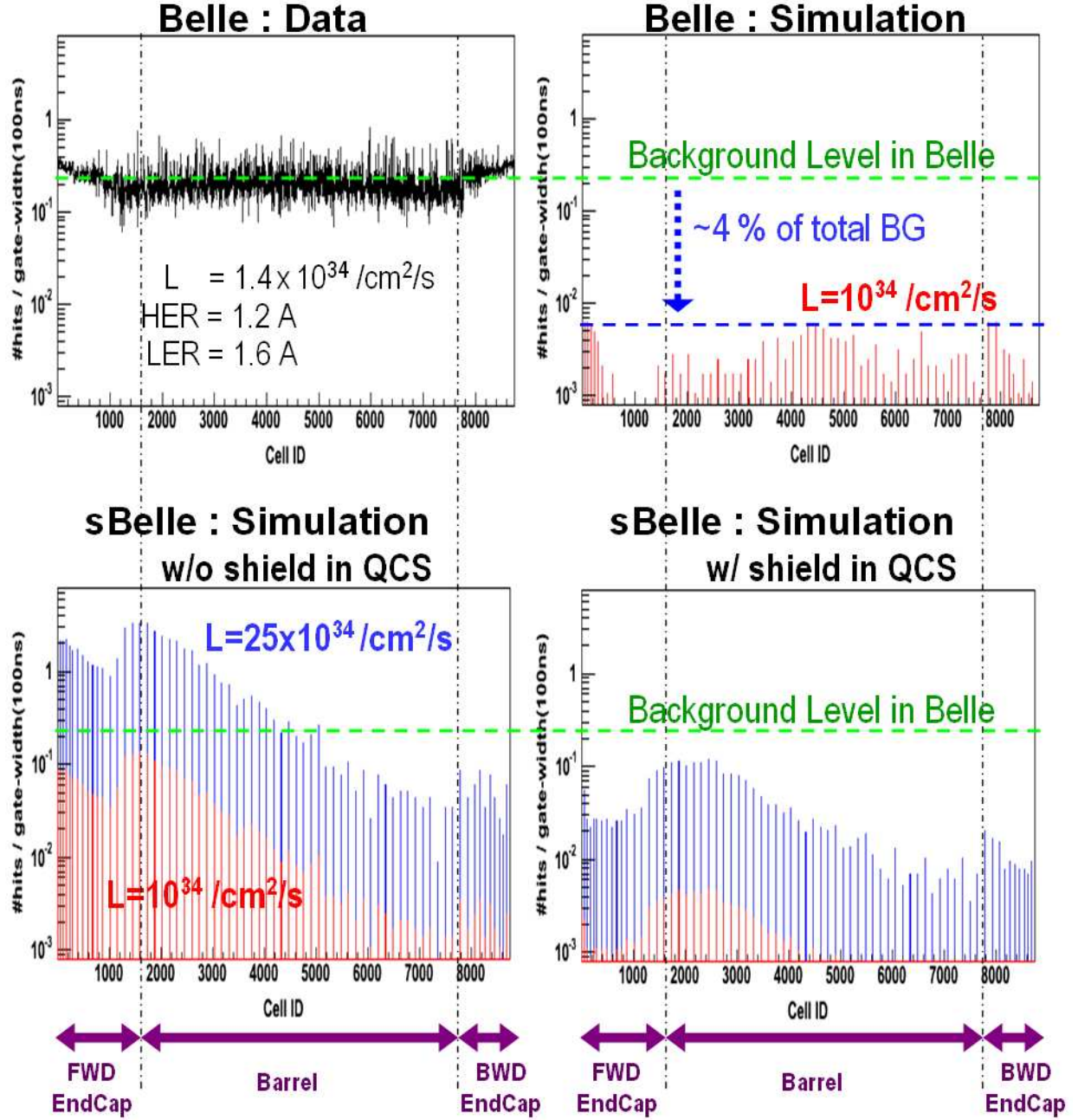


FIG. 4: Total background hit rate per CsI(Tl) calorimeter cell as a function of its ID number for the real data taken in experiment number 47, Dec. 2005 (upper left). The contribution from radiative Bhabha events is simulated based on the present IR configuration, assuming a luminosity of  $1 \times 10^{34} / \text{cm}^2/\text{s}$  (upper right). Lower two figures show simulation results for radiative Bhabha events based on the upgrade designs: without any shield material around the QCS magnets (lower left) and with heavy metal shields (lower right). We evaluate two luminosities  $1 \times 10^{34} / \text{cm}^2/\text{s}$  (red, or light-gray in grayscale) and  $25 \times 10^{34} / \text{cm}^2/\text{s}$  (blue, or gray in grayscale) in the lower plots.

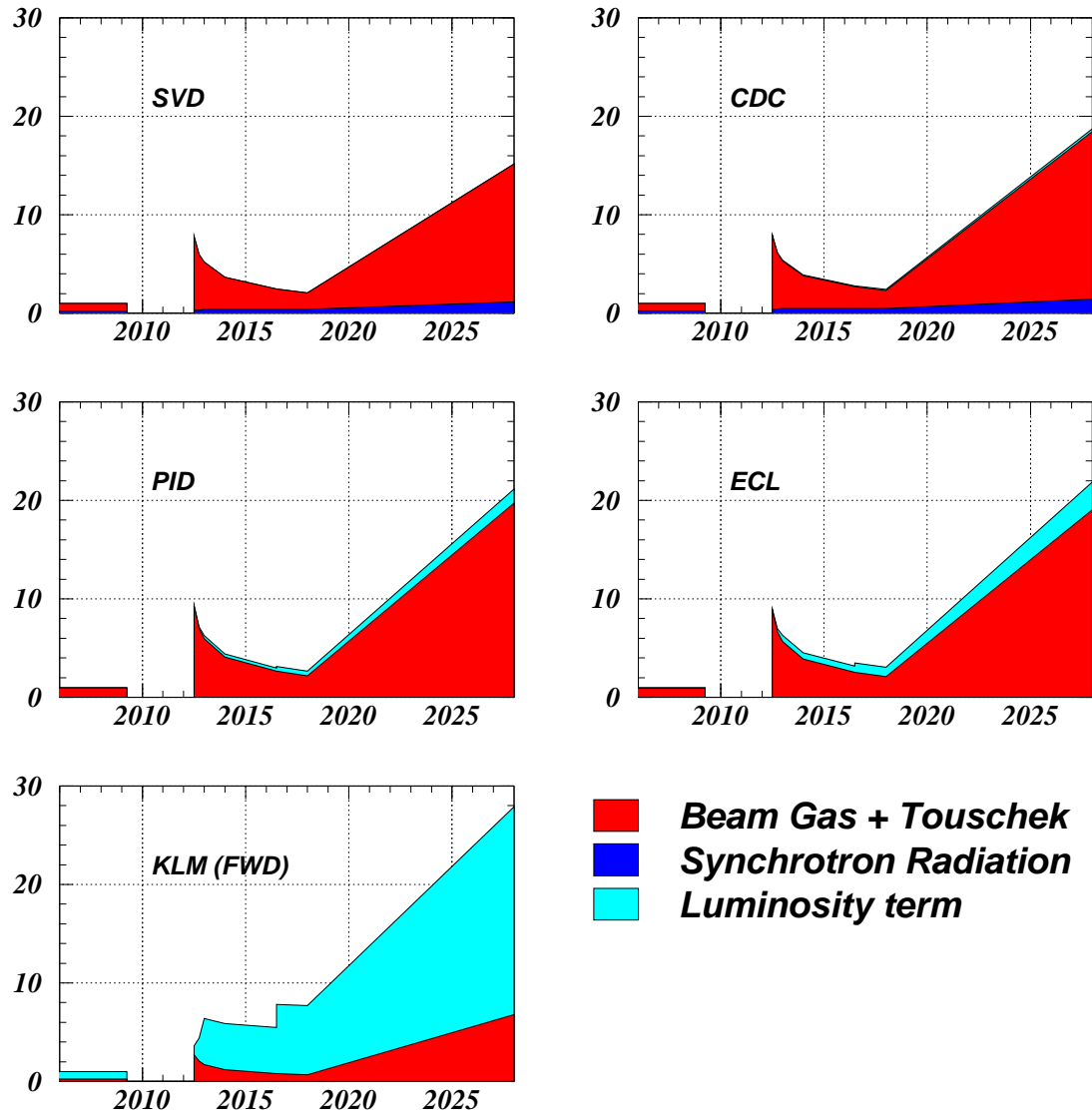


FIG. 5: Extrapolation of the beam-induced background levels for each detector normalized to the present level. Time scale is based on a modest assumption on how rapidly the beam currents increase. As indicated in the legend, beam-gas and Touschek scattering components are shown in red, radiative Bhabhas in light blue (brightest in grayscale), and SR in blue (darkest in grayscale).

### III. BASELINE DESIGN

The target detector of this study is the so-called *baseline* design, which is originally described in the Letter of Intent [1], and which is shown in Fig. 6 and includes some updates and minor changes made since then. We will have a 1.5 cm beam pipe and 6 layers of silicon vertex detectors (SVD) that consist of double-sided silicon strip sensors, a central drift chamber with about 15k sense wires (CDC), a time-of-propagation (TOP) counter as a particle identification device in the barrel, aerogel rich (A-RICH) counters in the forward endcap, thallium doped CsI crystals as an electromagnetic calorimeter (ECL), which will be partially replaced with pure CsI crystals in the endcaps, and a KLM based on resistive-plate-counters in the barrel and scintillators in the endcaps.

There are several other proposals for SVD and PID detectors; for example, we will include a pixel detector when it is ready, we may choose a DIRC or imaging TOP as the barrel PID. Whatever works can be a good candidate until we make a technical decision. The issues discussed in this report are, however, focused on the baseline design. This baseline design of each sub-detector is briefly summarized in the following subsections.

#### A. SVD

In the LoI that was released in 2004 [1], we have described a 6-layer SVD with a 1.0 cm radius beam pipe as a possible detector configuration. This design was proposed assuming operation at a luminosity of  $10^{36}/\text{cm}^2/\text{s}$ . In order to achieve a better impact parameter resolution, a smaller radius of the beam pipe was adopted at that time (1.5 cm for the current Belle detector). At the position of the innermost layer, the extrapolated beam background level is very large (shown in section II); it will reach  $\sim 5 \text{ MHz}/\text{cm}^2$  for beam-induced backgrounds above 10 keV at the full spec. Therefore we concluded that a pixel type sensor is necessary as the innermost layer to reduce the occupancy to an acceptable level ( $< 10\%$ ). Furthermore, this sensor should be as thin as a strip type sensor ( $\sim 300 \mu\text{m Si}$ ) to reduce the material budget. In terms of the readout time, this should be short to reduce the detector dead time. However we do not yet have a pixel sensor that fulfills these requirements<sup>4</sup>.

According to the present schedule for the sBelle, operation is anticipated to start in the middle of 2012. The primary target luminosity in the early stage is  $2 \times 10^{35}/\text{cm}^2/\text{s}$  (“201X” stage defined in section II) and we plan to gradually increase this up to  $10^{36}/\text{cm}^2/\text{s}$  (“202X” stage) within a few years. Because a detector upgrade takes three years according to our past experience, we should start the construction in 2009, that is, one year from now. Since we have to fix the detector configuration and technology choice immediately, we have decided our strategy for SVD upgrade as follows. For running in 2012, we will install an upgraded SVD with strip type sensors and a 1.5 cm radius beam pipe. A pixel sensor with a smaller radius beam pipe can replace the innermost layer as a further upgrade after a few years of operation. Following this new strategy, we propose in this report a new “baseline” SVD design for operation starting in 2012.

The specification of the baseline design is as follows. The radius of the beam pipe is 1.5 cm. As described in subsection V, the inner part of the present CDC cannot be operated at a higher luminosity because of the harsh beam background. Therefore we will replace this part with two additional SVD outer layers, which correspond to the fifth and sixth layers. The increased number of layers enables stand-alone tracking with the SVD and improves the tracking efficiency for

---

<sup>4</sup> DEPFET was not known as a candidate when we started this study.



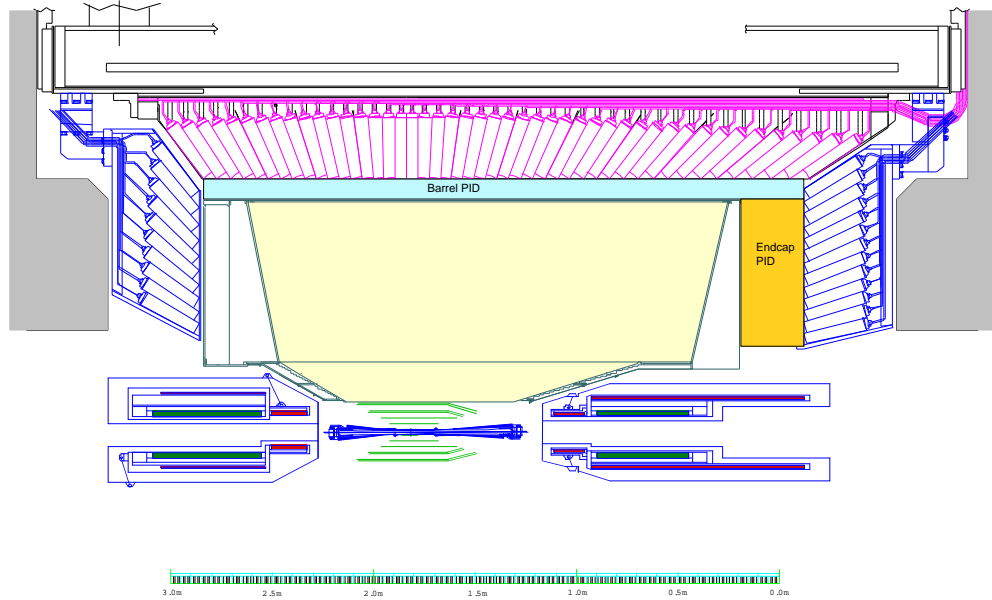
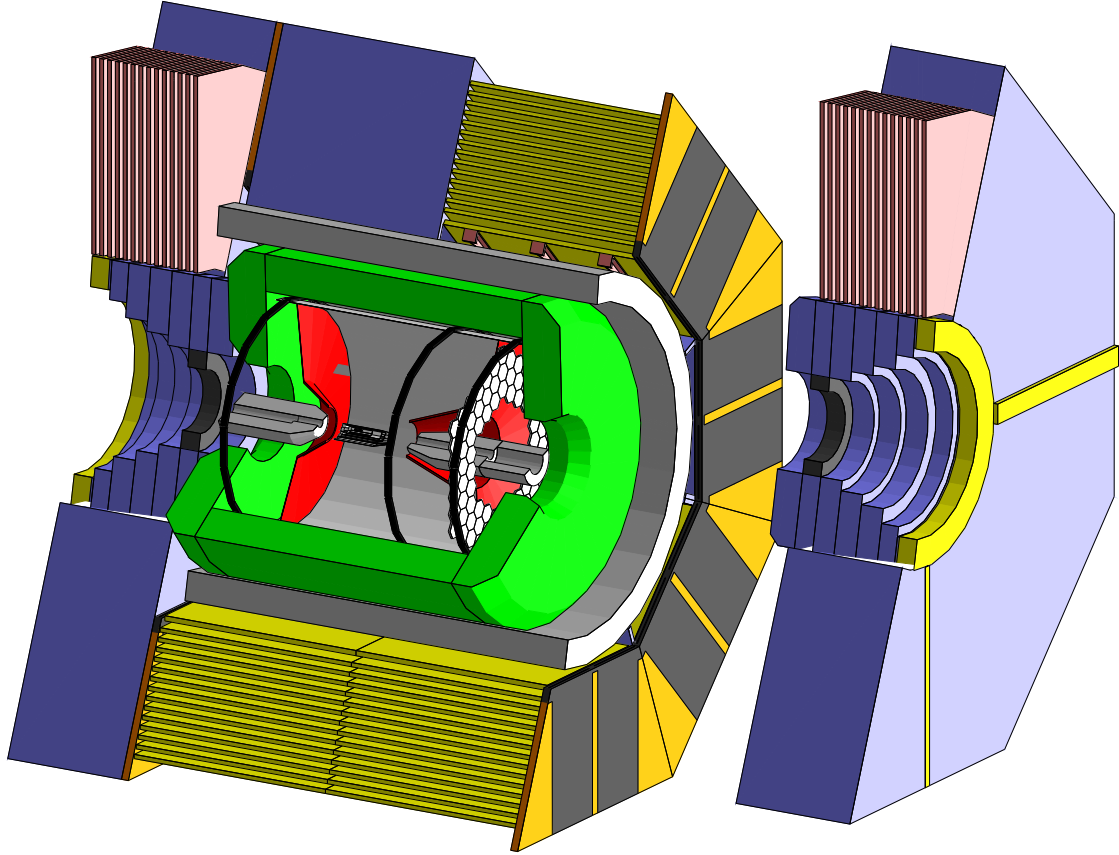


FIG. 6: Conceptual design of the sBelle detector in the LoI. The cross-sectional view of inner sub-detectors is shown in the bottom panel.

low momentum particles. Moreover, this enlarged SVD requires an increase in the efficiency for reconstructing  $K_S^0$  decays. However, this also leads to a longer sensor, especially for the outer layers. As a result, the noise level will increase. To cope with this, a development of a special readout scheme, for example the "chip-on-sensor" method, is needed to maintain a good S/N performance. Note, however, that this would increase the material budget in the acceptance. As for the forward and backward parts, the layers could be slanted or have a disk-type shape so that the ladder size and the number of readout channels can be reduced without losing acceptance.

The signals from a strip type sensor should be read out by a front-end chip, which has a short shaping time ( $\sim 50$  ns) to reduce the high occupancy induced by the harsh beam background. Since the L1 trigger rate would be very high ( $\sim 10$  kHz), a pipeline on the front-end chip is required. The VA chip, which has been used for the Belle SVD, cannot be used even at the outer layers since it needs at least  $12.8 \mu\text{s}$  to be read out and introduces a dead time fraction of more than 15% at the 10 kHz L1 trigger rate. The APV25 chip that has been developed for the CMS Si tracker fulfills the above requirements and is one possible solution.

In this design report, we will discuss these issues and make recommendations for the baseline SVD detector.

## B. CDC

The present CDC has been working well for 9 years starting from the beginning of the Belle experiment. It is used to reconstruct charged tracks with good momentum resolution due to its low mass, and hence reduced multiple scattering. It also provides particle identification based on the characteristic energy loss ( $dE/dx$ ). In addition, a powerful level 1 track trigger signal is generated with a latency of a few  $\mu\text{s}$ . All these features can only be achieved by using a small cell wire chamber filled with a helium based gas.

We want to maintain a similar performance level for the main tracking device in the sBelle detector. A new CDC detector should be designed to work under a beam background rate 20 times higher than the present level. The inner radius is increased to avoid the severe beam background environment in the region that will be covered with the new enlarged SVD. The outer radius is larger because the barrel part of the particle identification device will be thinner. The overall detector shape is similar to the present CDC with three parts, the main part, the conical part and the inner part. The main part is held between two curved 10 mm thick aluminum endplates, separated by about 2 m. The outer surface of the main part is a cylinder made of 5 mm thick carbon fiber reinforced plastic (CFRP). The conical part is necessary to extend the detector acceptance as much as possible in the forward direction, while allowing the KEKB machine components to be close to the IR. The inner part has 8 layers with small cells and a cylindrical inner surface made of 0.4 mm thick CFRP.

The wire configuration of the new CDC is shown in Fig. 7. The cell size will be smaller for the inner super layers to reduce the occupancy. More stereo layers should allow for an improved three-dimensional track reconstruction. For the sense wires as well as for the field wires, the same material and the same diameter used in the present CDC are selected. We will also keep the same gas mixture, because we have not encountered any problems such as radiation damage in the present CDC so far. Design details are described in the LoI [1].

New readout electronics should be used to reduce the dead time. This will be the most effective countermeasure against the expected high beam background. ASIC chips with a shorter shaping time will be used for signal amplification, shaping, and discrimination. The drift time and the pulse height are measured separately using pipelined TDCs and slow FADCs. The electronics

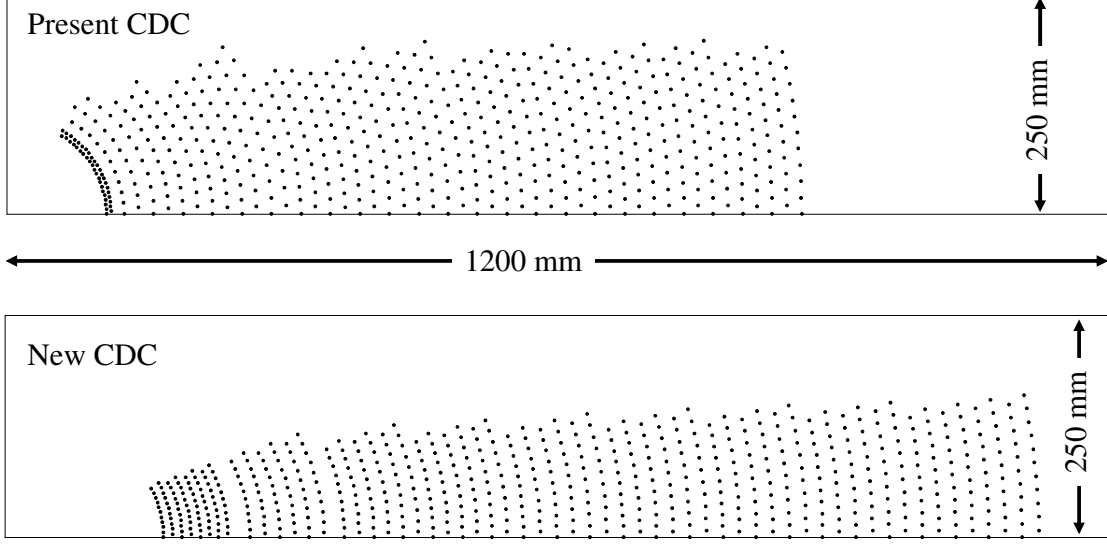


FIG. 7: Configurations of CDC sense wires in the present (top) and the upgraded (bottom) CDC.

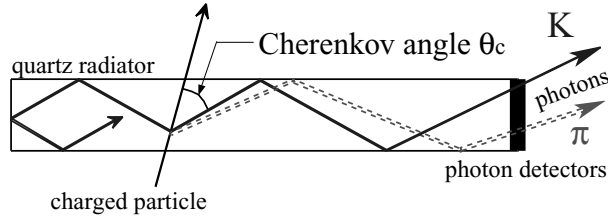


FIG. 8: Schematic side-view of TOP counter and internal reflecting Cherenkov photons.

components will be located near the backward endplate and all information will be transferred to the electronics hut through optical fibers.

### C. PID

To extend our physics reach, we would like to improve the  $K/\pi$  separation capability of the spectrometer by upgrading the particle identification (PID) system. An upgrade of the system is also compulsory to cope with the higher background environment. Another aspect to improve is to reduce the amount of material and make it more uniform since the PID system is located in front of the calorimeter.

At this moment, two types of detectors, both of which are based on the Cherenkov ring imaging technique, are proposed: a time-of-propagation (TOP) counter for the barrel region, and a proximity focusing Cherenkov ring imaging counter with aerogel radiators (ARICH) for the endcap region. The baseline design discussed in this report will be outlined below.

*f. TOP counter* In the barrel region of the spectrometer, the present time-of-flight and aerogel Cherenkov counters are replaced with a Time-Of-Propagation (TOP) counter [6]. In this counter the time of propagation of the Cherenkov photons internally reflected inside a quartz radiator is measured (Fig. 8). The Cherenkov image is reconstructed from the 2-dimensional information provided by one of the coordinates ( $x$ ) and precise timing, which is determined by micro-channel plate (MCP) PMTs at the end surfaces of the quartz bar. The array of quartz bars

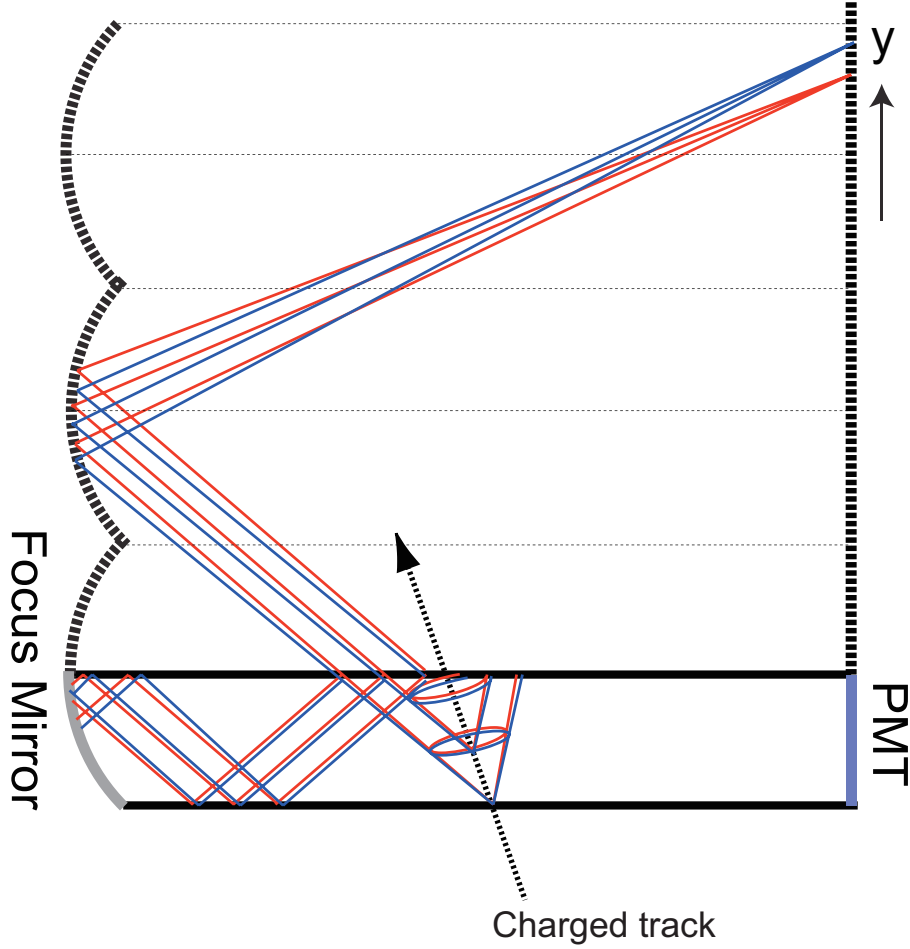


FIG. 9: The principle of the focusing scheme in the TOP counter. The virtual extension of the focal surface and of the photon detector plane are shown by the dashed curves and dashed lines.

surrounds the outer wall of the CDC; they are divided into 18 modules in  $\phi$  in the baseline geometry. In one module, in order to reduce the possible degradation due to chromatic dispersion, each radiator bar is subdivided into two pieces at  $z \sim 1070$  mm, where the “short” bar with 750 mm length is used for the forward side, and the “long” bar of 1850 mm length for the backward side. The short bar is instrumented by PMTs only at the forward side, while the long bar has PMTs at both sides.

To improve the performance, a “focusing scheme” is being considered (Fig. 9), in which the set of MCP-PMTs located at the forward side of the long bar at  $z \sim 1070$  mm is replaced by a focusing mirror (Fig. 10). The PMTs at the other end are rotated to determine the  $y$  coordinate in addition to the  $x$  position, which enables us to correct for the chromaticity of Cherenkov light as well as to measure the 3-dimensional information of emitted Cherenkov photons.

The present support structure for quartz bars occupies a small region in the  $\phi$  direction, which introduces an insensitive region. As will be discussed in Sect. VIA, this could be recovered by arranging two layers of radiators, where the inactive area in one radiator layer is covered with the other layer and vice versa.

*g. ARICH counter* The ARICH counter is located in front of the forward endcap calorimeter, in the region of the present forward endcap aerogel counter. Because of the limited space in

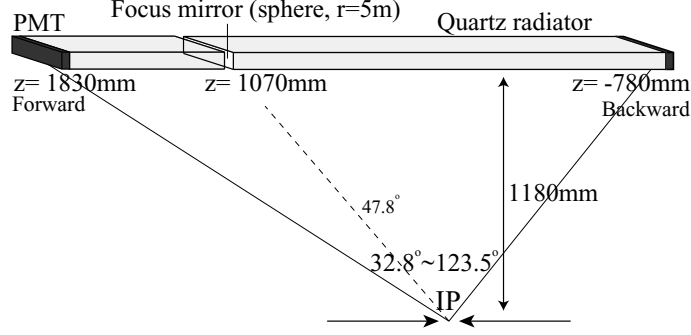


FIG. 10: Baseline design of the focusing type.

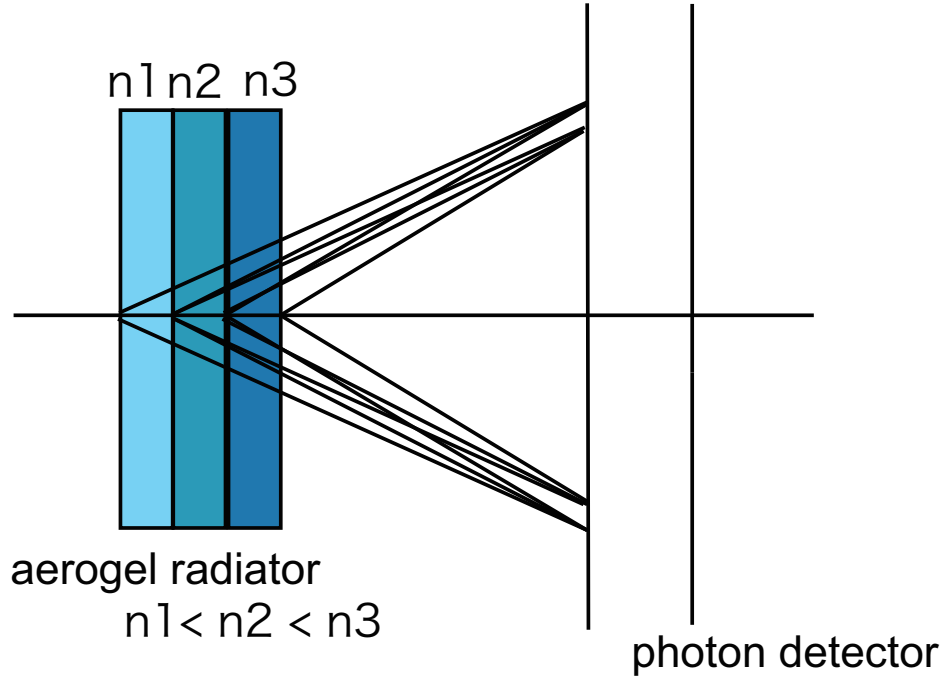


FIG. 11: A schematic view of ARICH counter with multiple aerogel radiators.

the Belle endcap layout, we employ a proximity focusing scheme, where the Cherenkov expansion distance is 200 mm. In the present design, 3 layers of silica aerogels, each 10 mm thick, with different refractive indices from 1.045 to 1.055 are used as Cherenkov radiators so that Cherenkov photons produce overlapped images on the photon detector surface, as shown in Fig. 11.

The photon detector, which has to detect efficiently single photons in the magnetic field of 1.5 T, has not been selected yet. One of the candidates is a hybrid avalanche photon detector (HAPD), where around 600 HAPDs, each of which has 68% active area, are aligned in 9 layers in the radial direction from an inner radius of 435 mm. Another choice for the photon detector is the MCP-PMT, which has an excellent timing resolution of  $\sim 50$  ps for single photons. This feature allows a time-of-flight measurement by using the Cherenkov photons from the entrance window of the MCP-PMT. With this additional information we could positively identify kaons with momenta below the Cherenkov threshold in aerogel ( $\approx 1.5$  GeV/c).

The boundary region between the barrel and the endcap is of concern as well, because this area

is used for the MCP-PMT mounting in the TOP counter, and in the ARICH counter Cherenkov photons emitted from the aerogel radiator tend to get lost because of detector acceptance (Fig. 12). This deterioration may be alleviated by installing a mirror at the outer wall of the ARICH counter in order to reflect photons back to the photon sensor active area. A potential drawback of this solution is that it may complicate the reconstruction of the ring images. This option is discussed in Sect. VIB.

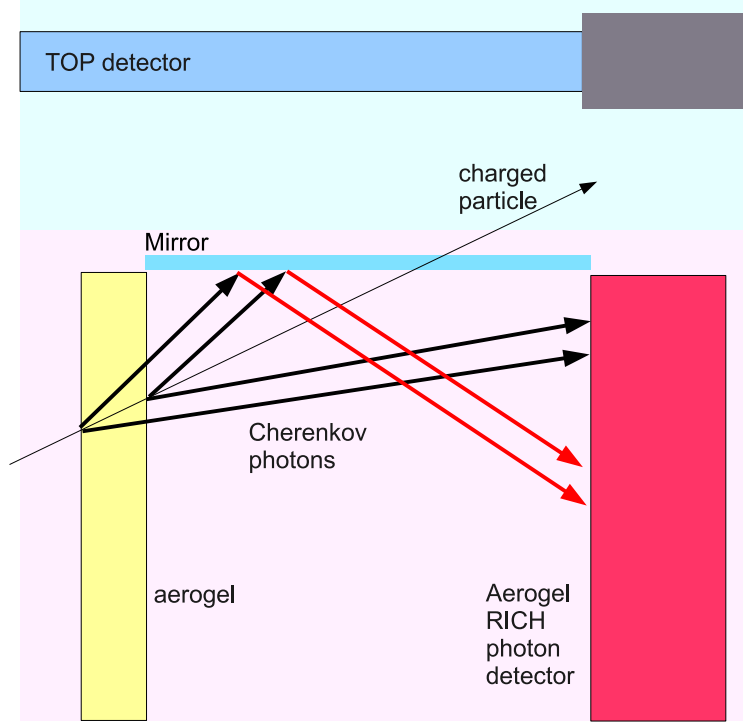


FIG. 12: Propagation of Cherenkov photons of a track hitting the aerogel radiator in the vicinity of the boundary to the barrel part, for the case with an additional planar mirror.

#### D. ECL

The main concern for the electromagnetic calorimeter (ECL) is the increase of background due to higher beam currents. The background in ECL will increase typically as a function of the total stored current multiplied by the pressure of the residual gas in the beam pipe. As the result, the background is expected to be an order of magnitude larger than at present as discussed in section II.

The basic idea is to replace the present read-out electronics with a relatively modern technology. In the new front-end electronics, waveform sampling will be implemented. The shaping time will also be shortened from  $1 \mu\text{sec}$  to  $0.5 \mu\text{sec}$ . The waveform is sampled with a  $\sim 2 \text{ MHz}$  sampling frequency. The sampled waveform is fitted in a FPGA to extract the amplitude (i.e., energy) and the timing, which allows us to separate physics signals and beam backgrounds. With the shorter shaping time and proper waveform analysis, the background is expected to be reduced by a factor of four to seven depending on the energy range.

The background rejection by the waveform analysis is limited by the slow ( $\sim 1 \mu\text{sec}$ ) scintillation light of the CsI(Tl). In order to further reduce the background, replacement of some CsI(Tl) crystals with faster ones is desirable. Pure CsI has a fast time constant of  $\sim 30 \text{ nsec}$ , 30 times shorter than CsI(Tl), while the light output is 50 to 100 times smaller. To detect the scintillation light from pure CsI, the photo-detector has to have sensitivities to UV light with a gain of 10 to 100 in a 1.5 T magnetic field, and has to be as short as a few cm long to fit into the current mechanical structure. Fine-mesh photomultipliers [7] with a small number of multiplication stages have a gain of more than 20 in 1.5 T field, and a length of about 5 cm. By replacing the crystals with pure CsI and with a proper waveform analysis, the background can be reduced by more than a factor of 100.

Initially, we will upgrade the read-out to do waveform fitting of the signals from the existing CsI(Tl) crystals, which is necessary from the very beginning of sBelle operation. We will also prepare pure CsI crystals and the corresponding read-out system for the endcaps by the time we reach a background level so high that we cannot handle it with waveform fitting alone. The performance of the ECL and the impact on physics analyses will be discussed in section VII. More details of the hardware issues are discussed in the LoI [1].

## E. KLM

The detection efficiency of Belle's resistive plate counters (RPCs) depends strongly on the ambient background rate. This is due to the long recovery time of the glass electrodes (resistivity  $\sim 10^{13} \Omega\cdot\text{cm}$ ) after the depletion of the charge in a spot near the streamer that forms in the gas volume upon its ionization by a primary particle. Neutrons make the dominant background here; the effect of  $\gamma$  rays is much smaller. The expected background rates at SuperKEKB situation are  $0.5 - 4 \text{ Hz/cm}^2$  for the barrel and  $2 - 5 \text{ Hz/cm}^2$  for the endcap. Because of the higher background rates in the endcap and the greater sensitivity of the endcap glass material, the estimated efficiency is 0% for the endcap in streamer-mode operation, and 90% or more ( $\sim 80\%$ ) in the outer (innermost) barrel layers.

In the barrel's inner-layer RPCs, a recovery to  $\sim 90\%$  efficiency may be achieved through various techniques. A shorter dead time can be achieved by a modified gas mixture. From our study using endcap-glass RPCs, the best gas mixture ( $\text{Ar/C}_4\text{H}_{10}/\text{HFC134a/SF}_6 = 50/8/37/5$ ) reduces the dead time by about a factor of three (to  $0.15 \text{ sec}\cdot\text{cm}^2$ ). However, there is a caveat: the current dead time of the barrel-glass RPCs ( $0.08 \text{ sec}\cdot\text{cm}^2$ ) is already shorter than this improved value, so the use of this new gas mixture in the inner-layer barrel RPCs may not result in as marked an improvement in efficiency. A more drastic measure to suppress the neutron background would be to replace the innermost RPC layer with a passive polyethylene absorber with a thickness of 4 cm. (This would increase slightly the threshold on transverse momentum of muons that reach the first sensitive barrel RPC layer.) By combining these options, the barrel-RPC efficiency degradation is expected to be a few %. If the actual background rate turns out to be much higher than the above estimates, the barrel RPCs will be operated in avalanche mode[8] rather than streamer mode. This will require a retrofit of an on-detector amplifier because of the small signal charge ( $\sim 1 \text{ pC}$ ).

In the sBelle endcaps, where the beam background effects are most deleterious, the RPCs will be replaced with a new and faster detector. In the proposed system [1] scintillator counters with wave-length-shifting (WLS) fiber readout are installed in the gaps between the iron absorber plates of the solenoid yoke. Each superlayer, contained within an existing RPC module's aluminum frame, is formed by two independent and orthogonal planes of scintillator strips. One quadrant of a scintillator superlayer is shown in Fig. 13.

Each strip has a cross section of  $1.0 \times 2.5 \text{ cm}^2$  and a length of up to 280 cm. The strip is extruded



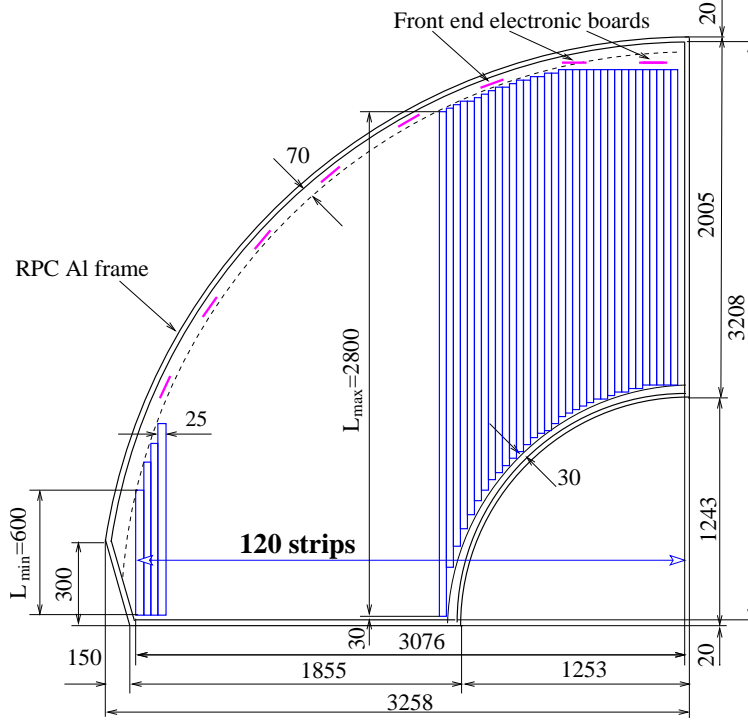


FIG. 13: Sketch of the scintillator-strip superlayer.

from granulated polystyrene with two dyes (PTP and POPOP) and covered by a diffraction reflector. The Kuraray multicladded WLS fiber Y11 (200) is installed in a groove at the strip's surface. To improve the light collection efficiency, the WLS fiber is glued into the groove with optical gel and the fiber and groove are covered by a Superradiant VN2000 foil. The Geiger Photo Diode (GPD) photodetector, produced by CPTA (Moscow) [9], is mounted at one end of the fiber; a mirror is placed at the other end. The GPD is a matrix of 560 tiny ( $40 \times 40 \mu m^2$ ) silicon photodiode pixels operating in Geiger mode. The signals from all pixels are internally summed to produce the GPD response. Signals with a distinct number of photoelectrons are well separated. The typical GPD amplification is about  $10^6$ . The product of quantum and geometrical efficiency is 25–30 % in the region near the WLS-fiber spectrum maximum. The radiation hardness of the GPD was measured directly in the KEKB tunnel and was found to be sufficient for the proposed system.

The GPD has a quite high single photoelectron noise rate of about 1–2 MHz at a room temperature. In order to reduce it to an acceptable level, it is necessary to impose a threshold of a few fired pixels. The dependence of the strip detection efficiency for a minimum-ionizing particle (MIP) on this GPD threshold has been studied using a cosmic ray trigger. The mean number of fired pixels per MIP is  $\sim 20$ , so a threshold of  $\sim 6$  fired pixels results in a MIP detection efficiency of as high as 99% with a suppression of the intrinsic GPD noise rate to less than 1 kHz. This GPD noise rate is much smaller than the rate due to the accelerator-induced neutron background. The latter is extrapolated to the SuperKEKB luminosity from our direct measurements with the test scintillator KLM module in the KEKB tunnel to be  $\simeq 100 \text{ Hz/cm}^2$ . For the longest strip, the expected rate is  $\sim 70 \text{ kHz}$ ; this does not reduce the MIP efficiency because of the very short GPD dead time.



## IV. SVD PERFORMANCE

As described in subsection III A, we have decided on the concept of the baseline SVD design, that is, a 1.5 cm radius beam pipe and a 6-layer SVD where all layers are constructed from strip type sensors. However, we still have many things to determine before finalizing the design.

One of the important issues is the front-end readout chip. At the target luminosity, the SVD will be exposed to harsh beam background. According to the estimation shown in section II, the beam background in the SVD could be about 15 times higher than the current Belle level. In this situation, the VA chip that has been used for the current SVD would not work at all because the rate at which beam background pulses overlap with the on-time signal pulses would increase drastically. To overcome this difficulty, we require a front-end chip whose shaping time is much shorter than that of the VA chip. Furthermore, the VA chip takes at least  $12.8 \mu\text{s}$  to be read out. The expected dead time fraction could then be more than 15% under the 10 kHz trigger rate that is anticipated in sBelle. Therefore, we need also a front-end chip that has a pipelined readout scheme.

Other issues are related to the configuration. As will be described in subsection V, the inner radius of the CDC will be enlarged to avoid the severe beam background. We will install two extra SVD layers in this space instead. Thanks to this, SVD stand-alone tracking will be available, and the reconstruction efficiency for  $K_s$  events will improve. However this requires longer sensors increasing the noise level. We should also be aware of further deterioration with a shorter shaping time since the intrinsic noise level is proportional to  $\sqrt{1/t}$ , where  $t$  is the shaping time. To maintain good noise performance, a special readout scheme must be developed, for example a “chip-on-sensor” method, is needed. However, this would increase the material budget in the acceptance and also the number of readout channels. One possibility to reduce the number of readout channels is to widen the pitch size of the readout channel.

Eventually, the design of the enlarged SVD induces many issues to be optimized; the effect of the poorer noise performance, the effect caused by the increased material, the optimization of the readout pitch and the best position of the fifth layer to improve the reconstruction efficiency for  $K_S^0$ 's. Furthermore, the arch structure for the outer layers is also an issue to be studied.

In this subsection, we will discuss the front-end chip and optimization of the configuration<sup>5</sup>. We will then make recommendations on the baseline SVD design.

### A. Inner radius and resolution

The radius of the beam pipe strongly affects the performance of SVD. In particular, the impact parameter resolutions are determined by the radius and the material budget of the beam pipe, the position and the material of the innermost layer and the position of the second layer.

On the other hand, the closer the sensor is to the interaction region, the higher the expected occupancy. Since the beam background level in sBelle is expected to be 15 times higher than in the current Belle configuration, the occupancy at the innermost layer will be a crucial problem. Since the number of fake clusters will increase dramatically and even signal clusters would be deformed by beam backgrounds, the trajectories of tracks reconstructed with fake and/or deformed clusters will be shifted from their true trajectories. Consequently, the hit resolution will deteriorate. This resolution is evaluated from the residual distribution between the true hit point in a certain DSSD

---

<sup>5</sup> the effect of the increased material will be discussed in section IX

and the intersection point of the trajectory with the DSSD. Finer segmentation of the readout channels is one solution to reduce occupancy. Further segmentation ( $< 50 \mu\text{m}$ ), however, is technically difficult and would increase the number of the total readout channels. A pixel type sensor, which has a small amount of material and a fast readout speed, has not been developed yet. Another approach is to suppress the overlaid beam background in the signal time-window by reducing the shaping time. In the Belle SVD, the shaping time of the readout chip, VA chip, is about 800 ns. Therefore, assuming a readout chip whose shaping time is 50 ns, we can reduce the occupancy by a factor of 1/16. Here, we compare the performance of the following three SVD design candidates. We propose the second one as a baseline design for the sBelle SVD. The third one is what was proposed in LoI 2004.

1. “Modified”: a 4-layer SVD with a 1.5 cm radius beam pipe as for the Belle SVD. The readout chip for the two inner layers is replaced with one having a shorter shaping time (50 ns) and a pipelined readout. The readout chips for the remaining outer layers are the same as the current one. (i.e., the shaping time is  $\sim 800$  ns.)
2. “Baseline”: a 6-layer SVD with a 1.5 cm radius beam pipe. Two outer layers at the radial positions of 13 and 14 cm are added to the current Belle SVD configuration. All layers are read out by chips having a shorter shaping time (50 ns) and a pipelined readout.
3. “LoI04”: a 6-layer SVD with a 1.0 cm radius beam pipe. Two outer layers at the radial positions of 13 and 14 cm are added to the current Belle SVD configuration. The two inner layers are replaced with pixel sensors. All layers are read out by chips having a shorter shaping time (50 ns) and a pipelined readout.

First, we estimate the occupancy level in each layer for the above SVD candidates. Table IV shows a rough estimation of the occupancy at a luminosity of  $2 \times 10^{35}/\text{cm}^2/\text{s}$ . For simplicity, in this calculation we assume that the occupancy is proportional to the shaping time, the area of each readout channel and  $1/r^2$ , where  $r$  is the radial position of the layer from the interaction point.

If we assume the limit on the occupancy is 15%, the occupancy of the third and fourth layers in option 1 nearly reaches this limit. Because option 1 still employs the VA readout chip for the outer layers, which take at least  $12.8 \mu\text{s}$  to be read out and does not include any pipeline, the dead time fraction could increase up to 15% or more at the 10 kHz trigger rate. For option 2, since we employ a readout chip having a shorter shaping time, the estimated occupancy for each layer is within an acceptable range. In option 3, thanks to the pixel sensor, the occupancy is kept at a low level for the first and second layers. Moreover, these two options can operate at a 10 kHz trigger rate because of the pipelined readout. Therefore, we need to use a readout chip having a shorter shaping time and a pipelined readout for all layers.

TABLE IV: Estimated occupancy at each layer for the different SVD candidates. The units are in %.

	1	2	3	4	5	6
Op.1. Modified	10	3	15	15	-	-
Op.2. Baseline	10	3	1	1	<1	<1
Op.3. LoI04	<1	<1	3	3	<1	<1

We estimated the impact parameter resolution with the TRACKERR program[10]. The effect of the high occupancy is well-understood from our experience with the Belle SVD. For example, with

30% occupancy, the intrinsic resolution degrades by 50% and the hit association is significantly degraded.

Figure 14 shows the impact parameter resolution as a function of the sine of the detector polar angle. Since the detector configuration for the modified option is the same as that of the current Belle SVD except for the readout chip, the impact parameter resolutions for the modified option (solid lines in Fig. 14) are not different from those of the current Belle SVD. The baseline design (dashed lines in Fig. 14) shows performance comparable to the current Belle SVD for both the  $r\phi$  and  $z$  directions. Because of the shorter lever arm for multiple scattering with the 1.0 cm radius beam pipe, option 3 (dotted lines in Fig. 14) has better impact parameter resolution.

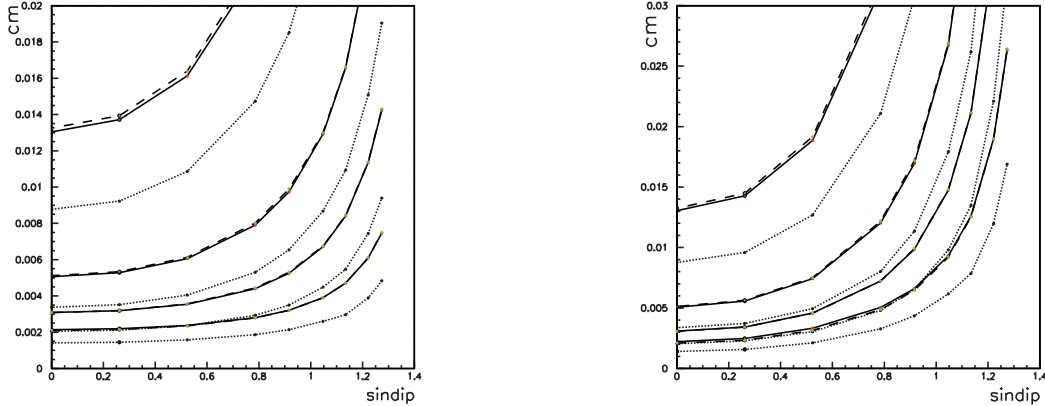


FIG. 14: The impact parameter resolution calculated by TRACKERR for the different SVD configurations. Solid, dashed and dotted lines correspond to option 1 “Modified”, option 2, “Baseline design” and option 3 “LoI04”, respectively. Thanks to the smaller radius beam pipe, option 3 shows better resolution.

## B. Beam background effect on the readout chip

In the previous subsection IV A, the requirements for the readout chip and impact parameter resolutions were obtained. Actually, option 1 is a very unlikely scenario at this stage. However, it is useful to check the effects induced by the beam background on the readout chip, especially on the innermost and second layers, partially because we can use the current Belle GEANT3-based full detector simulation with small modifications and partially because we can also make use of real beam background data for this check.

To simulate option 1, we replace the VA chip of the innermost and second layers of the current SVD by another chip whose shaping time is 50 ns. In this simulation, we assume this chip to be “APV25”. On the other hand, the same VA chip is used for the remaining outer layers. The detector dead time caused by the long readout time of the VA chip is not taken into account throughout this simulation. We estimate the effect of the beam background on analyses by embedding real beam background events taken with a random trigger in the simulated  $B$  meson decay events. In order to differentiate the effect of beam background on the readout chip from other effects, for instance, the effect of the poorly reconstructed tracks that are smeared with beam background hits in the CDC, we embed beam background events in the SVD only. Other details of the simulation procedure are described in [11].

Here we explain the values used to estimate the performance of the SVD. In the  $B$  factories, a  $CP$  violating asymmetry in the time-dependent rates for  $B^0$  and  $\bar{B}^0$  decays to a common  $CP$

eigenstate can be observed through the measurement of the distance between the two  $B$  decay vertices. Therefore the precise measurement of the decay vertices is the key point. For simplicity, the vertex of the  $B$  decaying to a  $CP$  eigenstate is described as the “ $CP$ ” side vertex and that of the accompanying  $B$  is the “tagging” side vertex.

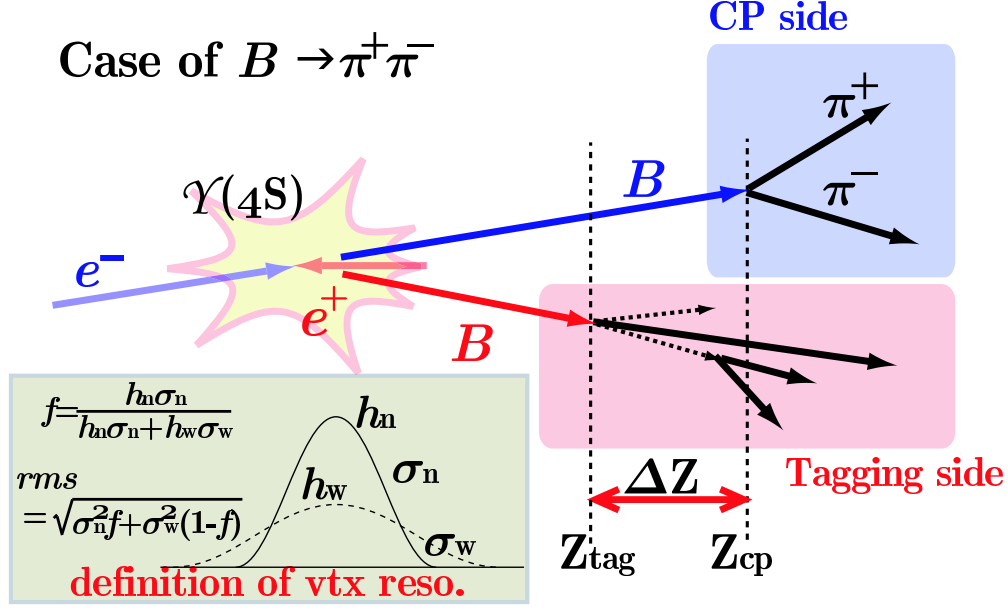


FIG. 15: Illustration of a typical event vertex topology

A typical event vertex topology is depicted in Fig. 15, and the reconstruction procedure is explained as follows. The neutral  $B$  meson is fully reconstructed in the specific  $CP$  eigenstate and then the  $CP$  side vertex is determined by the standard Belle kinematic vertex fitter. The tagging side vertex is reconstructed from the tracks that are not used in the reconstruction of the  $CP$  side. Here the types of the particles used in the  $CP$  side vertex reconstruction are identified from generator information. The distribution of the difference along the beam axis between the reconstructed  $B$  decay vertex position and the true decay point is fitted with a double gaussian form. The vertex resolution for the  $CP$  and tagging side vertices is defined as the area-weighted root mean square (for the definition, see Fig. 15) of the extracted  $\sigma$  values of the narrow and wide components. In the same way, the difference between the distance obtained from the two reconstructed  $B$  decay vertices and the true distance provides so-called the  $\Delta z$  vertex resolution.

Figures 16 (a) and (b) show distributions of  $\Delta z$  resolution for the  $B \rightarrow J/\Psi K_s$  events with the nominal beam background under the assumption of the current SVD and that of option 1, respectively. Figure 17 shows similar distributions with a beam background level five times larger. By comparing these figures, we found that for the current SVD the resolution deteriorates by a factor of 1.4 times when the beam background level is five times larger, whereas for option 1 the resolution is about the same as for the current SVD with the nominal beam background.

Figure 18 shows the  $\Delta z$  vertex resolution as a function of the beam background level. As shown in Fig. 5, we expect roughly a beam background six times larger than the current level in the SVD for the early stages of sBelle. By changing the readout chips of the innermost and second layers from the VA chip to the APV25, we can maintain the  $\Delta z$  vertex resolution at the level that has been achieved by the current SVD with six times higher beam background. In other words, the key to maintaining the current level of the vertex resolution under worse beam background

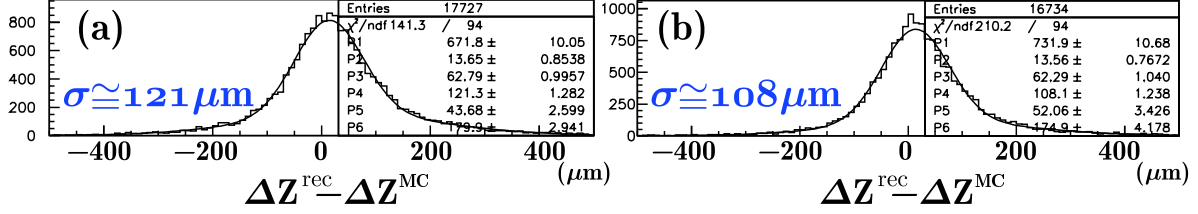


FIG. 16: (a) Distribution of  $\Delta z$  resolution for the SVD with VA readout and the nominal beam background level. (b) similar distribution for option 1.

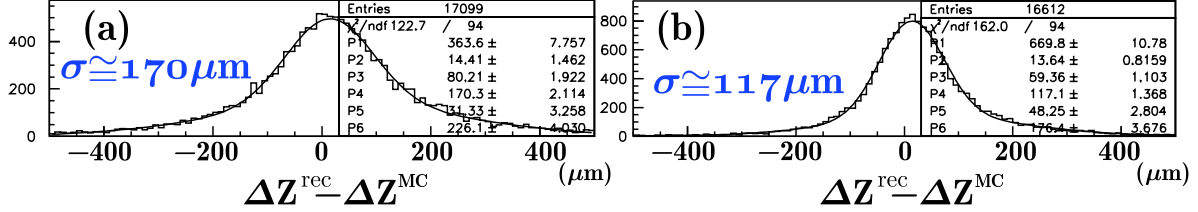


FIG. 17: (a) Distribution of  $\Delta z$  resolution of the SVD with VA with a beam background level five times larger. (b) similar distribution for option 1.

conditions is to suppress the beam background contribution by reducing the shaping time of the readout chip, especially for the innermost and second layers. Here we should recall that we have ignored the dead time induced by the long readout time of the VA chip in this study. As discussed in the previous subsection IV A, the VA chip can not be used with a 10 kHz trigger rate. From these points of view, the APV25, which has a short shaping time (50 ns) and a pipelined readout and which is also a commercially available chip at this stage, is one possible solution.

### C. Outer radius and $K_S^0$ vertex reconstruction efficiency

As discussed in Section III A, to improve the reconstruction efficiency for the decay  $B \rightarrow K^{*0} \gamma$ , we have decided to extend the SVD volume in the radial direction and to enlarge the current 4-layer configuration to a 6-layer one. Although there are no strict limits on the positions of the additional layers, a realistic outer radius of the SVD is currently assumed to be 16 cm. Practical considerations about the support structure suggest that the outermost (= sixth) layer should be located 14 cm from the interaction point.

In reconstructing this decay mode, only two charged pions from the  $K_S^0$  decay can be used for the  $B$  decay vertex determination. Since for each track at least two SVD hits are required, the location of the fifth layer is important. Figure 19 shows the fraction of  $K_S^0$  mesons that decay within a radius  $r$  for this decay mode. The second outermost layer of the current SVD (i.e., third layer) is placed at roughly 7 cm. In this case only  $\sim 60\%$  of the  $K_S^0$  decays from  $B \rightarrow K^{*0} \gamma$  can be detected. In the new SVD, we can increase the number of reconstructed  $K_S^0$ 's considerably by changing the position of the second outermost layer (= fifth layer). For instance, if the fifth layer is placed at  $r = 10$  cm, 75% of  $K_S^0$ 's can be detected in this decay mode.

However, even if the number of reconstructed  $K_S^0$  were be increased, they would be useless without a sufficiently precise measurement of the  $K_S^0$  decay vertex; in addition, a good resolution in the corresponding  $B$  decay vertex position, important to measure the  $CP$  asymmetry, would be

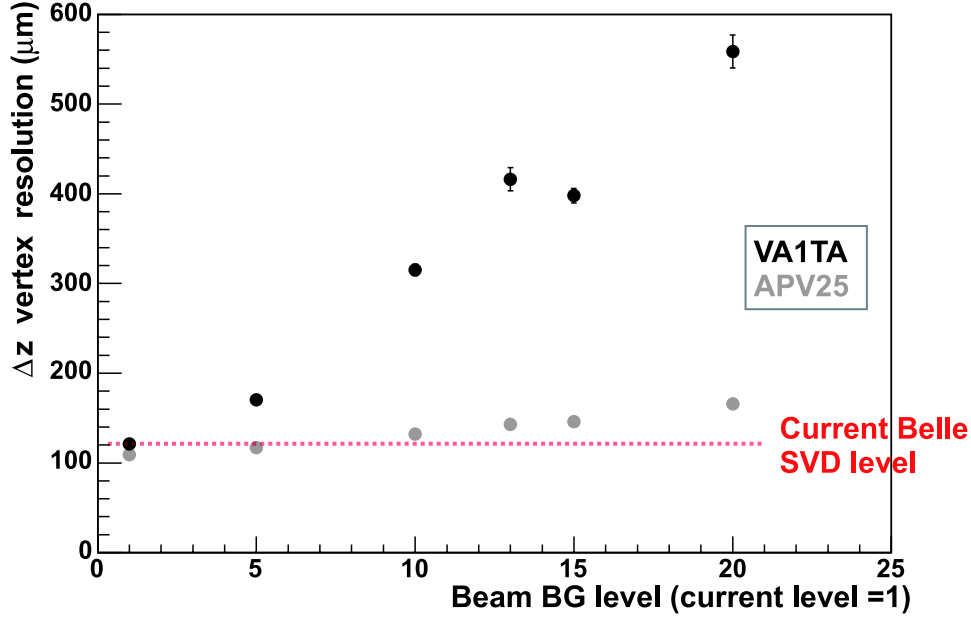


FIG. 18:  $\Delta z$  vertex resolution as a function of the beam background level relative to the current Belle background level: APV25 (black) and VA1TA (gray)

degraded. In this section, we present the results of a simulation study to optimize the location of the fifth layer in terms of both the reconstruction efficiency and the vertex resolution.

For this simulation study we make use of the GEANT3-based full detector simulator that is modified for the 6-layer configuration as described in Section IX A 3. The position of the fifth layer is varied from  $r = 10$  cm to 14 cm while the outermost layer is fixed at  $r = 14$  cm. The standard Belle software is used for tracking,  $K_S^0$  vertexing,  $\pi^0$  reconstruction and  $B$  decay vertex determination. If there are several  $B$  candidates in an event, the best  $B$  candidate is selected by requiring the minimum mass difference between the reconstructed  $B$  masses and the nominal value. The vertex resolution is estimated in the same way as described in section IX A 2.

The detection efficiency for  $B \rightarrow K^{*0}\gamma$  decays is shown in Fig. 20(a) as a function of the location of the fifth layer. By increasing the radius of the fifth layer, the efficiency increases by 29% for  $r = 12$  cm relative to the current 4-layer SVD, and by  $\sim 36\%$  for  $r = 14$  cm. On the other hand, the  $B$  decay vertex resolution deteriorates for larger radii of the fifth layer. It degrades by  $\sim 17\%$  relative to the 4-layer SVD at  $r = 12$  cm and 38% at  $r = 14$  cm (See Fig. 20(b)). For the tagging side vertex resolution, which is not affected by long-lived particles such as  $K_S^0$ 's, the vertex resolution does not depend on the location of the fifth layer (Fig. 20(c)). As expected, the  $\Delta z$  vertex resolution shows a tendency similar to the  $B$  decay vertex resolution (Fig. 20(d)). Up to  $r = 11.5$  cm, the resolution is constant, and then deteriorates as the radius increases.

To search for the optimal position, we need to consider the improvement of the efficiency and the degradation of the resolution simultaneously. Ref [26] shows the correlation between the vertex resolution and the necessary statistics to extract one of the  $CP$  asymmetry parameters  $\mathcal{S}$ . The minimum number of events ( $N_s$ ) required to measure  $\mathcal{S}$  with a statistical significance  $s$  can be



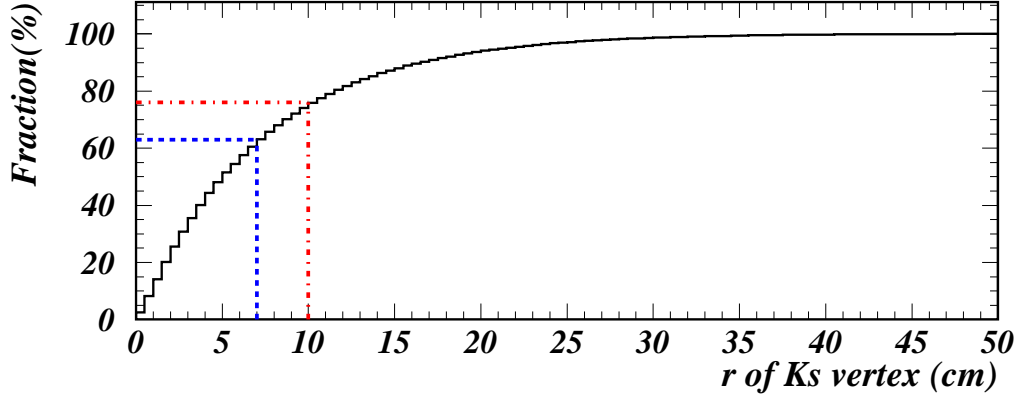


FIG. 19: The fraction of  $K_S^0$ 's that decay within radius  $r$  for the  $B \rightarrow K^{*0}\gamma$  mode. The dashed lines show the location of the second outermost layer of the current SVD ( $r \simeq 7$  cm) and the corresponding fraction, and the dot-dashed lines the case in which the second outermost layer in the upgraded SVD is placed at  $r = 10$  cm.

expressed as

$$N_s \simeq \left( \frac{s}{d \cdot \mathcal{S}} \right)^2 \quad (1)$$

where  $d$  is the so called dilution factor;  $d$  is a function of  $\mathcal{S}$ , the  $B^0 - \bar{B}^0$  mixing parameter  $\delta m/\Gamma$  and the detector response function. For simplicity, a double Gaussian function which is evaluated from the  $\Delta z$  distribution is assumed as the detector response function. In this study, the wrong tag probability and beam background effects are not taken into consideration.

Assuming the value of  $\mathcal{S}$  as expected in the Standard Model,  $\mathcal{S} = 0.03$ , the necessary number of events for the 6-layer SVD  $N_s$  normalized to the corresponding number for the 4-layer case is shown in Fig. 21 as a function of the position of the fifth layer. Apparently, we need more statistics to observe  $\mathcal{S}$  with the same statistical significance with the 6-layer SVD, because the average vertex resolution is degraded due to  $K_S^0$  mesons that decayed between the third and the fifth layers. However, in this figure of merit the effect of the better detection efficiency in a larger SVD volume is not taken into account. Once this efficiency  $\epsilon$  is considered by taking the ratio  $N_s/\epsilon$ , the optimal position of the fifth layer can be determined. The right side of Fig. 21 shows the ratio of  $N_s/\epsilon$  for the 6-layer and 4-layer SVDs. The minimum at about 12 cm indicates the best position for the fifth layer.

So far, the outermost layer has been fixed at  $r = 14$  cm, and the estimated best position of the fifth layer was found to be around  $r = 12$  cm. To generalize this result, similar simulation studies were performed with the outermost layer at  $r = 13$  cm and  $r = 15$  cm. As in the previous study, the position of the fifth layer is varied from 10 cm to the allowed maximum radius in steps of 0.5 cm. The left side of Fig. 22 shows  $N'_s$  for the three cases. We note that the track parameter resolution for tracks that are associated with SVD hits only in the fifth and sixth layers depends on the distance between these two layers. As this distance decreases, the  $B$  vertex resolution degrades, and a larger number of events is required to observe  $\mathcal{S}$  with the same statistical significance. The  $N_s/\epsilon$  ratio for the 6-layer SVD normalized by that for the 4-layer one is shown on the right side of Fig. 22. Again, the minimum indicates the best position of the fifth layer. From these plots, we

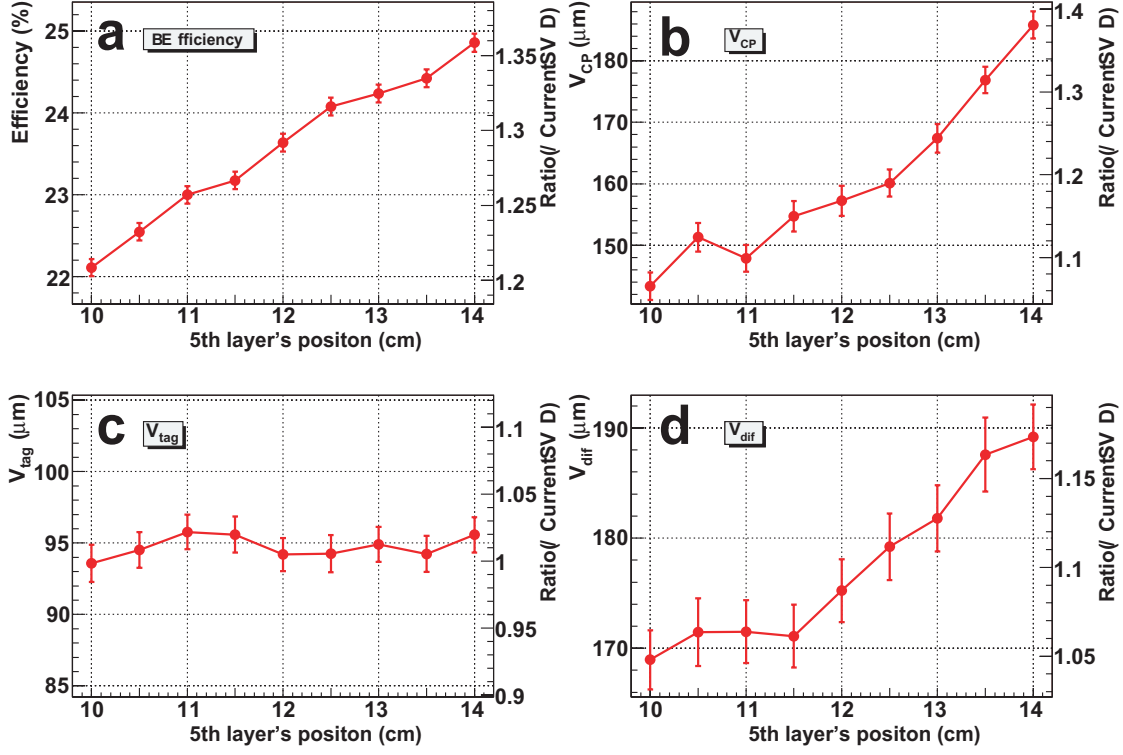


FIG. 20: (a) : The reconstruction efficiency for  $B \rightarrow K^{*0}\gamma$ . (b) and (c) are the  $CP$  side and tagging side vertex resolutions, respectively. (d) shows the  $\Delta z$  vertex resolution. Here all results are shown as a function of the position of the fifth layer in steps of 0.5 cm.

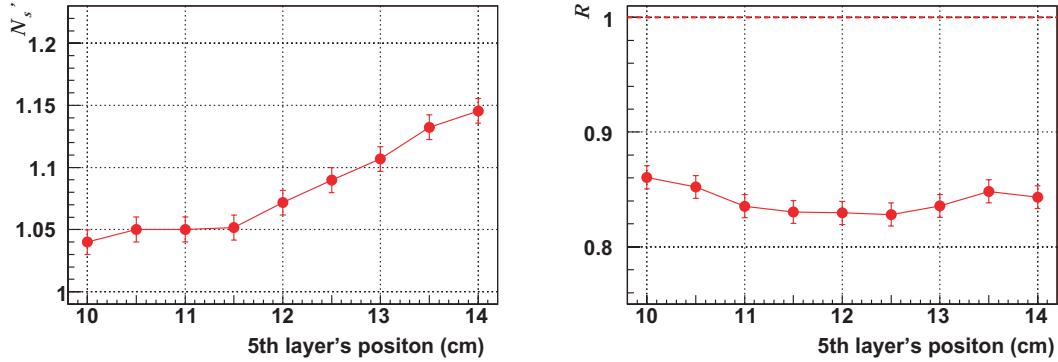


FIG. 21: The necessary number of events for the 6-layer SVD  $N_s$  normalized to the corresponding number for the 4-layer case, as a function of the location of the fifth layer (left). The ratio of  $N_s/\epsilon$  for the 6-layer and 4-layer SVD configurations (right).

conclude that about 2 cm inside the outermost layer seems to be the optimum for all cases.

The above optimization was performed for a specific decay channel  $B \rightarrow K^{*0}\gamma$ . It is mandatory to check whether the position of the fifth layer affects the vertexing performance of other important  $B$  decay modes. The detection efficiency and the vertex resolution for the  $B \rightarrow \pi^+\pi^-$  and  $B \rightarrow \phi K_S^0$  modes were investigated. The outermost layer is fixed at  $r = 14$  cm in this case. For  $B \rightarrow \pi^+\pi^-$ , all tracks used in the vertex reconstruction are produced in the vicinity of the interaction



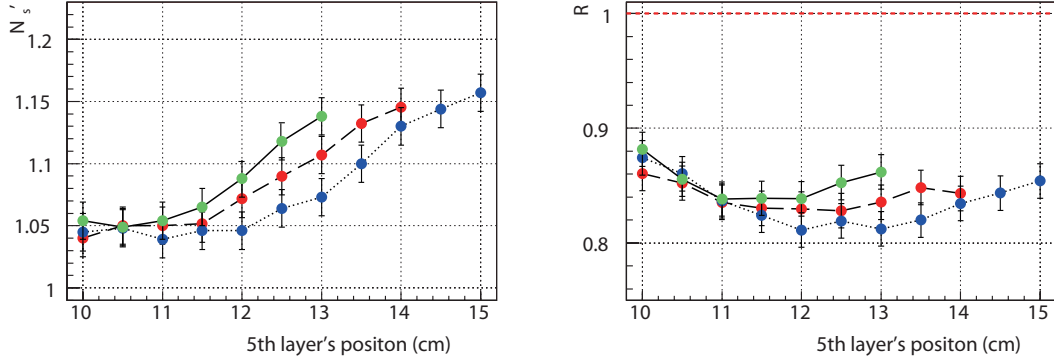


FIG. 22: The necessary number of events for the 6-layer SVD  $N_s$  normalized to the corresponding number for the 4-layer case, as a function of the location of the fifth layer (left). The ratio of  $N_s/\epsilon$  for the 6-layer and 4-layer SVD configurations (right). The solid, dashed and dotted lines correspond to cases with the outermost layer at  $r = 13$  cm, 14 cm and 15 cm, respectively.

point. Therefore, it is expected that the position of the fifth layer does not affect the efficiency nor the vertex resolution. Figure 23 shows the results of this study, and, as expected, we find no variation with the position of the fifth layer. In the case of the  $B \rightarrow \phi K_S^0$ , although a  $K_S^0$  is involved in this decay mode, the decay point of  $B$  is mainly determined by the decay point of  $\phi$ . Hence, it is again expected that the position of the fifth layer does not affect the performance; this is confirmed by Fig. 24.

We conclude that the second outermost layer be located 2 cm inside the outermost layer.

#### D. S/N ratio and track matching efficiency

In order to provide SVD hit information for tracks reconstructed in CDC, the tracking acceptance of SVD should be the same or larger than that of CDC. Therefore, the SVD layers have to cover a wider range of angles with respect to the beam axis. For the Belle SVD, the double sided sensors (DSSDs) are assembled into a “ladder structure”. In particular for the outer layers, several DSSDs are connected and read out by a single front-end chip, which is placed outside the tracking acceptance to reduce the material within the spectrometer acceptance. Since the number of DSSDs increases with the length of the ladder structure, the detector capacitance connected to a single front-end chip increases, and the noise level becomes large.

Furthermore, to reduce the occupancy in the upgraded SVD, we plan to employ a new front-end chip type APV25, which has been developed for the CMS Si tracker, with a shorter shaping time ( $\sim 50$  ns) than the presently used, VA1TA chip. Generally, the shorter shaping time results in a higher intrinsic electronic noise. In the current Belle SVD, the S/N ratio is around 35 for the inner layers and around 16 for the outer layers; the APV25 chip has a noise level four times higher than the VA1TA chip. Because a degraded S/N ratio affects the total performance of the SVD, it is important to evaluate the effect of the poor S/N ratio at the outer layers. In the case of a degraded S/N ratio, we expect that the matching efficiency and the tracking resolution will deteriorate. Here, the matching efficiency is defined as the probability that tracks reconstructed in CDC have hit information in at least two SVD layers. When the noise level becomes very large, the required threshold level could exceed the signal level. In that case, hit signals could be missed,

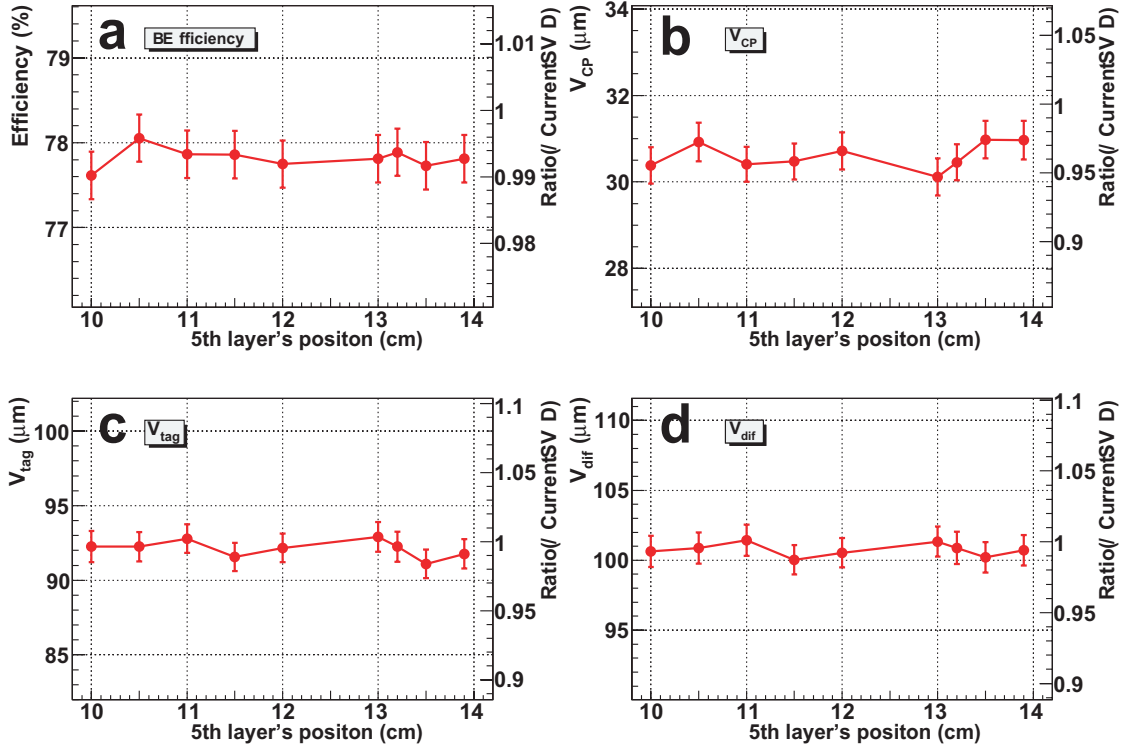


FIG. 23: (a) : The reconstruction efficiency for  $B \rightarrow \pi^+\pi^-$  decay. (b) and (c) are the  $CP$  side and tagging side vertex resolutions, respectively. (d) shows the  $\Delta z$  vertex resolution. Here all results are shown as a function of the position of the fifth layer in steps of 0.5 cm.

and the matching efficiency reduced. Even if we can find the correct signal hit, the high noise level distorts the SVD hit position information and degrades the track resolution.

To evaluate these effects, we carried out simulation studies. For this purpose, the current SVD configuration that is implemented in the standard Belle full detector simulator is replaced with the 6-layer one as shown in Fig. 56. As the detailed configuration for the SVD upgrade has not been determined yet, for the additional two layers we assume the same ladder modules as used in the fourth layer of the present Belle SVD, and place them at  $r = 13$  cm and  $r = 14$  cm.

We have checked the matching efficiency with various noise levels in layers 5 and 6. At first, we simulated generic  $B$  meson decays. In Fig. 25, the matching efficiency is shown normalized to the current Belle SVD performance as a function of the noise level. We increase the noise level on all layers in the figure on the left, and only on layers 5 and 6 for the figure on the right. For the latter case we conclude that the matching efficiency is higher than 99% for any noise level in layers 5 and 6 because there are still four other layers where matched hits can be found.

The main motivation for the proposed 6 layer configuration is to improve the efficiency for the  $K_S^0$  reconstruction. Due to the finite lifetime of  $K_S^0$ , the  $K_S^0$  daughter tracks originate from a vertex far from the IP. In this case, the effect of the poor S/N performance in the outer layers becomes severe. Figure 26 shows the vertex position of the  $K_S^0$  in  $B^+ \rightarrow K_S \pi^+$  decays for the case where two layers of SVD hits could be associated with both daughter tracks. Thanks to the additional two layers, we reconstruct an additional 20% of  $K_S^0$  vertices. Figure 27 shows the matching efficiency with various noise levels. We conclude that about 60% of tracks, decaying between layers 4 and 5, will be lost when the noise levels in layers 5 and 6 are three times higher than in the current Belle

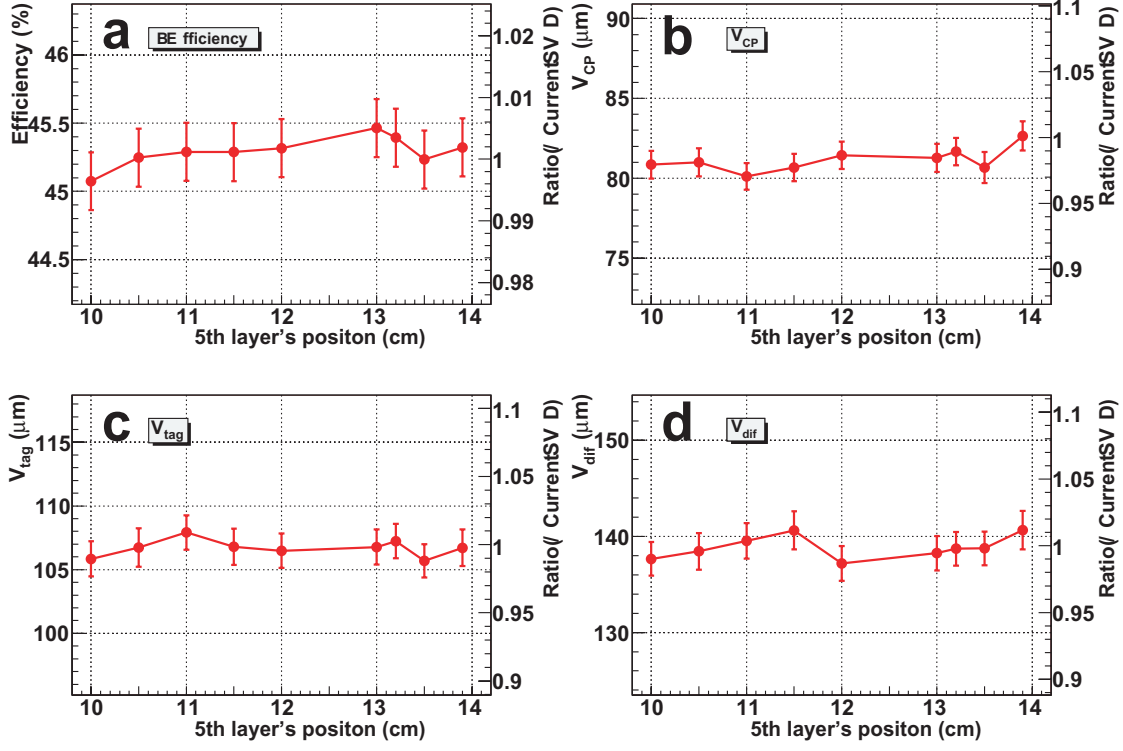


FIG. 24: (a) : The reconstruction efficiency for  $B \rightarrow \phi K_S^0$  as a function of the position of the fifth layer; (b) and (c) are the  $CP$  side and tagging side vertex resolutions, respectively, and (d) shows the  $\Delta z$  vertex resolution.

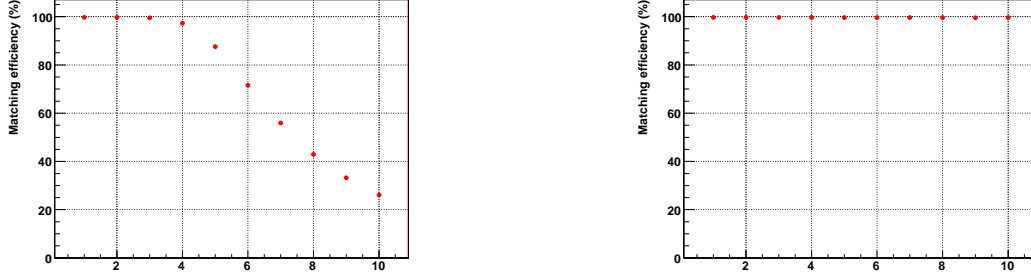


FIG. 25: The matching efficiency as a function of the noise level normalized to the noise level of the layer 4 in the current Belle SVD. The noise level is varied on all layers for the left figure, and on only layers 5 and 6 for the right figure.

SVD.

In the studies discussed above, we search for SVD hits in the DSSDs by applying a threshold cut on the energy deposited per strip at  $3\sigma$ , where  $\sigma$  is the noise level. We tried to recover the matching efficiency by lowering this threshold. Figure 28 shows the matching efficiency obtained with a threshold of  $2\sigma$ . The losses in matching efficiency can be reduced by up to 40% by lowering the threshold. Note, however, that data have to be sparsified when recorded in order to reduce the stored data size. With a lower threshold, we need to store 20 – 30 times more data, which is not trivial from the DAQ point of view.

We conclude that we have to be careful not to increase the noise level when we design the sensor and the readout scheme for the outer layers. It must not exceed a level which is 3 times larger than the one in layer 4 of the present Belle SVD. A possible solution is to develop a low noise DSSD and/or front-end chips. We have started a project to develop our own front-end chip, which has better S/N performance and a fast readout capability. Another solution is to avoid ganging of DSSDs. This can be realized by using a “chip-on-sensor” or a FLEX readout. However, both options will increase the amount of material and the number of readout channels, and will be challenges in the technical design of the SVD upgrade.

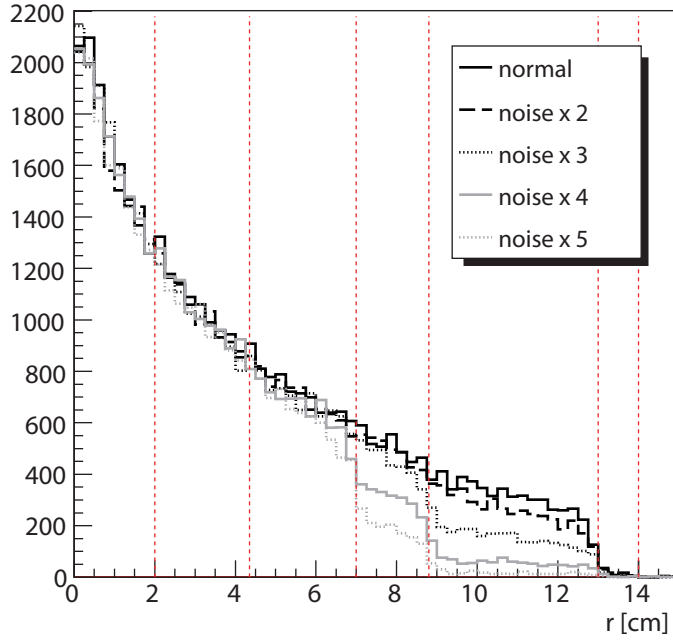


FIG. 26: The distribution of the  $K_S^0$  vertex, whose daughter tracks are matched with two layers of SVD hits, in  $B^+ \rightarrow K_S \pi^+$  for different noise levels in layers 5 and 6. The positions of individual layers are indicated by dashed lines. Thanks to layers 5 and 6, 20% more  $K_S^0$ 's are reconstructed within the SVD. The benefit is, however, diluted at higher noise levels.

### E. Readout pitch of outer layers

Due to the enlarged SVD volume in the radial direction, we can increase the reconstruction efficiency for  $K_S^0$  events. A much larger SVD volume requires an increase in the number of readout channels as described in section IV. It is therefore important to study whether or not the number of readout channels can be reduced without degrading the performance, especially for the outer layers. For this purpose, we use the GEANT3-based simulation again that was modified for the study in subsection IV C. This time, the strip pitch of the outermost (=sixth) and fifth layers is artificially increased. Note that this modification is applied only to the z-side strips, i.e., strips along the  $z$  direction, since it is expected that a corresponding change in the other direction could degrade the  $B$  vertex resolution. We compare the performance of the detector with the initial z-side

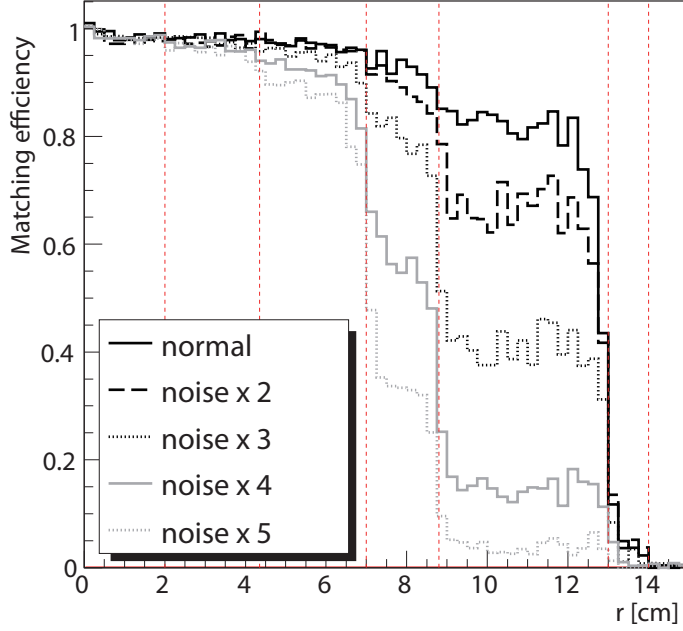


FIG. 27: The matching efficiency as a function of the  $K_S^0$  vertex position in  $B^+ \rightarrow K_S^0 \pi^+$  for different noise levels. If the noise level is 3 times higher than that of the present Belle SVD, the gain from the extra coverage by the outer layers is reduced by 50%.

strip pitch at  $73 \mu\text{m}$ , and with three alternatives,  $110 \mu\text{m}$ ,  $150 \mu\text{m}$  and  $290 \mu\text{m}$ . We only vary the strip pitch for the outer two layers (5 and 6). The positions of the outer two layers are fixed to  $r = 12 \text{ cm}$  and  $14 \text{ cm}$ . Figure 29 shows the distributions of the z-side cluster width in the fifth and sixth layers for tracks that are produced at the coordinate origin with a polar angle of 30 degrees. For tracks with a shallow incidence angle, the wider the strip pitch is, the smaller the cluster width becomes.

In general, a strip-type sensor with a wider pitch has worse spatial resolution than that with a narrow pitch. If we increase the strip pitch for the outer layers, the vertex resolution for the  $K_S^0$ 's that decay between the fourth and fifth layers could degrade. On the other hand, the vertex resolution for the  $K_S^0$ 's that decay in the vicinity of the interaction point should not change much, since the better spatial resolution of the inner layers has a greater impact on the vertex resolution than the poorer resolution of the outer layers. In order to check these expectations, the vertex resolution for the  $B \rightarrow K^{*0} \gamma$  decay is investigated. The analysis procedure is the same as in subsection IV C. The vertex resolutions for the case where the z-side strip pitches are set to  $73 \mu\text{m}$  and  $150 \mu\text{m}$  are shown in Fig. 30. Shown at the top are the resolutions for the case where at least two SVD hits are required to reconstruct each charged pion, which is a decay product of the  $K_S^0$  from the  $K^{*0}$  decay chain. The middle figures in Fig. 30 show the same distributions for the case where at least one of the two charged pions is required to have SVD hits only in the outer two layers. From these plots, a clear degradation caused by the wider strip pitch is observed in the vertex resolution. In contrast, when we require hits in all SVD layers for at least one of the two charged pions, no degradation is observed as shown in similar distributions at the bottom of Fig. 30. The results including cases with other pitch values are summarized in Table V.

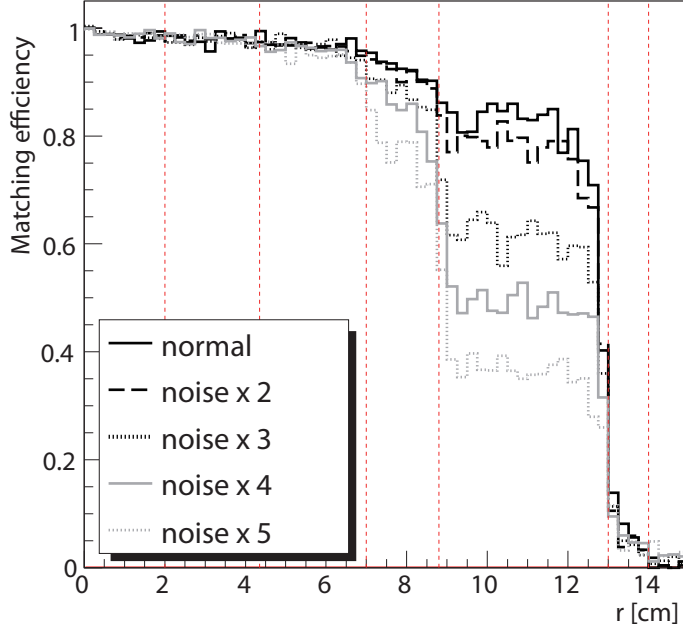


FIG. 28: The matching efficiency as a function of the  $K_S^0$  vertex position in  $B^+ \rightarrow K_S \pi^+$ , where the threshold for SVD hit finding is reduced from  $3\sigma$  to  $2\sigma$ .

Table V shows that there is no sizable degradation in the vertex resolution, if we require SVD hits in all layers for the charged pions used to reconstruct the  $K_S^0$  (see “hits in all lyrs” in Table V). Furthermore, when a charged track has SVD hits in the outermost and fifth layers only, the vertex resolution becomes worse (see “hits in 5th & 6th lyrs only” in Table V). In particular, in the case where the strip pitch is set to  $290 \mu\text{m}$  the vertex resolution degrades by roughly 20% (for the more specific case where at least one charged pion is required to have SVD hits in the outermost and fifth layers only, which is denoted as “at least 1 track” in Table V). In this case, the merit of the enlarged SVD volume, that is, the better reconstruction efficiency for  $K_S^0$ ’s, could be reduced by the poorer resolution. For the case of  $110 \mu\text{m}$  strip pitch, the vertex resolutions are comparable to the case of  $73 \mu\text{m}$  strip pitch, except when both charged pions have SVD hits in the outermost and fifth layers only. With the requirement that a charged track must have at least two SVD hits without any constraint on which layers were hit (the standard procedure in  $K_S^0$  reconstruction in Belle, see “ $\geq 2$  lyr hits” in Table V), we observe a degradation by about 4% even for the case of  $110 \mu\text{m}$  strip pitch compared to the case of  $73 \mu\text{m}$  strip pitch. If only these results are taken into account, strip pitches in the range up to  $110 - 150 \mu\text{m}$  seem to be acceptable. However, as will be discussed in section IX, we also have to consider the effect of the increased material in order to maintain a S/N ratio of  $\sim 15$  even in the outer layers. Because the effect of the increased material cannot be avoided, a further degradation caused by the wider strip pitch is not acceptable.

To conclude this subsection we note that outer layers with a wider strip pitch are not an optimal solution for the  $K_S^0$  reconstruction in the analysis of  $B \rightarrow K^{*0} \gamma$  decays. One possibility is to introduce sensors with a wider strip pitch in the forward and backward region of the outer layers, while keeping the current strip pitch ( $\sim 73 \mu\text{m}$ ) in the main cylindrical part. As reported in [12], the intrinsic resolution of the sensors with a wider strip pitch could be better than that with narrow

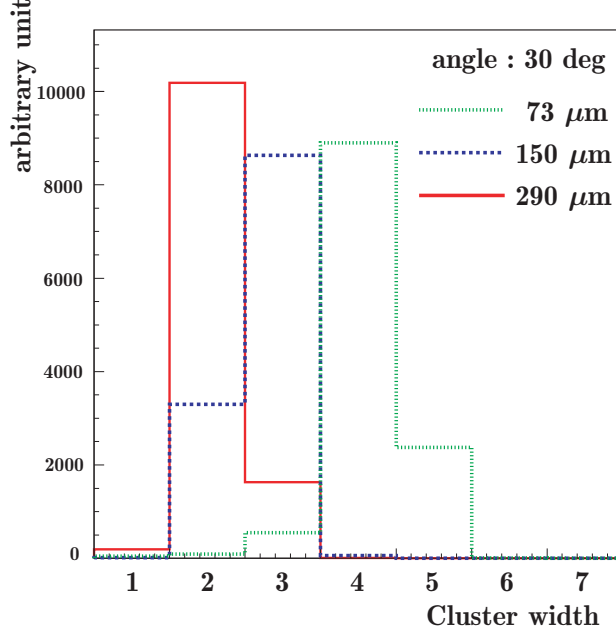


FIG. 29: Distributions of the z-side cluster width in the fifth and sixth layers for tracks that are produced at the IP with a polar angle of 30 degrees. The transverse momentum of tracks is fixed to 2.0 GeV/c. The dotted line, dashed line and solid line corresponds to the case where the z-side strip pitch is set to 73  $\mu\text{m}$ , 150  $\mu\text{m}$  and 290  $\mu\text{m}$ , respectively. In this simulation, the collected charges on the floating strip are divided equally and added to the adjacent strips, while those of the readout strip are left untouched.

strip pitch for particles with a shallow incidence angle (larger than 50 degrees). Thanks to this, the vertex resolution in the vicinity of the interaction point should not be affected. However, even this modification would degrade the performance of  $K_S^0$ 's that decay between the fourth and fifth layers.

As an alternative solution, the introduction of an arc-shaped detector or a slanted detector would reduce the number of readout channels in the outer layers. Note, however, that in this case the SVD detector would occupy a smaller overall volume; as a consequence, the  $K_S^0$  reconstruction efficiency would be reduced.

TABLE V: Decay vertex resolution for  $B \rightarrow K^{*0}\gamma$  decays. Charged pions from the  $K_S^0$  decay are required to have at least two SVD hits (denoted as “default”) or more (denoted as “hits in all lyrs” and “hits in 5th + 6th lyrs only”).

(z-side strip pitch)	$\geq 2$ lyr hits.	hits in all lyrs		hits in 5th & 6th lyrs only	
	(default)	(at least 1 track)	(for both tracks)	(at least 1 track)	(for both tracks)
73 $\mu\text{m}$	$162 \pm 1$ ( $\mu\text{m}$ )	$94 \pm 2$ ( $\mu\text{m}$ )	$66 \pm 1$ ( $\mu\text{m}$ )	$288 \pm 5$ ( $\mu\text{m}$ )	$234 \pm 4$ ( $\mu\text{m}$ )
110 $\mu\text{m}$	$168 \pm 1$ ( $\mu\text{m}$ )	$91 \pm 1$ ( $\mu\text{m}$ )	$61 \pm 1$ ( $\mu\text{m}$ )	$283 \pm 5$ ( $\mu\text{m}$ )	$300 \pm 5$ ( $\mu\text{m}$ )
150 $\mu\text{m}$	$170 \pm 2$ ( $\mu\text{m}$ )	$93 \pm 2$ ( $\mu\text{m}$ )	$62 \pm 1$ ( $\mu\text{m}$ )	$317 \pm 5$ ( $\mu\text{m}$ )	$304 \pm 4$ ( $\mu\text{m}$ )
290 $\mu\text{m}$	$176 \pm 1$ ( $\mu\text{m}$ )	$97 \pm 2$ ( $\mu\text{m}$ )	$63 \pm 2$ ( $\mu\text{m}$ )	$342 \pm 4$ ( $\mu\text{m}$ )	$352 \pm 5$ ( $\mu\text{m}$ )



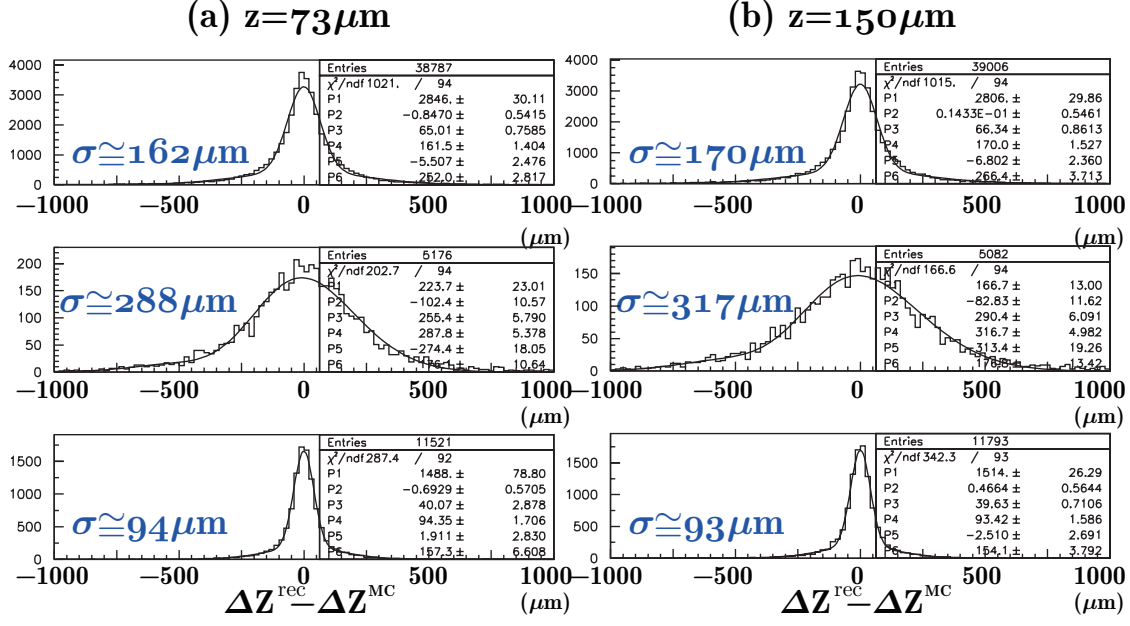


FIG. 30: Decay vertex resolution for  $B \rightarrow K^{*0}\gamma$  decays with z-side strip pitches of  $73\,\mu\text{m}$  (column a) and  $150\,\mu\text{m}$  (column b). For the top of each (a) and (b), we require at least two SVD hits to reconstruct each charged pion. The middle figures show the distributions for the case where at least one of the two charged pions is required to have an SVD hit in the outermost two layers. The bottom figures are the distributions for the case where hits are required in all SVD layers for at least one of the two charged pions.

## F. Slant angle

In the silicon vertex detector (SVD) of the Belle experiment, all the DSSD sensors are placed parallel to the beam axis. The 2004 Super KEKB LoI introduced slanted sensors to the SVD configuration in the forward region. These slanted sensors reduce the length of the SVD ladders in the outer layers. Note that even in present SVD2 with four layers, the length of the layer 4 ladders is about 50 cm.

In the design, we tried to minimize the number of DSSD types in order to reduce the cost of masks used in the silicon process. However, the ladders in the outer layers are still long, and a reduction of ladder length might be beneficial. In addition, it was pointed out that the dip angles of particles entering the DSSDs become very shallow in the forward region. The effective material thickness and cluster size increase by a factor of 3 – 4 compared to those in the central region, and vertex reconstruction and position resolution degrade.

To address this problem, an optimization of the sensor configuration is carried out. Slanted sensors are introduced both in the forward and backward regions, and the slant angles are varied to find the best solution.

The optimization is based on the minimization of the average incident angle of tracks originating in the collision point. Parameters used in this optimization are shown in Figure 31. The angles  $\theta_1$  and  $\theta_2$  are polar border angles of the planar sensor section,  $\phi_0$ ,  $\phi_1$  and  $\phi_2$  are the slant angles;  $\theta_1$ ,  $\theta_2$ ,  $\phi_0$ , and  $\phi_2$  are the free parameters, and  $\phi_1 = 0$  is fixed as the middle sensor is kept parallel to the beam axis.



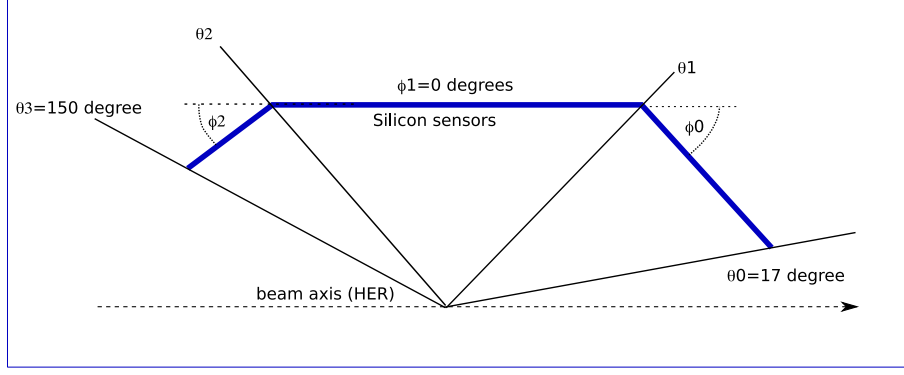


FIG. 31: The schematic of a SVD ladder, with slanted sensors in the forward and backward regions with the definition of angles used for the optimization.

TABLE VI: Table for the optimization

	$\theta_0$	$\theta_1$	$\theta_2$	$\theta_3$	$\phi_0$	$\phi_1$	$\phi_2$	$V_1$	$V_2$	$S$ (cm <sup>2</sup> )
No Slant	17	-	-	150	-	0	-	29	34	6161
LoI	17	34	-	150	-15	0	-	28	33	5018
Disk	17	45	135	150	-90	0	90	24	28	3431
Optimized	17	70	108	150	-41	0	36	11	13	2419

The optimization is carried out by minimizing either the average incident angle or its square,

$$V_1 = \overline{\text{Incident angle}} = \int (\text{Incident angle}) \cdot d \cos \theta \quad (2)$$

$$V_2 = \overline{\text{Incident angle}^2} = \int (\text{Incident angle})^2 \cdot d \cos \theta \quad (3)$$

for tracks within the acceptance ( $17^\circ < \theta < 150^\circ$ ).

In addition to the LoI design (slanted sensors only in the forward region) and the optimized design, these variables are also calculated for a cylindrical detector with no slanted sensors, as well as for a configuration with disks in the forward and backward regions ( $\phi_2 = -\phi_0 = 90^\circ$ ). The total DSSD area  $S$  for layer 6 ( $R=14$  cm) is calculated to estimate the cost of the detector.

The optimization using  $V_1$  and  $V_2$  gives almost the same answer within  $1^\circ - 2^\circ$ . After the optimization, the average incident angle is close to 1/3 of the LoI design value, and the sensor area  $S$  is reduced by a factor of more than two. The values of  $V_1$  and  $V_2$  for the non-slanted design and LoI design are almost the same. This is due to the fact that in the LoI design the slanted region covers only a very small solid angle. Note also that in the LoI design we only save 20% of the sensor area compared to the cylindrical non-slanted solution.

## G. Summary of recommendations for SVD

### Front-end chip

In terms of the impact parameter resolution, the innermost layer should be located as close to the beam pipe as possible. This means that the innermost layer should be operable under a harsh beam background that is estimated to be 15 times higher than in the current Belle detector. According to subsection IV A, this problem can be solved by adopting a front-end chip that has a shorter shaping time, such as  $\sim 50$  nsec. Furthermore, from the MC study described in subsection IV B, the vertex resolution for  $B \rightarrow J/\Psi K_S^0$  can be maintained at the same level that has been achieved by the current SVD even if the beam background level is six times higher. Here in this simulation, the front-end chips of the innermost and second layers are assumed to be "APV25's". Therefore, increased occupancy from the beam background can be reduced to a manageable level by adopting a front-end chip that has a shorter shaping time, especially for the innermost and second layers. For the readout speed, the current front-end chip "VA1" takes  $13 \mu\text{sec}$  to be read out with the maximum possible clock rate. This is not acceptable with a high trigger rate, such as 10 kHz. In order to cope, we need a front-end chip that has a pipelined readout scheme even for the outer layers. Therefore, **a front-end chip that has both a shorter shaping time ( $\sim 50$  nsec) and a pipelined readout scheme is required for all layers to overcome the higher beam background without degrading the performance.**

### Geometrical design

To increase the vertexing efficiency for the  $K_S^0$  from the  $B \rightarrow K^{0*} \gamma$  decay chain, the SVD volume is enlarged in the radial direction. Because at least two SVD hits for each daughter pion are required to reconstruct the  $K_S^0$ , the position of the second to outermost layer is important. As demonstrated by the simulation in subsection IV C, **the best position of the second to outermost layer is found to be 2 cm inside the outermost layer.**

Due to the expansion of the SVD volume, the detector, especially in the outermost and fifth layers, becomes longer. This leads to an increase of the detector capacitance and leakage current in the front-end chip. Consequently, the noise level becomes larger. Furthermore, the shorter shaping time also results in higher intrinsic electronic noise. The simulation study performed in subsection IV D shows that the S/N ratio for all the layers should be better than a third of that in the current Belle SVD, which is roughly 35 for the inner layers and about 16 for the outer layers. Otherwise, the efficiency for matching tracks between the SVD and the CDC will degrade. In particular in  $K_S^0$  vertexing, we would lose 60% of tracks that decay between the fourth and fifth layers if the noise level is three times higher than in the current Belle SVD. **A possible solution to overcome the poorer S/N ratio is to develop a system with low-noise sensors (DSSD) and/or front-end chips.** However, this has not been accomplished yet. **Another solution is to make use of a relatively established technology, e.g., "chip-on-sensor", which can avoid the ganging of sensors.** However, to realize this we need to clarify the material budget of the chips and the cooling systems (the choice of the coolant, the flow rate of the coolant circulation, the material of the cooling pipe and must test the temperature/pressure tolerance, the leakage of the coolant, corrosion, clogging and the connection of the cooling pipe to the outside), the number of readout channels, the support structure and the space for the cabling and so on.

The effect of the additional material is studied in subsection IX A. For physics that aims at  $CP$  violation, for instance,  $B \rightarrow J/\Psi K_S^0$ ,  $\pi^+ \pi^-$  and  $D^+ D^-$ , increasing the amount of material in the innermost and second layers degrades the  $\Delta z$  vertex resolution by roughly 10%. Therefore **we recommend that the chip-on-sensor should not be adopted for the innermost and second**

**layers. On the other hand, for the outer layers (the outermost and second to outermost layers), we have to compromise because the degradation from S/N is more serious than that from the increase in material budget.**

Another side effect of the expansion of the SVD volume is an increase of the number of readout channels. Moreover, as described in subsection IV D, the chip-on-sensor technology will be applied to maintain the current level of S/N,  $\sim 15$ , especially for the outer layers. In this case, the number of readout channels would increase drastically. In order to explore the possibility that the number of readout channels in the outer layers can be reduced without degrading the performance, a MC study was carried out with  $B \rightarrow K^{0*}\gamma$  decay, because this mode is sensitive to the performance of the outer layers. In this simulation, the z-side strip pitch, which is nominally  $73\ \mu\text{m}$ , was increased by a factor of two or four and then the  $CP$  side vertex resolution was examined. From the results obtained in subsection IV E we conclude that the wider strip pitch seems to be feasible. However, considering the degradation caused by the increased material to maintain the current level of S/N, **further degradation from a wider strip pitch is no longer acceptable.** As an alternative solution, **the introduction of an arch-shaped detector or a slanted detector is recommended.**

When the arch-shaped detector or the slanted detector configuration is considered, one can optimize by minimizing the average incidence angle of tracks from the interaction point to the sensor. Thus the "optimized" design shown in subsection IV F is determined. Thanks to this optimization, we find a better resolution than the case without an arch-shaped or slanted detector. Furthermore, the total area covered by sensors also can be reduced, which directly reduces the cost. However, if the fifth layer is located at  $r = 12\ \text{cm}$  in the optimized design, roughly 8% of  $K_S^0$ 's would be lost. Consequently, among the four options shown in subsection IV F, the LoI design is the best in terms of  $K_S^0$  vertexing efficiency. However, **there is still much room to optimize the arch-shaped or slanted part to optimize the tracking performance, the track matching efficiency between CDC and SVD, the detection efficiency for the  $K_S^0$  and the effect of the beam background. This should be clarified before the final decision on the SVD design.**

Although we did not discuss the middle layers (the third and fourth layers), these are also important for the SVD stand-alone tracking. At this moment, we have not decided the position of these layers and the choice of technology for the readout system. The decision will depend on several issues such as a possible mechanical structure for these layers, how many readout channels are acceptable, and what level of the S/N can be achieved; these issues have not been studied in detail yet. We will fix these in parallel with the hardware development.

## V. CDC PERFORMANCE

There are three requirements to be able to operate the new CDC with higher beam background. First, the dead time for the readout electronics must be reduced. At present, we are using charge to time conversion chips and multi hit TDCs for measurements of the drift time and the energy loss. The conversion takes some time (800 – 2200 nsec) and the drift time cannot be measured during that time. This contributes to the dead time. The new system records the timing with a pipelined TDC and the charge with an FADC separately. The dead time for the new system depends on the shaping time for the new ASIC chip and will be around 200 nsec. This is significantly better than in the present system. Second, the cell size must be reduced. This means that the number of cells in one layer increases and the maximum drift time decreases. The number of cells for the first super layer (where the most serious background is expected) increases from 64 to 160 (A small cell chamber was installed instead of the cathode chamber in 2003. It has 128 cells for just two layers in order to test the small cell principle and has been working well for 5 years.) Finally, we will increase the number of stereo layers in each super layer to obtain higher efficiency for three dimensional tracking. A detailed wire configuration is described in the LoI [1]. We studied the effects of background on tracking performance including these improvements included in the upgrade; the results are described in the subsections that follow.

### A. Tracking efficiency and mass resolution

We approximately estimate the tracking performance in sBelle using the Geant3-based detector simulator for Belle. The same CDC and SVD as used in Belle are assumed except for the dead time of the readout electronics for the CDC, which is set to 200 nsec. The high beam background environment expected at sBelle is simulated by superimposing real random triggered events (taken with the Belle detector) on each simulated signal event.

We assume three beam background levels in the simulation study:

- nominal ( $1 \times \text{bkg}$ ): 1 times bkg both in the CDC and SVD, where bkg is the nominal level of beam background observed in the Belle detector;
- moderately-high ( $5 \times \text{bkg}$ ): 3 times bkg in the CDC and 1 times bkg in the SVD;
- highest ( $20 \times \text{bkg}$ ): 13 times bkg in the CDC and 1 times bkg in the SVD.

Here note that the background level in the highest (moderately-high) case is 20 (5) times nominal, which approximately corresponds to 13 (3) times bkg in the sBelle CDC, whose cell sizes are smaller than those of the Belle CDC. The beam background in the SVD is assumed to be nominal in all cases, because readout electronics with much shorter ( $\sim 1/16$ ) shaping time than in the Belle SVD will be used for the sBelle SVD.

The track-finder in the CDC used in the study is one that has been recently updated. It has higher tracking efficiency than that used to process data so far in Belle, especially for events with high charged multiplicity. In addition, the stand-alone track-finder for the SVD, which became available recently is used. This finder aims at efficient tracking of low momentum particles such as the slow pion from  $D^* \rightarrow D^0 \pi$  decay.

The physics channels studied are,  $B^0 \rightarrow J/\psi K_S^0$  ( $J/\psi \rightarrow \mu^+ \mu^-$ ;  $K_S^0 \rightarrow \pi^+ \pi^-$ ), which is an example of a typical channel, and  $B^0 \rightarrow D^{*+} D^{*-}$  ( $D^{*\pm} \rightarrow D^0 \pi_s^\pm$ ;  $D^0 \rightarrow K^0 3\pi$ ), which is an example of the most difficult channels in terms of tracking.

1. Result for  $B^0 \rightarrow J/\psi K_S^0$

Summarized in Table VII are the reconstruction efficiencies and relative efficiencies for the three background cases.<sup>6</sup>

TABLE VII: Reconstruction efficiencies and relative efficiencies for  $B^0 \rightarrow J/\psi K_S^0$  for the three background cases. The efficiency in Belle is also shown in the last row for comparison.

bkg level	eff. (%)	eff. ratio - 1 wrt $1 \times \text{bkg}$ (%)	eff. ratio - 1 wrt Belle (%)
$1 \times \text{bkg}$	58.7	$\equiv 0$	+11.3
$5 \times \text{bkg}$	57.7	-1.7	+ 9.4
$20 \times \text{bkg}$	53.6	-8.8	+ 1.5
$1 \times \text{bkg}$ (Belle)	52.7	-	$\equiv 0$

As shown in column 3 of the table, the reconstruction efficiency in the highest (moderately-high) background case drops only by  $\sim 9$  (2)% with respect to the nominal background case. Furthermore as shown in column 4, nearly the same efficiency as in Belle can be maintained even in the highest background case, thanks to the hardware (reduced dead time and smaller cell size) and software improvements. Note that the efficiencies in the table are those derived from the CDC track-finder, with the SVD stand-alone track-finder turned off. The difference in efficiency between the SVD track-finder off and on is very small,  $\sim 0.1 - 0.2\%$  level, because the final state does not include slow particles.

Summarized in Table VIII are the mass and  $\Delta E$  resolutions. The degradations of the resolutions due to background are not large, at the few % level.

TABLE VIII: Mass and  $\Delta E$  resolutions for  $B^0 \rightarrow J/\psi K_S^0$  for the three background cases. Here the resolution is simply defined as  $\sigma$  of a single-Gaussian fit to the distribution in question. The resolutions in Belle are also shown in the last row for comparison.

bkg level	$M(\mu^+\mu^-)$ (MeV/ $c^2$ )	$M(\pi^+\pi^-)$ (MeV/ $c^2$ )	$\Delta E$ (MeV)
$1 \times \text{bkg}$	8.9	2.2	7.2
$5 \times \text{bkg}$	8.9	2.2	7.4
$20 \times \text{bkg}$	9.1	2.3	7.5
$1 \times \text{bkg}$ (Belle)	8.8	2.1	7.1

<sup>6</sup> The event selection is performed with the following criteria:  $-60 < (M(\mu^+\mu^-) - M_{J/\psi}) < 36 \text{ MeV}/c^2$ ,  $|M(\pi^+\pi^-) - M_{K_S^0}| < 16 \text{ MeV}/c^2$ ,  $5.270 < M_{\text{bc}} < 5.290 \text{ GeV}/c^2$  and  $|\Delta E| < 40 \text{ MeV}$ . These are somewhat simpler criteria than those applied in the data analysis in Belle [13].

## 2. Result for $B^0 \rightarrow D^{*+} D^{*-}$

The final state includes ten charged particles, two of which are low momentum pions from  $D^{*}$ 's, hence this is regarded as one of the most difficult channels in term of charged particle tracking.

Summarized in Table IX are the reconstruction efficiencies and relative efficiencies for the three background cases.<sup>7</sup>

TABLE IX: Same as Table VII but for  $B^0 \rightarrow D^{*+} D^{*-}$ .

bkg level	eff. (%)	eff. ratio - 1 wrt $1 \times \text{bkg}$ (%)	eff. ratio - 1 wrt Belle (%)
$1 \times \text{bkg}$	7.3	$\equiv 0$	+119
$5 \times \text{bkg}$	6.7	-9	+99
$20 \times \text{bkg}$	4.4	-41	+30
$1 \times \text{bkg}$ (Belle)	3.3	-	$\equiv 0$

As shown in column 4 of the table, the reconstruction efficiency for the nominal (and 5 times) background case is approximately twice that of Belle, thanks to the hardware and software improvements. The efficiency in the highest background case, however, significantly drops (column 3) in contrast to the  $J/\psi K_S^0$  channel. This is because many (2.5 times more) low momentum charged particle tracks must be reconstructed in this channel compared to  $J/\psi K_S^0$ . Nevertheless, an efficiency higher than in Belle can be maintained (column 4).

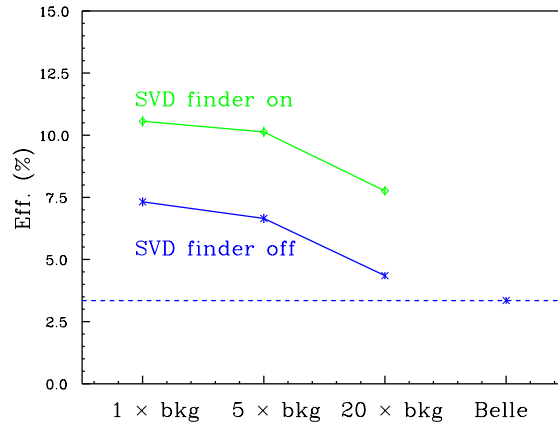


FIG. 32: Reconstruction efficiencies for  $B^0 \rightarrow D^{*+} D^{*-}$  with the SVD stand-alone track-finder on and off.

<sup>7</sup> The event selection is performed with the following criteria:  $|M(K3\pi) - M_{D^0}| < 16 \text{ MeV}/c^2$ ,  $|\delta M - \delta M_{\text{nominal}}| < 3 \text{ MeV}/c^2$  ( $\delta M \equiv M(K3\pi\pi_s) - M(K3\pi)$ ),  $|M_{\text{bc}} - M_{B^0}| < 10.5 \text{ MeV}/c^2$  and  $|\Delta E| < 40 \text{ MeV}$ . These are somewhat simpler criteria than those applied in the Belle data analysis [14].

Shown in Fig. 32 are the reconstruction efficiencies with the SVD stand-alone track-finder on, along with the efficiencies with the SVD finder off (the same efficiencies as in Table IX). As seen in the figure, the SVD finder improves the efficiency significantly, because this finder is very efficient for the low momentum pions from  $D^*$ 's.

Summarized in Table X are the mass and  $\Delta E$  resolutions. No degradation is found (within fitting errors) either in the  $D$  mass or in the  $D^* - D$  mass difference resolution, whereas there is a  $\sim 10\%$  degradation in the  $\Delta E$  resolution.

TABLE X: Same as Table VIII but for  $B^0 \rightarrow D^{*+}D^{*-}$ . These are results obtained without the SVD track-finder.  $\delta M \equiv M(K3\pi\pi_s) - M(K3\pi)$ .

bkg level	$M(K3\pi)$ (MeV/ $c^2$ )	$\delta M$ (MeV/ $c^2$ )	$\Delta E$ (MeV)
$1 \times \text{bkg}$	5.1	0.72	7.2
$5 \times \text{bkg}$	5.0	0.72	7.5
$20 \times \text{bkg}$	5.1	0.70	7.9
$1 \times \text{bkg (Belle)}$	4.9	0.73	7.1

## B. Summary of CDC performance

The CDC will be upgraded to handle much higher beam background. Quick simulation studies including the effects of the upgraded components, such as the smaller cell size, optimized time windows, as well as the new tracking algorithm and the SVD standalone tracker, have been carried out. We found that the new CDC will maintain a track reconstruction performance that is similar to the present CDC.



## VI. PID PERFORMANCE

### A. TOP counter

#### 1. Overview

In a TOP counter, Cherenkov photons are guided to the photon detector by total internal reflections (Fig. 8). The detector measures the precise arrival time and position of the photons. The determination of the velocity,  $\beta$ , of the particle is derived from a combination of two different contributions:

- (i) The propagation time for a photon emitted at Cherenkov angle,  $\theta_c$ , is a function of  $\theta_c$ .
- (ii) The time of flight for the charged particle from the interaction point to the counter is a function of  $\beta$  of the particle and will therefore influence the arrival time of the Cherenkov photon at the photon detector.

The time-of-arrival difference between Cherenkov photons from a 3 GeV/c  $K$  and  $\pi$  hitting a TOP counter at 1 m from the photo detector, is about 75 ps. The time of flight difference is about 50 ps for a 1 m flight path. Compared to a DIRC counter [15], the TOP counter reconstructs the ring image using all timing information, including the TOF. This improves the separation power.

The baseline design is given in Fig. 10. The quartz radiators are  $75 \times 40 \times 2 \text{ cm}^3$  and  $185 \times 40 \times 2 \text{ cm}^3$ . The quartz is cut at  $\theta = 47.8$  degrees, where  $\theta$  is the polar angle in the Belle detector. The end surface of the longer part of the bar (covering  $\theta > 47.8$  degrees) is a spherical focusing mirror with a 5 m radius of curvature. The mirror's position is optimized to improve the PID power, because the separation between ring images is large when the propagation length is long, however, the timing resolution becomes worse due to dispersion as described later. Cherenkov photons are detected by a multi-anode micro-channel-plate photo-multiplier-tube (MCP-PMT). The time resolution is excellent,  $< 40 \text{ ps}$  [16]. The anodes are arranged in a linear array with 5 mm pitch. The MCP-PMTs are attached to the ends of the quartz bars as shown in Fig. 10. A multi-alkali photocathode is used in the standard version of such a MCP-PMT.

#### 2. GaAsP photocathode

Fig. 33 shows a simulation of the time distribution for a channel around the center of the TOP counter. It is clear that the improvement of the PID power is limited by the broadening of the time resolution due to the chromaticity of Cherenkov photons. From Fig. 33 we observe that the detection time is shifted by about 500 ps if wavelength changes from 300 nm to 600 nm.

One way to minimize this effect is to restrict the sensitivity window of the photon detector as shown in Fig. 34(a), and make use of the reduced velocity variation at longer wavelengths. Fig. 34(b) shows the QE of multi-alkali and GaAsP photocathodes as a function of wavelength. A GaAsP photocathode has a higher QE at longer wavelengths compared to the alkali photocathodes. The light propagation velocity spread, corresponding to the FWHM interval of the QE, is 0.181-0.201 m/ns for multi-alkali and 0.198-0.204 m/ns for GaAsP photocathodes, as shown in Fig. 34(a). The use of a GaAsP photocathode will therefore improve the time resolution for propagated photons.

We have been developing a square-shaped MCP-PMT with a GaAsP photocathode with Hamamatsu photonics K.K. (HPK). Fig. 35 shows a picture of the prototype. It has four anode strips, a

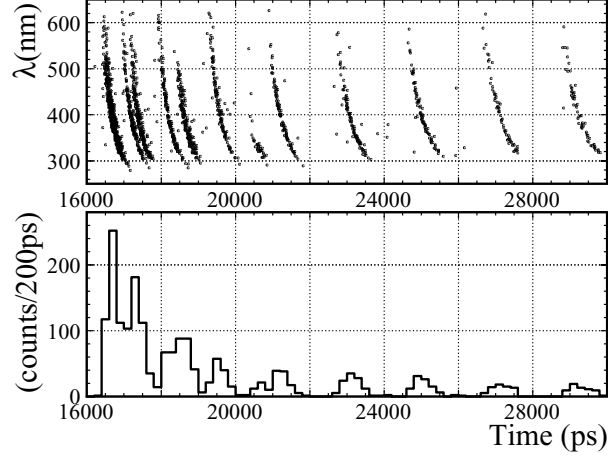


FIG. 33: Wavelength ( $\lambda$ ) dependence of the detection time (top) and the projected time distribution (bottom).

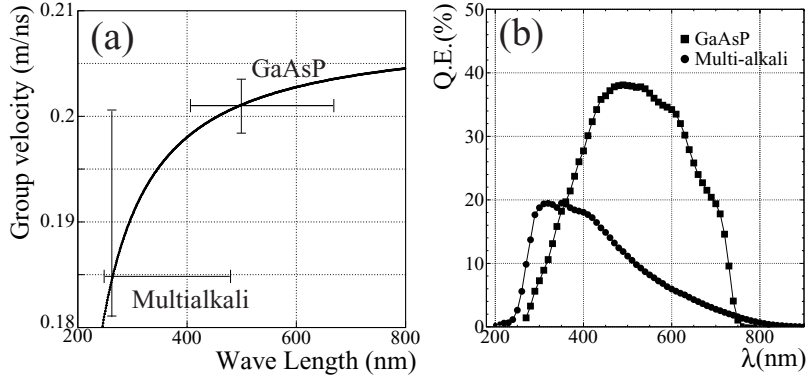


FIG. 34: Light propagation velocity inside quartz as a function of the wavelength  $\lambda$  (a), and quantum efficiency (b).

GaAsP photocathode and an aluminum protection layer on the first MCP to protect the photocathode from damage by feedback ions. The anode layout is also shown in Fig. 35.

We checked the time response for single-photon detection, using a picosecond laser (HPK; PLP-02-SLDH-041). The wavelength and pulse width are, respectively,  $405 \pm 10$  nm and 34 ps. The light intensity is reduced by a diffuser and filters down to the single-photon level. The photons

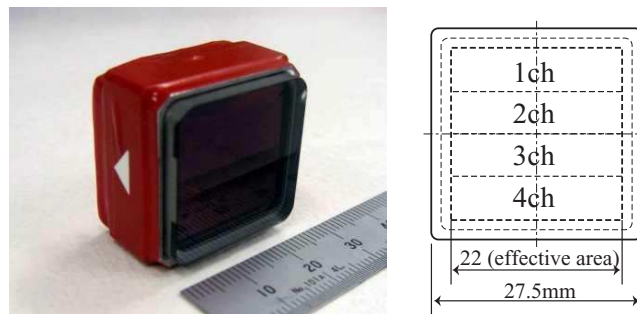


FIG. 35: Picture of a prototype MCP-PMT with the anode channel layout.

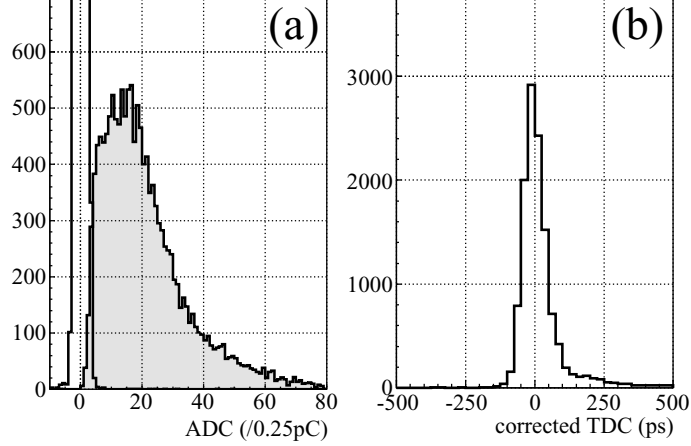


FIG. 36: ADC (a) and TDC (b) distributions of the GaAsP photocathode MCP-PMT for single-photon detection. In (a), the shaded histogram is the output charge for single photons within the corresponding time window, and the open histogram is the pedestal.

are led to the PMT window by an optical fiber. The output of the MCP-PMT is fed into an attenuator (Agilent; frequency  $< 18$  GHz) and an amplifier (HPK; C5594; gain = 36 dB; frequency, 50 kHz – 1.5 GHz), to avoid noise at the discriminator. The charge and timing are measured by an ADC, 0.25 pC/count, and a TDC, 25 ps/count. A discriminator (Phillips Scientific, model 708) is used with an threshold of 20 mV.

Fig. 36 gives the charge and timing distribution for single photons. The signal output is fast with a rise time of  $\sim 500$  ps. The gain is in the order of  $\sim 0.6 \times 10^6$ . We also obtained a good time resolution of  $\sim 35$  ps around the main peak.

### 3. Focusing system

Even when using the GaAsP photocathode MCP-PMT, the remaining chromatic effect contributes a 100 ps spread (rms) to the time of propagation. This is of the same order of magnitude as the time difference between  $K$  and  $\pi$  detection. To minimize the chromatic effect, we can introduce a focusing system. The refractive index,  $n$ , of quartz is well described by the following approximation within the range  $200 < \lambda < 900$  nm:

$$n(\lambda) = 1.44 + \frac{8.2}{\lambda - 126}$$

for  $\lambda$  in nm. The Cherenkov angle,  $\theta_c$ , depends on the photon wavelength according to

$$\cos \theta_c = \frac{1}{n(\lambda)\beta}.$$

We can therefore correct the chromaticity directly by using the  $\lambda$  dependence of  $\theta_c$ .

Fig. 37 shows the schematic set-up. A focusing mirror is introduced at the end of the longer quartz bar, and replaces PMTs in the previous TOP counter (3-readout type) version. The PMTs at the other end of the bar are rotated to measure the position of the photon impact in  $x$  and  $y$ . The cross section of the quartz bar is a rectangle. We can therefore expand the light trajectory into the mirror-image region and create a virtual readout screen, a matrix of  $22 \times 5$  mm<sup>2</sup> readout channels

as shown in Fig. 35. Cherenkov photons with different  $\theta_c$  will focus onto different PMT channels, and we thereby obtain  $\lambda$  information from the  $y$  detection position through  $\theta_c$ . We can reconstruct the ring image from 3-dimensional information on time,  $x$  and  $y$ .

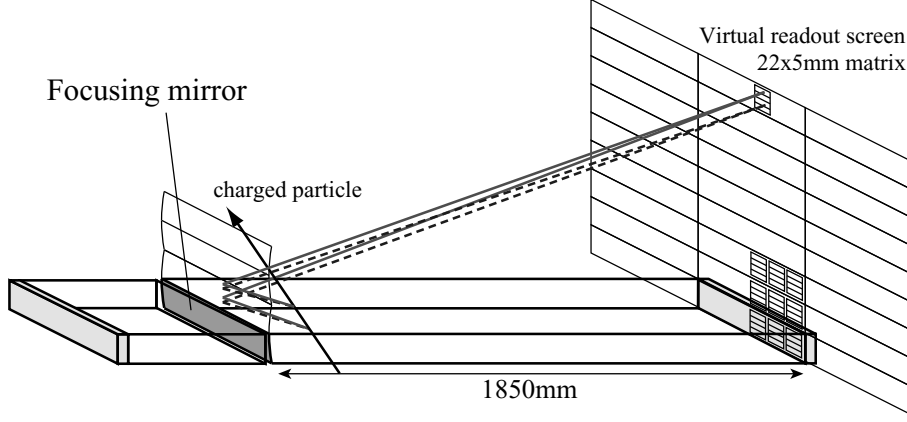


FIG. 37: Schematic view of the focusing system.

Across the restricted  $\lambda$  range,  $\theta_c$  varies by  $\sim 12$  mrad. The bar length from the mirror to the MCP-PMT is 1850 mm, as shown in Fig. 37. The corresponding difference in the  $y$  photon detection position is  $\sim 20$  mm, about four times the pad size, and comparable to the quartz thickness. We can therefore improve our estimate of  $\lambda$  and light propagation velocity, and consequently obtain improved performance, even with this narrow mirror and readout plane. The focusing TOP counter does not require a large focusing mirror and readout channels with high granularity.

The estimated performance of the focusing TOP is shown in Fig. 38. We evaluated the performance of the TOP counter with the GaAsP photocathode by simulating the Cherenkov photon generation, light propagation inside the quartz and the time fluctuation of the MCP-PMT. We have included in the simulation all chromatic effects. We have also applied a cut-off at 400 nm to the QE distribution and a collection efficiency of 36% for the MCP-PMT. The fake rate is improved by a factor of two and we obtain  $4.3\sigma$  separation for 4 GeV/ $c$  tracks.

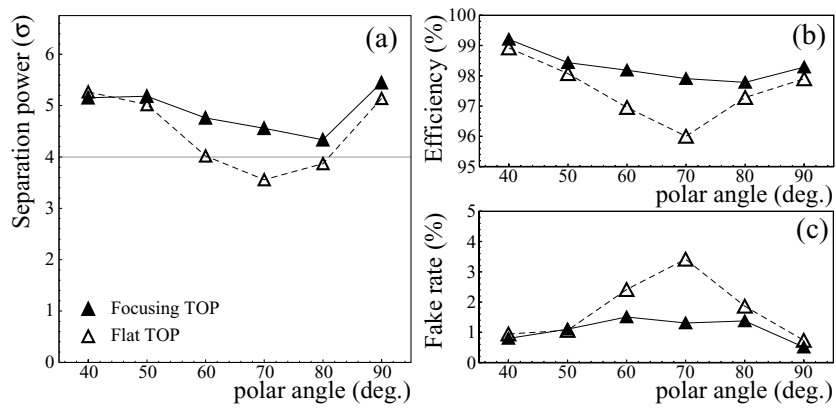


FIG. 38: (a) Separation power, (b) kaon efficiency and (c) pion fake rate for the 3-readout type ( $\Delta$ ) and the focusing type ( $\blacktriangle$ ).

TABLE XI: TOP configurations and their performance in terms of separation of  $K$  and  $\pi$  at 4 GeV/ $c$  and  $\theta = 70^\circ$ .

Configuration	Separation	Status
A) 3-readout and multi-alkali p.c.	$2.8\sigma$	Ready
B) 3-readout and GaAsP p.c.	$3.5\sigma$	PMT production and lifetime test
C) Focusing and multi-alkali p.c.	$2.5\sigma$	Focusing system test
C') C with CE=60%	$4.0\sigma$	Lifetime test
D) Focusing and GaAsP p.c.	$4.2\sigma$	PMT production and lifetime test

#### 4. TOP configurations

In the baseline design, we plan to use the MCP-PMT with a GaAsP photocathode. The key issue for the Belle upgrade is the lifetime of the photocathode. Because of the high beam background rate (we expect an increase by about a factor of 20 with respect to the present rate in the TOF counter), many Cherenkov photons from gamma-converted electrons will be detected. The current prototype MCP-PMT has an inadequate lifetime for the high intensity run. Although we are trying to improve the lifetime of the GaAsP photocathode, we are also developing a MCP-PMT with a multi-alkali photocathode as a backup option. Our study [17] shows a satisfactory lifetime, which was achieved when the multi-alkali photocathode has a thin aluminum layer on the first MCP surface. This layer protects the photocathode from damage by feedback ions. However, such a layer also reduces the collection efficiency (CE) by 40%. To recover the collection efficiency and maintain a long lifetime, we are developing a new type of MCP-PMT by changing the internal configuration, either with a protection layer on the second MCP surface, or with an additional MCP layer.

There are two possible radiator configurations, the 3-readout type and the focusing type. We plan to use the focusing type as the baseline design. Although the 3-readout type has simpler ring images compared to the focusing type, the ring-image separation of the focusing type is better than that of the 3-readout type.

The possible TOP configurations are summarized in Table XI. The focusing TOP with a GaAsP photocathode MCP-PMT has the best performance with  $4.2\sigma$  separation for  $K/\pi$  tracks at 4 GeV/ $c$  and  $\theta = 70$  degrees. The focusing type using a multi-alkali photocathode MCP-PMT with improved CE has a similar performance.

#### 5. $\phi$ coverage

The layout of the proposed TOP quartz radiators is shown in Fig. 39(left), and is similar to the structure of Babar's DIRC [15]. In this case, there is a gap between radiators. In addition, the TOP counter has an insensitive region of about 1 cm from the quartz edge due to the short path length of the curled tracks in the radiator bar. In total, we have about 10% (or less) dead space in the  $\phi$  direction in the barrel region.

To reduce this dead space, we consider an overlapping layout as shown in Fig. 39(right). We adopt this staggered layout to avoid charge asymmetry. In this case, we need wide quartz bars (50 cm width) and a complicated support structure. We also have to reduce the inner radius from

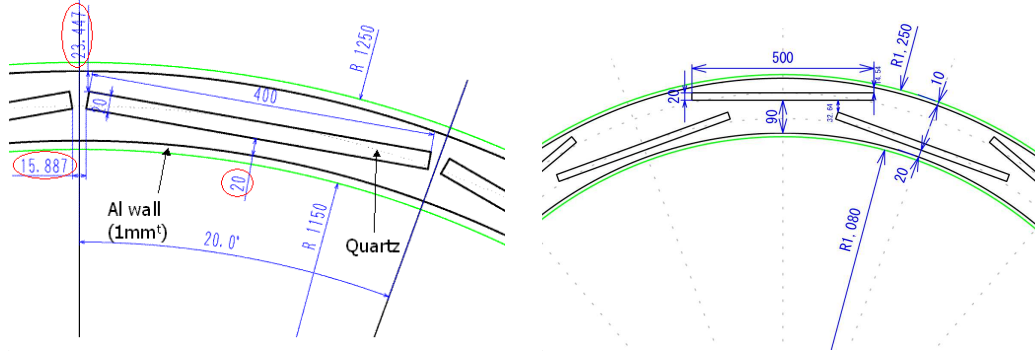


FIG. 39: Quartz radiator configurations in the  $r - \phi$  plane for a basic TOP (left) and for a layout with overlaps (right).

1150 mm to 1080 mm.

### B. Aerogel RICH Performance

The key issue in the performance of a RICH counter is the Cherenkov angle resolution per track  $\sigma_{\text{track}} = \sigma_{\theta}/\sqrt{N}$ . With a thicker radiator, the number of detected photons increases, but in a proximity focusing RICH the single photon resolution degrades because of the emission point uncertainty. As it turns out for a given geometry, the optimal thickness is around 20 mm [18, 19]. However, this limitation can be overcome in a proximity focusing RICH with a non-homogeneous radiator [19–22]. By appropriately choosing the refractive indices of consecutive aerogel radiator layers, one may achieve overlapping of the corresponding Cherenkov rings on the photon detector (Fig. 40) [22]. This represents a sort of focusing of the photons within the radiator, and eliminates or at least considerably reduces the spread due to emission point uncertainty. Note that such a tuning of refractive indices for individual layers is only possible with aerogel, which may be produced with any desired refractive index in the range 1.01–1.07 [23]. The dual radiator combination can readily be extended to more than two aerogel radiators. In this case, the indices of aerogel layers should gradually increase from the upstream to the downstream layer. In Fig. 40, we compare the data for two 4 cm thick radiators; one with aerogel tiles of equal refractive index ( $n = 1.046$ ), the other with the focusing arrangement ( $n_1 = 1.046, n_2 = 1.056$ ). The improvement is clearly visible. The single photon resolution  $\sigma_{\theta} = 14.3$  mrad for the dual radiator is considerably smaller than the corresponding value for the single refractive index radiator ( $\sigma_{\theta} = 20.7$  mrad), while the number of detected photons is the same in both cases.

The particle identification capabilities of the counter were evaluated by using simulated data. The backgrounds that are not included in the simulation (Rayleigh scattered Čerenkov photons from the same track, Čerenkov photons emitted by the same track in the photon detector window, beam related background hits and electronic noise) were added according to observed or expected rates. In the analysis of simulated events, the likelihood for the observed hit pattern is calculated for each hypothesis, and momentum dependent selection criteria are chosen for a given fake hypothesis probability [24]. The resulting identification efficiency for kaons is shown in Fig. 41; as expected we observe a clear advantage of using a focusing radiator compared to the homogenous one.

We have also investigated the performance of the counter in the region close to the boundary to the barrel PID device. As can be seen from Fig. 12, a sizable fraction of Cherenkov photons

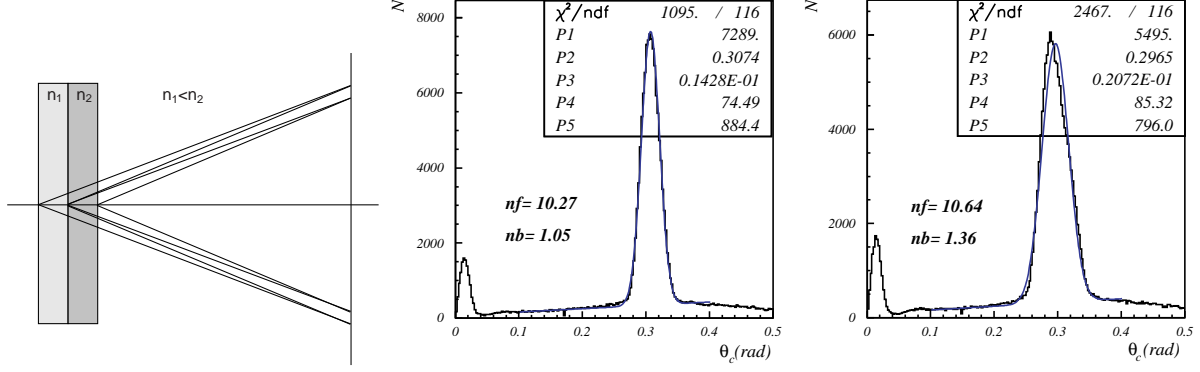


FIG. 40: Proximity focusing RICH with a nonhomogeneous aerogel radiator in the focusing configuration(left); the accumulated distribution of Cherenkov photon hits depending on the corresponding Cherenkov angle for a 4cm homogeneous radiator (right) and a focusing configuration with  $n_1 = 1.046$ ,  $n_2 = 1.056$  (center).

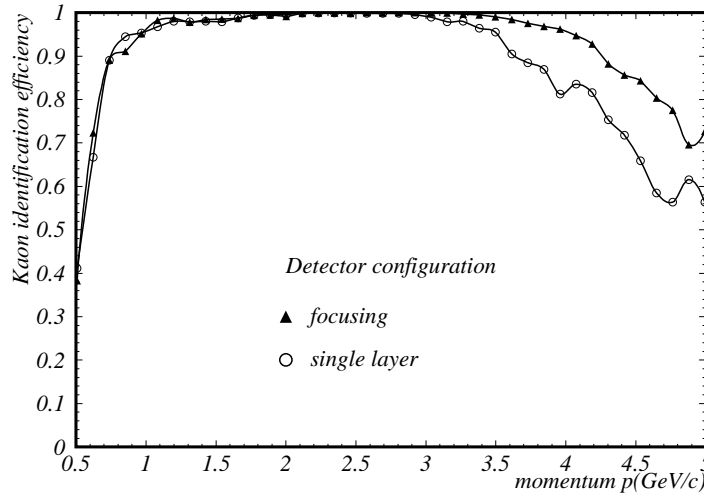


FIG. 41: Particle identification capability of the aerogel RICH counter: kaon efficiency at 1% pion misidentification probability for the focusing radiator configuration (triangles) compared to the homogenous radiator (open circles).

emitted by tracks close to this boundary do not hit the photon detector. This problem could in principle be overcome by inserting a planar mirror as illustrated in Fig. 42.



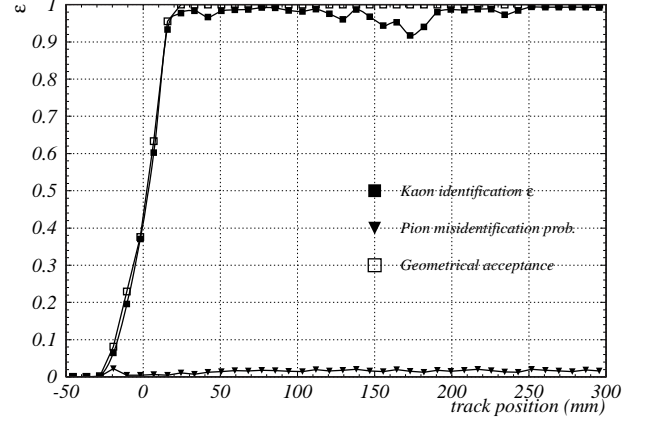
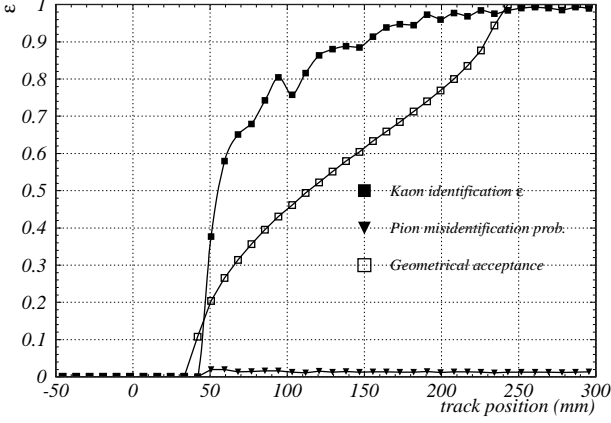


FIG. 42: Particle identification capability in the vicinity of the boundary to the barrel: kaon efficiency at 1% pion misidentification probability for the case with an additional planar mirror (right) and without it (left), shown as function of the distance from the boundary.

### C. Impact on $B \rightarrow \rho\gamma$ analysis

One of the important modes in which PID can contribute is  $B \rightarrow \rho\gamma$ . This mode suffers from a severe background from  $B \rightarrow K^*\gamma$  decays when the  $K$  from the  $K^*$  is misidentified as a  $\pi$ . We have therefore estimated the effect of an upgrade of the PID system on the analysis of this decay mode.

#### 1. TOP and ARICH performance with the simulator

In order to estimate the impact on the  $B \rightarrow \rho\gamma$  analysis, we use gsim and fsim6 simulators to describe the present Belle detector (ACC+TOF+ $dE/dx$ ) and the future sBelle detector (TOP+ARICH+ $dE/dx$ ), respectively.

In fsim6 with the nominal TOP configuration, the effective  $\phi$  coverage is assumed to be 90%, where the 10% insensitive region comes from the gap between the quartz bars and from the edge of the quartz bars where the PID efficiency is expected to be very low. In order to precisely estimate the actual  $\phi$  coverage, we have to make a real design of the supporting structure and study carefully the TOP performance for tracks that pass at the edges of bars, but we think that the assumption of 90% coverage is conservative. For the staggered quartz bar configuration, we assume the effective  $\phi$  coverage to be 100%. This assumption may be too optimistic, especially for low momentum tracks, but it is practical to study the impact of  $\phi$  coverage on the performance.

We first study the PID system performance for single tracks, generated uniformly over the laboratory solid angle ( $\cos\theta$ ). Figure 43 shows the efficiencies and mis-identification probabilities of  $K$  or  $\pi$  for two kinds of  $K$ - $\pi$  selection criteria using TOP and  $dE/dx$  for two TOP configurations (Fig. 43 (a) ~ (d)). Here, the performance of  $dE/dx$  at sBelle is assumed to be identical to the performance in the present Belle detector. The performance of the present PID (ACC, TOF and

TABLE XII:  $K$  efficiency (Eff.),  $\pi$  mis-identification rate (Fake) and separation (Sep.) for the selection  $LR(K, \pi) > 0.6$ .

	1 GeV/ $c$			2 GeV/ $c$			4 GeV/ $c$		
	Eff.(%)	Fake(%)	Sep.	Eff.(%)	Fake(%)	Sep.	Eff.(%)	Fake(%)	Sep.
ACC	71.2	6.4	2.1	83.6	3.2	2.8	38.8	14.4	0.8
ACC + $dE/dx$	76.2	7.3	2.2	86.9	3.8	2.9	84.4	6.0	2.6
ARICH	36.0	0.08	2.8	95.8	0.6	4.2	93.1	1.4	3.7
ARICH + $dE/dx$	48.2	0.06	3.2	99.5	0.4	5.2	98.6	1.0	4.5

TABLE XIII:  $\pi$  efficiency (Eff.),  $K$  mis-identification rate (Fake) and separation (Sep.) for the selection  $LR(K, \pi) < 0.1$ .

	1 GeV/ $c$			2 GeV/ $c$			4 GeV/ $c$		
	Eff.(%)	Fake(%)	Sep.	Eff.(%)	Fake(%)	Sep.	Eff.(%)	Fake(%)	Sep.
ACC	59.6	9.1	1.6	64.1	6.5	1.9	3.5	2.6	0.1
ACC + $dE/dx$	59.9	9.2	1.8	75.7	5.2	2.3	71.1	3.5	2.4
ARICH	99.5	37.4	2.9	94.8	0.12	4.7	89.6	0.38	3.9
ARICH + $dE/dx$	99.8	28.8	3.4	98.7	0.086	5.4	96.3	0.31	4.5

$dE/dx$ ) estimated using gsim is also shown for comparison (Fig. 43 (e), (f)). We can observe a significant improvement of the performance with the TOP detector. We can also see the effect of the  $\phi$  gap.

Similar distributions can be obtained for the endcap region. Figure 44 shows the efficiencies and mis-identification probabilities for  $K$ 's or  $\pi$ 's with the ACC and an ARICH. The performance can be expressed in terms of the separation, which can be calculated from the efficiency and mis-identification rate for certain selection criteria. Table XII (XIII) lists the  $K$  ( $\pi$ ) efficiencies and  $\pi$  ( $K$ ) mis-identification rates and the  $K$ - $\pi$  separations for a particular choice of selection criteria based on the likelihood ratio for the kaon and pion hypotheses,  $LR(K, \pi) > 0.6$  ( $LR(K, \pi) < 0.1$ ), for three momentum regions. The momentum regions denoted as 1 GeV, 2 GeV and 4 GeV correspond to the intervals  $0.8 < p < 1.2$  GeV,  $1.8 < p < 2.2$  GeV and  $3.5 < p < 4.0$  GeV, respectively.

## 2. Luminosity gain in $B \rightarrow \rho\gamma$

We consider the following PID configurations for the barrel region:

- (B1) Present ACC only. This corresponds to the case when the present PID device is used at Super KEKB and not only TOF but also  $dE/dx$  are conservatively assumed to be unusable.
- (B2) Present ACC and  $dE/dx$  only. This corresponds to the case when the present PID device is used at Super KEKB and  $dE/dx$  is assumed to work as at present.
- (B3) Present Belle PID (ACC, TOF,  $dE/dx$ ). This configuration is for reference, and does not correspond to any PID configuration at Super KEKB.

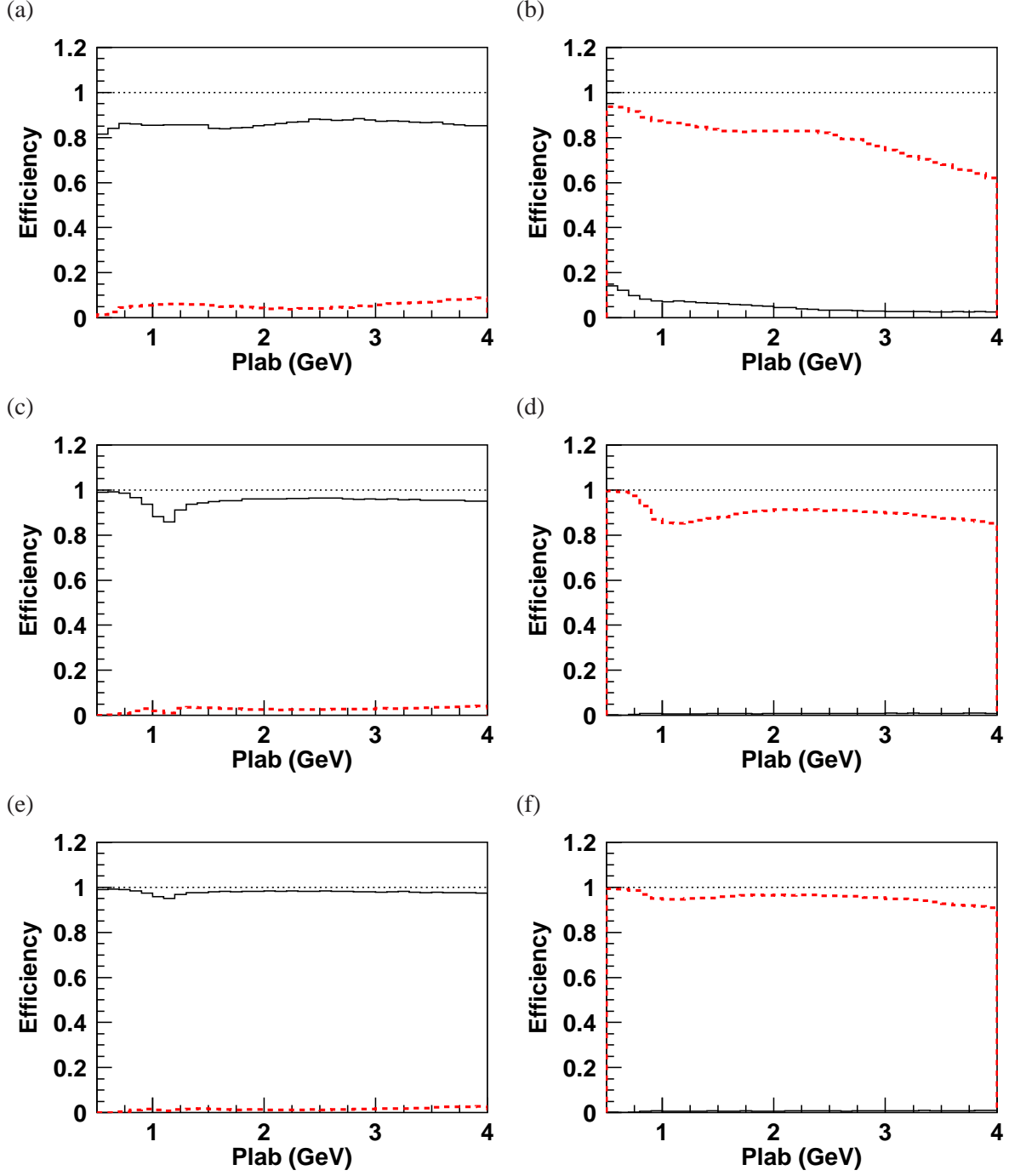


FIG. 43: Momentum dependence of the efficiencies for  $K$ 's (solid) and  $\pi$ 's (dashed) (a) for  $LR(K, \pi) > 0.6$  with the present barrel PID, (b) for  $LR(K, \pi) < 0.1$  with the present barrel PID, (c) for  $LR(K, \pi) > 0.6$  with TOP +  $dE/dx$ , (d) for  $LR(K, \pi) < 0.1$  with TOP +  $dE/dx$ , (e) for  $LR(K, \pi) > 0.6$  with TOP +  $dE/dx$  without a  $\phi$  gap, (f) for  $LR(K, \pi) < 0.1$  with TOP +  $dE/dx$  without a  $\phi$  gap.

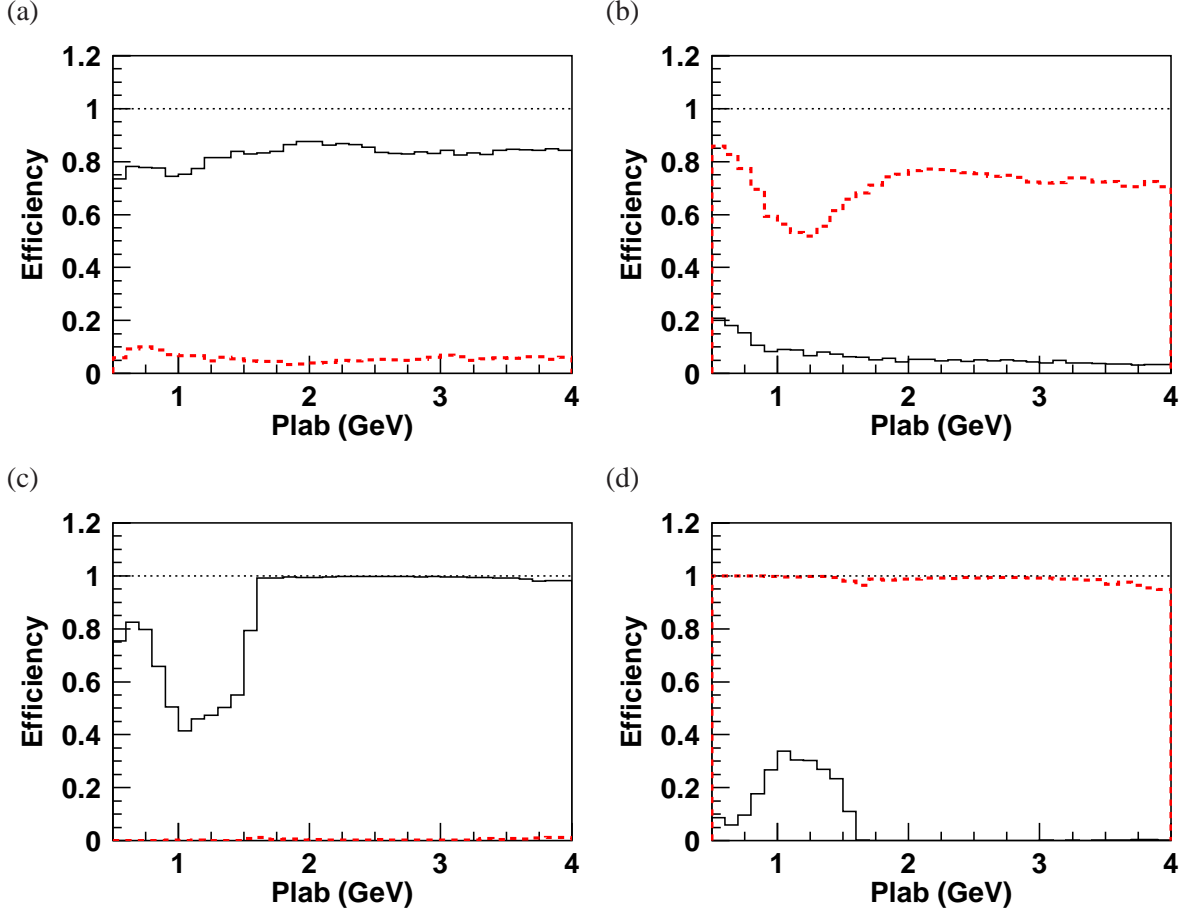


FIG. 44: Momentum dependence of the efficiencies for  $K$ 's (solid) and  $\pi$ 's (dashed) (a) for  $LR(K, \pi) > 0.6$  with the present endcap PID (b) for  $LR(K, \pi) < 0.1$  with the present endcap PID (c) for  $LR(K, \pi) > 0.6$  with ARICH +  $dE/dx$  (d) for  $LR(K, \pi) < 0.1$  with ARICH +  $dE/dx$ .

- (B4) TOP detector with the 3-readout scheme and a multi-alkali MCP, i.e., lower performance TOP.  $dE/dx$  is also assumed to work as at present.
- (B5) TOP detector with the focusing scheme and a GaAsP MCP.  $dE/dx$  is also assumed to work as at present.
- (B6) TOP detector with the focusing scheme and a GaAsP MCP without a  $\phi$  gap.  $dE/dx$  is also assumed to work as at present.

The simulations for (B1), (B2) and (B3) are done using the Geant 3 simulator gsim for the present Belle detector. The simulation for (B5) and (B6) is done with fsim. We do not have a simulator for configuration (B4), and we assume that the mis-identification rate is 5 times higher at 4 GeV and two times higher below 3 GeV compared to (B5).

Similarly, the following configuration is assumed for the forward endcap region:

- (F1) Present ACC only. This corresponds to the case when the present PID device is used at Super KEKB and  $dE/dx$  is conservatively assumed to be unusable.

(F2) Present Belle PID (ACC and  $dE/dx$ ). This corresponds to the case when the present PID device is used at Super KEKB and  $dE/dx$  is assumed to work as present. This configuration is also a reference for the present Belle PID.

(F3) ARICH detector.

(F4) ARICH detector with TOF information.

The simulations for (F1), (F2) are done using gsim for the present Belle. The simulation for (F3) is done with fsm. We do not have a simulator for configuration (F4), and we simply assume that the mis-identification rate below 1.5 GeV is half of that in (F3).

We reconstruct  $B^0 \rightarrow \rho^0 \gamma$  and  $B^+ \rightarrow \rho^+ \gamma$  for  $B \rightarrow \rho \gamma$  and  $B \rightarrow K^* \gamma$  MC samples. The selection criteria are similar to those in the recent Belle analysis. For simplicity, the contribution from the  $q\bar{q}$  background is assumed to be independent of the PID configuration. and is fixed to 2000 events for  $7.5 \text{ ab}^{-1}$ . We estimate the figure of merit (FOM) from the number of signal ( $B \rightarrow \rho \gamma$ ) events  $N_S$  and background ( $B \rightarrow K^* \gamma$  and  $q\bar{q}$  background) events  $N_B$  in the signal region. Here, the signal region is defined by  $M_{bc} > 5.27 \text{ GeV}$  and  $\Delta E_{\min} < \Delta E < 0.08 \text{ GeV}$ , where  $\Delta E_{\min}$  is chosen for each PID configuration to maximize the FOM.

Tables XIV and XV list the FOM for various detector configurations. The  $\Delta E$  distributions for two typical configurations, PID configuration B3 and F2 that correspond to the present PID performance and configuration B5 and F3 corresponding to TOP and ARICH, are shown in Fig. 45. As seen from Fig. (a) and (b), the suppression of the  $K^* \gamma$  component is quite significant with the TOP and the ARICH. The contribution of the  $K^* \gamma$  component below  $-0.2 \text{ GeV}$  contains events that are not due to a simple mis-identification between  $K$  and  $\pi$  but come from mis-reconstruction. In (b), because the mis-identification is highly suppressed by good PID devices, such mis-reconstructed events become visible. For the  $B^+ \rightarrow \rho^+ \gamma$  case ((c) and (d)), we can also observe a significant improvement in the analysis, although the effect is smaller if compared to the  $\rho^0 \gamma$  channel because mis-reconstructed events already represent a significant fraction of the background in the present detector.

Tables XVI and XVII show the “luminosity gain” compared to the present PID performance (configuration B3 and F2). The luminosity gain is defined as a square of the ratio of the FOM, and is the luminosity ratio that would be necessary to obtain the same sensitivity with the nominal PID configuration. The rows corresponding to B1 and B2 of the two tables show that the present Belle detector cannot be used at sBelle because the TOF counter cannot operate reliably in such an environment. The rows corresponding to B4 and B5 of Table XVI show that the introduction of the TOP detector is essential for this mode. The F3 and F4 columns show that the ARICH further improves the performance.

The reduction of the  $\phi$  gap in the TOP counter also seems to be of some benefit as can be seen from B6, where the coverage of the TOP counter in the  $\phi$  direction is assumed to be 100%. However, this assumption might be too simple for the staggered-bar option, and more studies are needed to resolve this question.

TABLE XIV: Number of signal ( $N_S$ ) and background ( $N_B$ ) events, figure of merit (FOM), and the  $\Delta E$  lower limit  $\Delta E_{\min}$  chosen for each barrel and forward PID configuration for  $B^0 \rightarrow \rho^0 \gamma$  analysis at  $7.5 \text{ ab}^{-1}$ . See the text for an explanation of the configuration label.

Barrel	Forward	$N_S$	$N_B$	FOM	$\Delta E_{\min}$ [GeV]
B1	F1	427	3998	6.4	-0.10
B1	F2	474	4021	7.1	-0.10
B1	F3	510	3846	7.7	-0.10
B1	F4	510	3836	7.7	-0.10
B2	F1	714	4791	9.6	-0.20
B2	F2	800	5254	10.3	-0.30
B2	F3	813	4609	11.0	-0.20
B2	F4	813	4590	11.1	-0.20
B3	F1	930	5207	11.9	-0.25
B3	F2	987	5242	12.5	-0.25
B3	F3	1032	5026	13.3	-0.25
B3	F4	1032	5002	13.3	-0.25
B4	F1	924	3389	14.1	-0.30
B4	F2	982	3422	14.8	-0.30
B4	F3	1027	3208	15.8	-0.30
B4	F4	1027	3180	15.8	-0.30
B5	F1	924	2832	15.1	-0.30
B5	F2	982	2865	15.8	-0.30
B5	F3	1027	2651	16.9	-0.30
B5	F4	1027	2623	17.0	-0.30
B6	F1	1060	2857	16.9	-0.30
B6	F2	1118	2890	17.7	-0.30
B6	F3	1163	2677	18.8	-0.30
B6	F4	1163	2648	18.8	-0.30

TABLE XV: Number of signal ( $N_S$ ) and background ( $N_B$ ) events, figure of merit (FOM), and the  $\Delta E$  lower limit  $\Delta E_{\min}$  chosen for each barrel and forward PID configuration for  $B^+ \rightarrow \rho^+ \gamma$  analysis at  $7.5 \text{ ab}^{-1}$ . See the text for an explanation of the configuration label.

Barrel	Forward	$N_S$	$N_B$	FOM	$\Delta E_{\min}$ [GeV]
B1	F1	1014	3775	14.7	-0.30
B1	F2	1034	3681	15.1	-0.30
B1	F3	1076	3656	15.6	-0.30
B1	F4	1076	3626	15.7	-0.30
B2	F1	997	3197	15.4	-0.30
B2	F2	1017	3103	15.8	-0.30
B2	F3	1059	3078	16.5	-0.30
B2	F4	1059	3048	16.5	-0.30
B3	F1	1132	3100	17.4	-0.30
B3	F2	1152	3006	17.9	-0.30
B3	F3	1194	2981	18.5	-0.30
B3	F4	1194	2951	18.5	-0.30
B4	F1	1121	2950	17.6	-0.30
B4	F2	1141	2856	18.0	-0.30
B4	F3	1183	2831	18.7	-0.30
B4	F4	1183	2802	18.7	-0.30
B5	F1	1121	2584	18.4	-0.30
B5	F2	1141	2490	18.9	-0.30
B5	F3	1183	2465	19.6	-0.30
B5	F4	1183	2436	19.7	-0.30
B6	F1	1174	2597	19.1	-0.30
B6	F2	1194	2503	19.6	-0.30
B6	F3	1236	2478	20.3	-0.30
B6	F4	1236	2448	20.4	-0.30

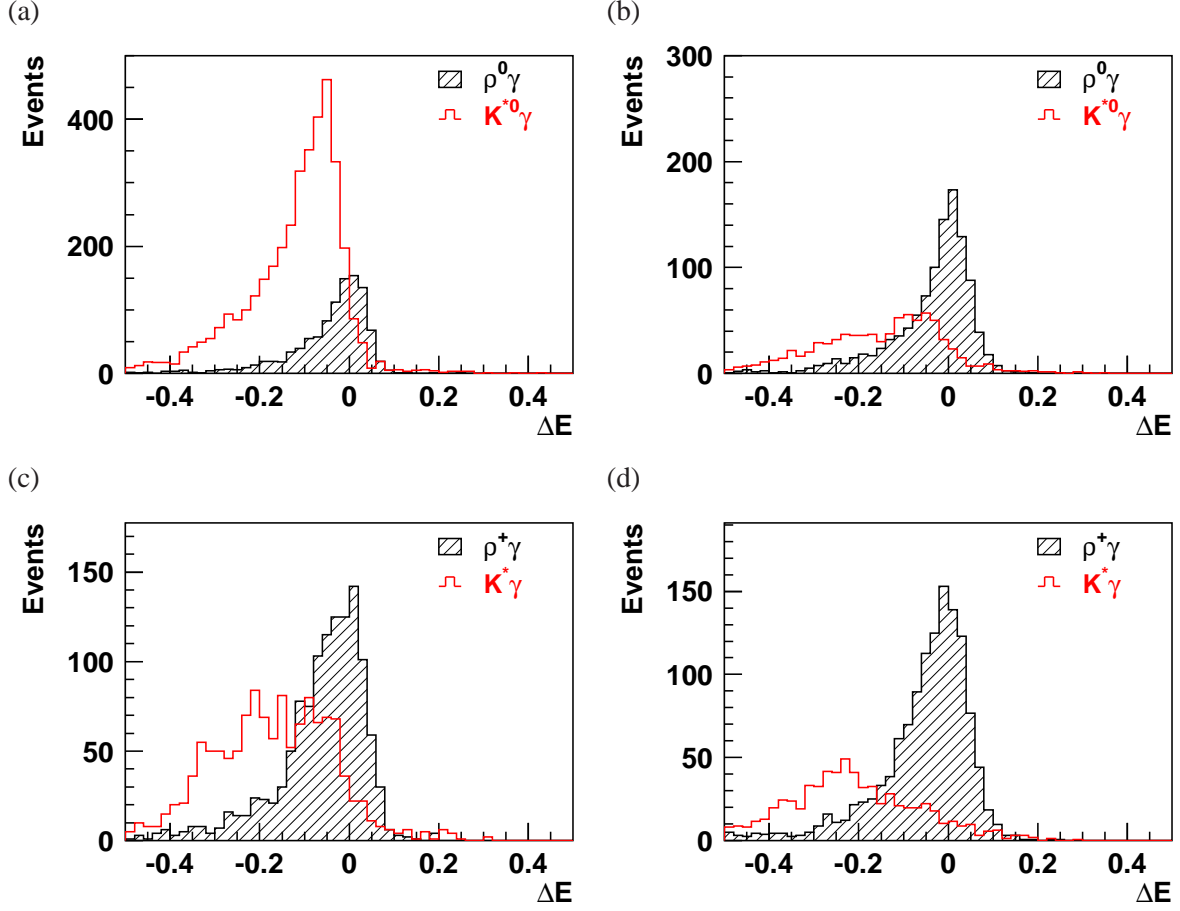


FIG. 45: Expected  $\Delta E$  distribution at  $7.5 \text{ ab}^{-1}$  for (a)  $B^0 \rightarrow \rho^0\gamma$  with present PID performance (B3 and F2), (b)  $B^0 \rightarrow \rho^0\gamma$  with TOP and ARICH (B5 and F3), (c)  $B^+ \rightarrow \rho^+\gamma$  with present PID performance (B3 and F2), (d)  $B^+ \rightarrow \rho^+\gamma$  with TOP and ARICH (B5 and F3).

TABLE XVI: Luminosity gain for  $B^0 \rightarrow \rho^0\gamma$  for various detector configurations.

	F1	F2	F3	F4
B1	0.26	0.32	0.38	0.38
B2	0.59	0.68	0.78	0.78
B3	0.90	1.00	1.12	1.13
B4	1.27	1.40	1.59	1.60
B5	1.45	1.60	1.83	1.85
B6	1.83	1.99	2.25	2.27

TABLE XVII: Luminosity gain for  $B^+ \rightarrow \rho^+\gamma$  for various detector configurations.

	F1	F2	F3	F4
B1	0.67	0.71	0.77	0.77
B2	0.74	0.79	0.85	0.86
B3	0.95	1.00	1.07	1.08
B4	0.97	1.02	1.09	1.10
B5	1.06	1.12	1.20	1.21
B6	1.14	1.21	1.29	1.30



## VII. ECL PERFORMANCE

For the electromagnetic calorimeter, ECL, overlapping beam-background events will degrade the performance. The mean shift of energy distribution due to this background source can be calibrated in principle, but the energy resolution will be worse and cannot be recovered unless we resolve the contribution from the background. Therefore, we will upgrade the readout electronics so that we can sample and fit the signal waveform. With waveform fitting two overlapping waveforms can be resolved if they are separated by more than about one peaking time. From a toy MC study, in which we assume a flat background distribution in time, the background reduction factor is estimated to be seven in the energy range above 20 MeV where the background hits create fake clusters.

On the other hand, in the energy range below 20 MeV, the effect of the beam-background is similar to electric noise; we call this low energy background “pileup noise”. The waveform fitting does not have great suppression power for the pileup noise, compared to its suppression of fake clusters; the suppression factor is two for the pileup noise. The magnitude of the pileup noise,  $\sigma_p$ , is proportional to the fluctuation of the background, which is,

$$\sigma_p \propto \sqrt{\nu\tau(\bar{\epsilon}^2 - \bar{\epsilon}^2)},$$

where  $\nu$  is the rate of the photons,  $\tau$  is effective duration of the signal,  $\bar{\epsilon}$  and  $\bar{\epsilon}^2$  are the mean and the square mean of the photon energies. Therefore, the background suppression factor for the pileup noise by waveform fitting is four ( $\sqrt{N}/2 = \sqrt{N/4}$ ). A concern is only in the low energy photon reconstruction, which should be examined in the analysis of  $B \rightarrow D^*K$ ,  $D^* \rightarrow D\gamma$  or  $D\pi^0$ .

For higher background levels when the suppression by waveform fitting is not sufficient, CsI(Tl) has to be replaced with pure CsI crystals. This is planned for both endcaps. Because of the shorter time constant for pure CsI ( $\sim 30$  ns) compared to CsI(Tl) ( $\sim 1$   $\mu$ s), a background reduction of about 30 is expected. Since the light output will be lower and the wavelength of the scintillation light will be in the UV region, photomultiplier tubes have to be used instead of PIN photodiodes. The biggest issue for pure CsI crystals is the cost. The number of crystals that we can replace will depend on the available budget. In the following subsections, effects of a partial upgrade with pure CsI are discussed.

### A. Partition of endcaps

If only a part of the endcaps is upgraded with pure CsI crystals, a choice on the location of the pure CsI part has to be made. There are several possible partitions of the two regions. Two ways of partitioning are under consideration,

- **(A):** Forward innermost 4 rings (224), middle 5 rings (448) and outermost 4 rings (480)  
Barrel (6624)  
Backward innermost 6 rings (480), and outermost 4 rings (480),
- **(B):** Forward innermost 5 rings (288), next 2 rings (192), next 2 rings (192) and outermost 4 rings (480)  
Barrel (6624)  
Backward innermost 3 rings (192), next 1 ring (96), next 2 rings (192) and outermost 4 rings (480),

where the numbers in parentheses are the numbers of crystals in each partition. The difference between the two turn out to be minor, and are not crucial for the conclusion of the studies in this section.

### B. Study of $B \rightarrow K_S^0 \pi^0 \gamma$ decays

Assuming that the readout electronics will be upgraded and that waveform fitting will give us a background suppression by a factor of 7 as expected, 20 times more background corresponds to 3 times more background for the case with CsI(Tl), while we will be essentially free from background for the case with pure CsI. The effect of a partial upgrade with pure CsI on  $B \rightarrow K_S^0 \pi^0 \gamma$  is studied with partitioning scheme A. Using exp 55 MC, we overlaid 3 times more background to the part with CsI(Tl), while no background is overlaid on the part with pure CsI. For detectors other than ECL, 3 times more background is overlaid in all cases for technical reasons.

Several combinations of partitions are tested. Each configuration is identified with a 6 digit identifier like 033000, where each digit represents the background multiplication factor; the left-most digit refers to the most backward (largest in theta) partition, and the rightmost digit to the most forward (smallest in theta) partition. Hence in the example given above, 033000, corresponds to no background in the backward innermost 6 rings, 3 times more background in the backward outermost 4 rings, 3 times more background in the barrel, and no background in the forward endcap. Note that the present conditions correspond to 111111.

As shown in Fig. 46, in the case of 333333 (green, with filled circles), the mean of the  $\Delta E$  distribution is shifted towards the positive side, the width becomes larger, and the signal yield is lower compared to 111111 (black solid histogram); these are consequences of the background superposition. We observe a similar deterioration also in the case of 003000 (red, with open circles), namely the case with both forward and backward endcaps fully upgraded to pure CsI. Other configurations (003300, 003333, 033000, 033300, 033330, 033333, 333000, 333300 and 333330) are also tested; it is found that the corresponding performance is between the performances for 003000 and 333333. This deterioration corresponds to a 10 to 15 percent loss of luminosity, depending on the number of pure CsI crystals.

Note that in this decay photons with relatively high energy are produced as shown in Fig. 47. The analysis can be performed using the barrel ECL. Therefore, the impact of having pure CsI in the endcaps on this mode is not very large, although it is preferable to have a larger number of pure CsI crystals.

### C. Full reconstruction of $B$

Events where one of the  $B$  meson decays is fully reconstructed, are of particular importance in studies of rare decays such as  $B \rightarrow \tau \nu$  and  $B \rightarrow K \nu \nu$ . The main role of ECL in full reconstruction is to identify photons and  $\pi^0$ 's. It is therefore useful to understand the contribution of photons in the fully reconstructed events. Figure 48(left) shows the smallest and largest  $\theta$  indices of the photons in each of the correctly reconstructed MC events without overlaid background. Peaks at the theta indices = 0 and 70 correspond to events without photons in the final state. Those events, which account for about 30% of total events currently used for the full reconstruction, are not relevant for the ECL performance study. Figure 48(right) shows the integrals of the two distributions. From the figure the maximum contributions for the forward (index 1–13) and for the backward side (index 59–69) are estimated to be at most 14% and 5%, respectively.

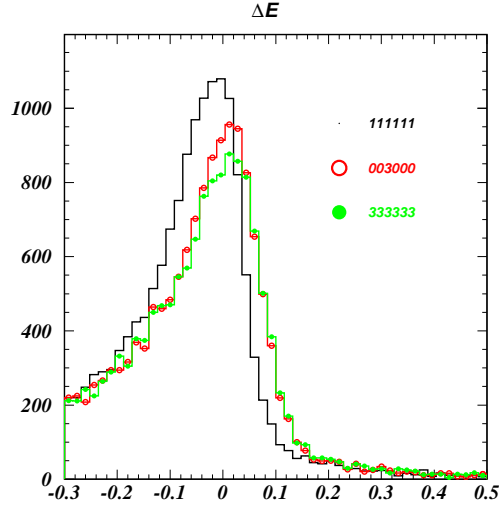


FIG. 46:  $\Delta E$  distributions for  $B \rightarrow K_S^0 \pi^0 \gamma$  decays for several background conditions.

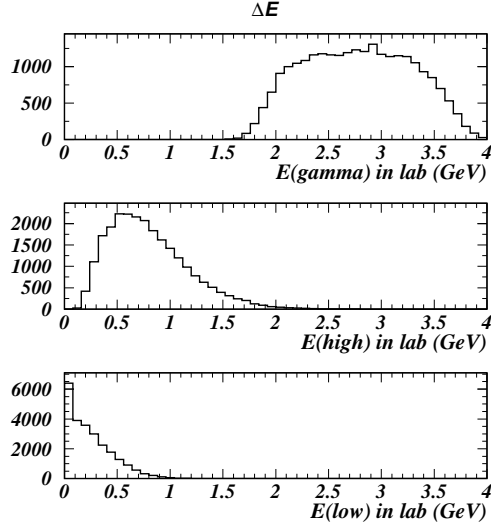


FIG. 47: Laboratory energy distribution of three photons in the  $B \rightarrow K_S^0 \pi^0 \gamma$  decay sequence: the primary photon from the  $B$  decay (top) and the two photons from the  $\pi^0$  decay ordered by energy (middle and bottom).

Also note that the introduction of waveform sampling reduces the pile-up by a factor of seven. This means that the performance will be better than at present until the beam background becomes seven times higher. This is expected to occur when the beam current is about three times higher.

The effect of partial replacement was studied as described in the previous subsection, except that the partitioning was according to scheme B. In this case the nominal background level was chosen as two times the background level of experiment 49. The background level in the region with the crystals replaced with pure CsI is again assumed to be zero. The reconstruction efficiency is estimated using MC events where one of the  $B$  mesons decays to the final states included in

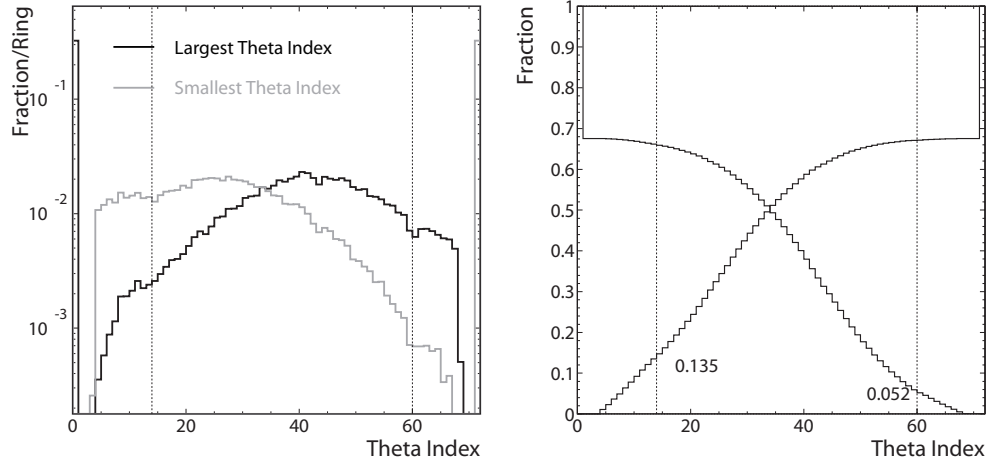


FIG. 48: Left: Minimum/Maximum  $\theta$  of photons in fully reconstructed  $B$  events with nominal background. Right: Fraction of events integrated over angle.

the full-reconstruction algorithm. The other  $B$  is forced to decay to a neutrino. The combinatorial background from real  $B$  decays is estimated using generic  $B$  decay MC. To obtain the contribution from combinatorial background, the  $m_{bc}$  distribution is fitted with a Gaussian signal and with Argus background shapes. The integral of the fitted Argus background is taken as the combinatorial background. Note that the peaking background in the  $m_{bc}$  distribution is not considered here. From the MC study, about one third of the Gaussian signals in the generic  $B$  MC events actually originates from the combinatorial background. The background from light flavor production is estimated using udsc-mixed MC events.

Figure 49 summarizes the effect of background in various partial upgrade conditions. The configuration type is indicated with a convention similar to the previous subsection. In this case there are four subdivisions in each of the endcaps. So the number of digits is nine, FFFFbBBBB, where F/b/B are the forward/barrel/backward, respectively. In the figure the variables are normalized to the case with two times overlaid background. The numbers in the parentheses are the numbers of crystals replaced by pure CsI. The efficiency increase and background reduction by a full replacement, i.e., with 2112 pure CsI crystals, is about 5%. The effect is very small when the number of replaced CsI crystals is below 960.

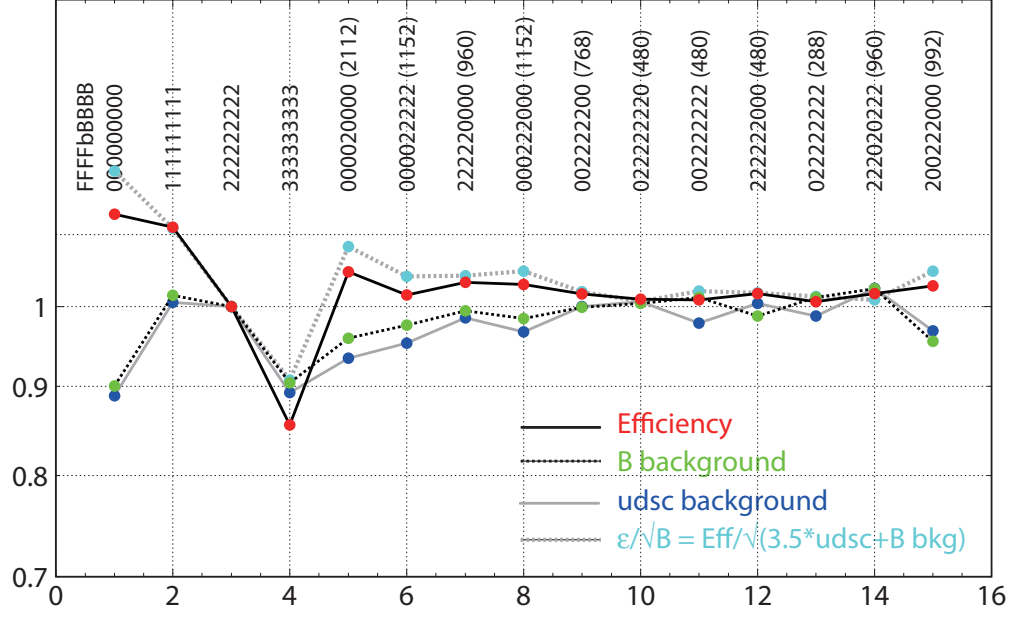


FIG. 49: Effect of a partial upgrade of the ECL. Black solid line, black dashed line and gray solid line show signal efficiency,  $B$  combinatorial background, and background from light flavors normalized to the case with two times background overlaid, respectively. Also shown by a gray dashed line is the efficiency divided by the square root of background. Numbers in parentheses are the numbers of crystals replaced with pure CsI. The nine digit numbers indicate the background level factor for each of the nine detector regions.

## VIII. $K_L^0$ RECONSTRUCTION

In the design studies for the existing Belle detector, the KLM subsystem's segmented geometry was chosen to enhance the reconstruction of  $K_L^0$  mesons arising from  $B \rightarrow J/\psi K_L^0$  decays for time-dependent  $CP$  asymmetry measurements. Indeed,  $K_L^0$  reconstruction in Belle has led to high quality  $CP$  asymmetry measurements in  $B \rightarrow J/\psi K_L^0$  as well as in other rare  $B$  decay modes such as  $\phi K_L^0$  and  $\eta' K_L^0$ .

In the sBelle era,  $K_L^0$  reconstruction will be driven not only by these time-dependent  $CP$  asymmetry measurements but also as a veto of backgrounds in rare decay modes with neutrinos such as  $B \rightarrow \tau \nu$ . In this section, we study the extent to which we can improve the sensitivity of  $B \rightarrow \tau \nu$  via enhancement of  $K_L^0$  reconstruction compared to the current Belle detector and discuss the possibility of implementing such enhancements.

### A. Impact of $K_L^0$ reconstruction improvement to $B \rightarrow \tau \nu$

A large Monte Carlo simulation sample shows that about  $78 \pm 1\%$  of the background events remaining in the signal region of  $B \rightarrow \tau \nu$  have at least one  $K_L^0$  among the final state particles. In particular, the dominant background component that peaks in the signal region arises from  $b \rightarrow c$  semileptonic decays where the charm-meson daughter decays to a  $K_L^0$ . Therefore, an effective  $K_L^0$  veto would be very useful to reduce this background; in particular, an enhancement of  $K_L^0$  detection efficiency is very desirable.

Based on the GEANT simulation of the existing KLM and the measured detection efficiency (from  $J/\psi K_L^0$  data), the  $K_L^0$  veto efficiency is estimated to be 35%. We use these data to estimate the improvement in the significance of the  $B \rightarrow \tau \nu$  signal with a higher  $K_L^0$  veto efficiency. For the signal and background ratio, we use our published measurement of  $B \rightarrow \tau \nu$  obtained from 447 million  $B\bar{B}$  events. The loss in signal efficiency due to accidental  $K_L^0$  vetoes, which is estimated to be about 15% from MC simulation, is taken into account in this study.

Figure 50 shows the  $B \rightarrow \tau \nu$  sensitivity in terms of the required luminosity ratio to achieve a particular sensitivity for several  $K_L^0$  veto efficiency cases. Smaller values on the vertical axis (luminosity ratio) are better. From the figure, a  $PKzL$  veto efficiency of 70% (i.e., double the present value) corresponds to a remarkable 30% reduction in the required luminosity.

### B. Possibility of $K_L^0$ reconstruction improvement

The present algorithm for  $K_L$  identification is based on requiring nearby hits in at least two RPC superlayers (“KLM-only”) or an ECL cluster matching geometrically with an RPC hit (“ECL-KLM”). (All RPC hits are three-dimensional: the orthogonal cathode strips give two coordinates, while the RPC plane's position gives the third.) One possible way to increase the efficiency without changing the present iron-plate configuration is to relax the requirement of the KLM-only class to at least one hit in a detector superlayer. This increases the efficiency of  $K_L$  reconstruction by a factor of  $\sim 1.3$ , according to the GEANT3 simulation. A more robust estimation, using better hadronic-shower simulation, will be developed with the new GEANT4 Monte Carlo simulation.

Relaxing the  $K_L$  identification requirement to a single superlayer increases the fraction of neutrons misidentified as  $K_L$  mesons. This is exacerbated with increased luminosity, since all of the neutrons arise from beam backgrounds.

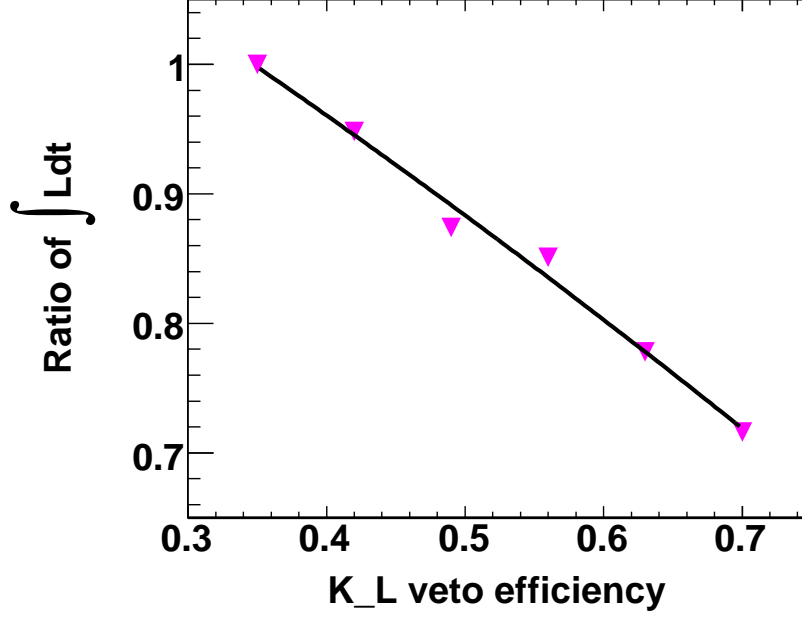


FIG. 50: The required-luminosity dependence on the  $K_L$  veto efficiency in  $B \rightarrow \tau\nu$ . The vertical axis is the relative luminosity needed to achieve a given signal sensitivity; smaller values are better.

In the scintillator endcaps, the independent operation of the two orthogonal scintillator planes within a superlayer considerably reduces this neutron background, since one neutron typically is absorbed in a single scintillator strip. This is a distinct advantage over the RPCs, where a neutron interaction within the active volume produces hits on both orthogonal cathode planes. Such backgrounds can be further suppressed in the scintillator endcaps by using fast electronics and taking advantage of the sub-ns time resolution of the scintillator detectors. Using a signal gate of 10 ns, the neutron background drops to  $\sim 0.5$  per event in the entire endcap KLM. This  $K_L$  misidentification rate gives too high an accidental signal veto of  $B \rightarrow \tau\nu$ , but this estimate may be overestimated because

- the background neutron rate may actually be smaller, while it enters as a square.
- we ignored the fact that some fraction of the strips in two layers do not overlap
- the outermost endcap superlayers (with the highest neutron rate) are not useful for the  $K_L$  veto and can be excluded.

There are additional possibilities to reduce the background rate:

- use a higher threshold (at  $\sim 0.6$  MIP) for  $K_L$  identification in case of a single superlayer cluster. This reduces the final coincidence rate by a factor of  $\sim 4$ . However this option requires a modification of the electronics (an additional discriminator).
- require an additional nearby hit within the same superlayer. The final random coincidence rate will be reduced by a roughly a factor of 250. However, the efficiency of such requirement cannot be determined without a full GEANT4 simulation.
- use three scintillator planes per superlayer.



### C. Summary

An enhancement of  $K_L^0$  identification will have a large and beneficial impact on the measurement of the decay modes with neutrinos such as  $B \rightarrow \tau\nu$ . One way to enhance the  $K_L^0$  identification is to relax the  $K_L$  definition in the scintillator endcaps to one or more struck superlayers. Our preliminary MC study shows that a factor of 1.3 improvement in the  $K_L$  identification efficiency is possible. This corresponds to about a 30% reduction in the luminosity required to achieve a given  $B \rightarrow \tau\nu$  signal sensitivity. Of concern is the increase of the  $K_L$  misidentification rate due to stray neutrons. A conservative estimate indicates that  $\sim 0.5$  neutrons will be misidentified as  $K_L$  mesons per event in the sBelle scintillator-based endcap. However, it may be possible to improve the background rate by optimizing the electronics and the reconstruction algorithm.

## IX. MATERIAL EFFECTS

In detector design, the material budget is always a big issue. This is especially true in a  $B$ -factory experiment, since the momenta of particles that we measure are relatively low and the effect of multiple scattering can be critical to determine  $B$  decay vertices with good precision. We must pay special attention to this issue, because some of the layers of the upgraded SVD are expected to have readout chips on sensors instead of at the edges of the sensor chain as in the present detector. This implies that all the necessary massive structure for cooling will also be inside the detector acceptance.

The robustness of the calorimeter performance should be checked. Photon conversions at detector components in front of the calorimeter can result in detection inefficiencies. If a conversion occurs just in front of the calorimeter, we can still reconstruct the electromagnetic shower, but components with sizable amount of material placed far from the ECL should be avoided. In this respect, replacing the current ACC detector with the TOP counter is expected to improve the calorimeter performance.

### A. Track and vertex reconstruction

As discussed in the beam background section II, the SVD will be exposed to harsh beam background under the target luminosity. The beam background in the SVD could be about 15 times higher than in the current Belle detector. To cope with this, we decided to replace the current VA1TA readout chips with APV25 chips. Since the APV25 has a pulse width 16 times shorter than the VA1TA, the rate at which beam background pulses overlap with the signal will decrease accordingly.

However, to realize the shorter pulse width we have to compromise on the signal-to-noise (S/N) ratio. In particular, for the outer layers several silicon sensors could be connected and read out by a chip located at one end of the sensor chain. In that case the S/N ratio would be about 4 times worse than for the current SVD. Recently, an attractive new technique has been proposed, the so-called “chip-on-sensor”, where readout chips are attached to each silicon sensor to reduce the deterioration of the S/N ratio. However, this leads to an increase in the amount of material within the tracking acceptance region. Furthermore, the total number of readout channels would drastically increase.

For sBelle, the  $B \rightarrow K^{*0}\gamma$  decay (reconstructed in  $K_S^0\pi^0\gamma$ ) is one of the most important modes used to explore physics beyond the Standard Model. Only charged decay products of the  $K_S^0$  from the  $K^{*0} \rightarrow K_S^0\pi^0$  decay chain are available for the reconstruction of the  $B$  decay vertex. To improve the detection efficiency for  $B \rightarrow K^{*0}\gamma$ , we have decided to extend the SVD detector volume in the radial direction from a 4-layer to a 6-layer configuration, while keeping the same tracking acceptance for the CDC. However, this change requires longer silicon sensors, which in turn leads to a deterioration of the S/N ratio of the readout chips. The two additional layers also contribute to an increase in the amount of material.

In terms of the CDC, to reduce the high occupancy induced by the harsh beam background, we will make the cell size smaller and increase the number of sense wires by roughly a factor of two. This proposal implies that the amount of material in the CDC will increase and that the tracking performance could deteriorate.

Therefore, to estimate the effects that stem from the required beam background tolerance and the impact on physics, simulation studies are performed. The in-depth report related to the SVD itself (optimization of the layer position, a study of a wider readout pitch size, the effect of a

poorer S/N ratio) was presented in section IV. In this section, we discuss the impact of the additional material on the charged particle tracking and vertexing, while its effect on the calorimetry is described in the next subsection (IX B).

### 1. Tracking Performance

In order to estimate the effect of the extra material on the tracking performance, we utilize a GEANT3-based full detector simulation that has also been used in the current Belle experiment. In this simulation the density parameters of the silicon sensors in the SVD and those of wires in the CDC are intentionally multiplied by a factor of two or three.

Single muons are generated at the coordinate origin in a random direction with a specific momentum (0.2 GeV/c, 0.5 GeV/c, 1.0 GeV/c and 2.0 GeV/c) and then are reconstructed by the standard Belle tracking algorithm, which is modified to correspond to each density case. Here, to clearly see the dependence on the amount of material, no beam background is assumed throughout this study. The effect of beam background on the tracking is discussed in section V.

Figures 51 and 52 show the relative resolution for the tracking parameters “ $dr$ ” and “ $dz$ ” with respect to the nominal density case, respectively. In each of the two figures, plot (a) corresponds to the case when the density of materials under consideration is multiplied by a factor of two, and plot (b) to the case when it is multiplied by a factor of three. The resolution degrades by 5% – 10% depending on the momentum for both “ $dr$ ” and “ $dz$ ” in case (a); 8% – 20% degradations are observed in case (b).

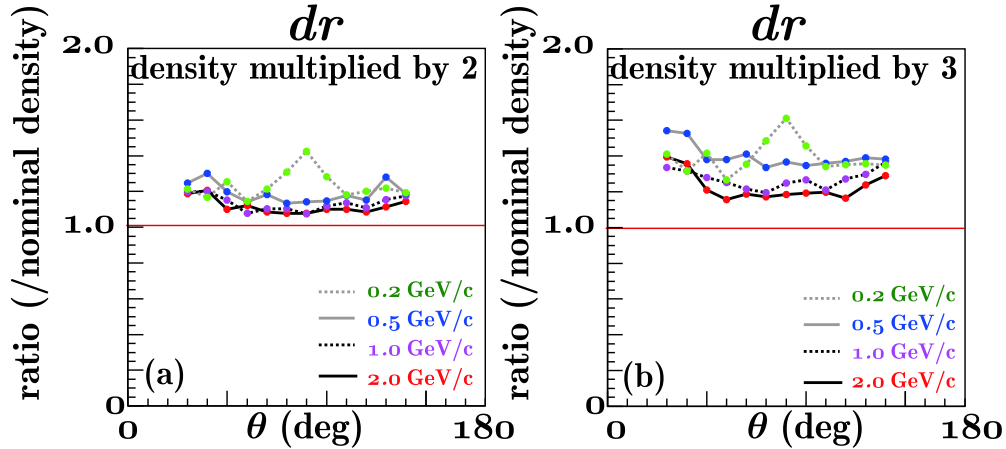


FIG. 51:  $dr$  resolution as a function of the polar angle relative to the beam axis, normalized to the corresponding resolution estimated in the nominal density case. The resolution degradation can be observed as the deviation from 1.0. Plots (a) and (b) correspond to the cases when the densities of the silicon sensors in the SVD and the wires in the CDC are increased by a factor of two and three, respectively.

Another tracking parameter, the transverse momentum component  $P_t$ , is also checked with the same conditions as above, but the transverse momentum of particle is fixed instead of the full momentum. The deviation of the reconstructed transverse momentum from the input value is plotted as a point in the Fig. 53 as a function of the polar angle relative to the beam axis. The relative resolution of the transverse momentum is also shown by the points with error bars. Although the reconstructed transverse momentum matches well to the input for relatively high momentum tracks, the resolution in the case when the density is increased by a factor of two

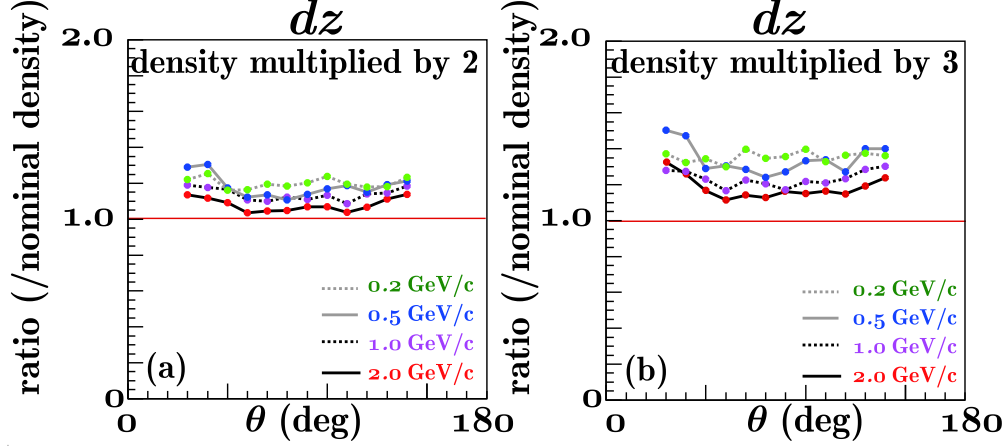


FIG. 52:  $dz$  resolution as a function of the polar angle relative to the beam axis, normalized to the corresponding resolution estimated in the nominal density case. The resolution degradation can be seen as the deviation from 1.0. Plots (a) and (b) correspond to the cases when the densities of the silicon sensors in the SVD and the wires in the CDC are increased by a factor of two and three, respectively.

(three) becomes 5% – 15% (15% – 30%) worse than in the case of nominal density, depending on the polar angle. For low momentum tracks, due to the energy loss in the SVD and CDC, a small bias (below 1%) is observed in the reconstructed transverse momentum, as shown in Fig. 53(a). In terms of the resolution, the degradation ranges from 4% – 20% depending on the polar angle, for the case when the density is increased by a factor of two.

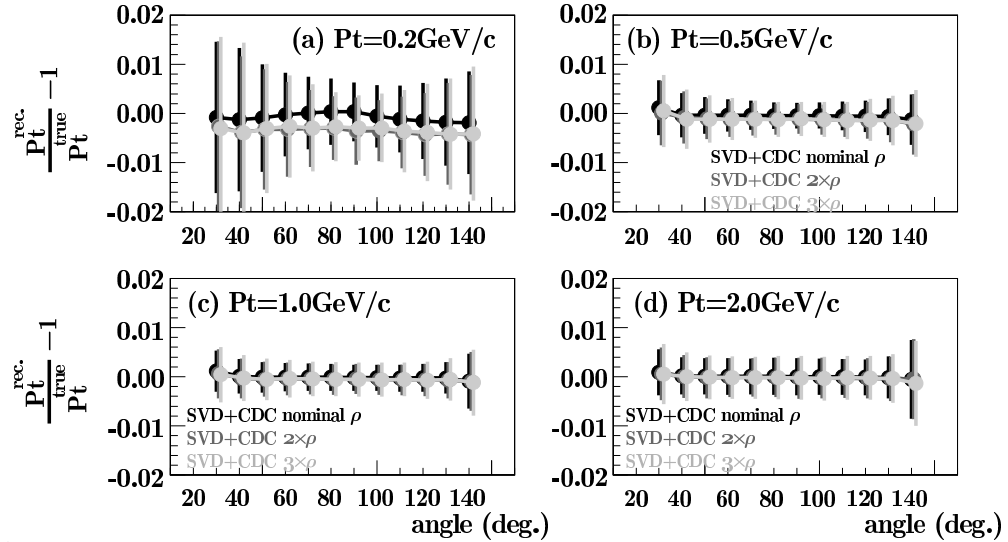


FIG. 53:  $P_t$  relative bias and resolution as a function of the polar angle relative to the beam axis. The difference between the reconstructed  $P_t$  and the input is shown as the deviation from 0.0. Black points and error bars correspond to the nominal density case. Dark gray (light gray) corresponds to the case when the densities of the silicon sensors in the SVD and the wires in the CDC are multiplied by a factor of two (three).

To summarize, for single muon tracks in the more realistic case when the amount of material increases by a factor of two, the  $dr$  and  $dz$  resolutions degrade by 5% – 10%, while the  $P_t$  resolution

TABLE XVIII: The deviation of the reconstructed  $P_t$  from the input and the resolution for the typical polar angle. Both are nomalized by the input  $P_t$ .

Case	$P_t = 0.2\text{GeV}/c$					
	40°deg		80°deg		130°deg	
	$P_t^{rec.}/P_t^{true} - 1$	res./ $P_t^{true}$	$P_t^{rec.}/P_t^{true} - 1$	res./ $P_t^{true}$	$P_t^{rec.}/P_t^{true} - 1$	res./ $P_t^{true}$
nominal $\rho$	-0.00127±0.00025	0.01460±0.00032	0.00039±0.00010	0.00674±0.00011	-0.00175±0.00015	0.00884±0.00016
$2 \times \rho$	-0.00383±0.00027	0.01543±0.00035	-0.00299±0.00010	0.00648±0.00010	-0.00409±0.00018	0.01035±0.00020
$3 \times \rho$	-0.00397±0.00024	0.01837±0.00039	-0.00268±0.00011	0.00703±0.00013	-0.00419±0.00020	0.01130±0.00019
Case	$P_t = 0.5\text{GeV}/c$					
	40°deg		80°deg		130°deg	
	$P_t^{rec.}/P_t^{true} - 1$	res./ $P_t^{true}$	$P_t^{rec.}/P_t^{true} - 1$	res./ $P_t^{true}$	$P_t^{rec.}/P_t^{true} - 1$	res./ $P_t^{true}$
nominal $\rho$	-0.00035±0.00008	0.00449±0.00007	-0.00045±0.00004	0.00271±0.00004	-0.00066±0.00006	0.00374±0.00005
$2 \times \rho$	-0.00081±0.00010	0.00531±0.00008	-0.00117±0.00005	0.00314±0.00004	-0.00138±0.00008	0.00448±0.00004
$3 \times \rho$	-0.00114±0.00011	0.00601±0.00009	-0.00121±0.00006	0.00358±0.00005	-0.00142±0.00009	0.00504±0.00007
Case	$P_t = 1.0\text{GeV}/c$					
	40°deg		80°deg		130°deg	
	$P_t^{rec.}/P_t^{true} - 1$	res./ $P_t^{true}$	$P_t^{rec.}/P_t^{true} - 1$	res./ $P_t^{true}$	$P_t^{rec.}/P_t^{true} - 1$	res./ $P_t^{true}$
nominal $\rho$	0.00010±0.00006	0.00349±0.00005	-0.00012±0.00004	0.00276±0.00003	-0.00023±0.00005	0.00323±0.00005
$2 \times \rho$	-0.00034±0.00008	0.00407±0.00006	-0.00055±0.00005	0.00310±0.00004	-0.00070±0.00007	0.00371±0.00005
$3 \times \rho$	-0.00026±0.00009	0.00471±0.00007	-0.00051±0.00005	0.00348±0.00004	-0.00054±0.00007	0.00432±0.00006
Case	$P_t = 2.0\text{GeV}/c$					
	40°deg		80°deg		130°deg	
	$P_t^{rec.}/P_t^{true} - 1$	res./ $P_t^{true}$	$P_t^{rec.}/P_t^{true} - 1$	res./ $P_t^{true}$	$P_t^{rec.}/P_t^{true} - 1$	res./ $P_t^{true}$
nominal $\rho$	0.00014±0.00007	0.00378±0.00005	0.00008±0.00006	0.00376±0.00005	-0.00015±0.00007	0.00429±0.00006
$2 \times \rho$	-0.00003±0.00008	0.00438±0.00005	-0.00014±0.00006	0.00402±0.00005	-0.00044±0.00008	0.00451±0.00006
$3 \times \rho$	-0.00003±0.00009	0.00496±0.00007	-0.00018±0.00007	0.00439±0.00006	-0.00038±0.00009	0.00497±0.00009

deteriorates by 5% – 15%. However, the more practical consequences of the increased material, such as the effect on the vertexing performance, should be checked in a high track-multiplicity environment. For this purpose, we examine the effect on the  $B$  vertex resolution with typical physics events we are interested in. This is discussed in the next subsection (IX A 2).

## 2. Vertexing Performance

First of all, to see the influence of the additional material located in the inner part of SVD, we use the modes  $B \rightarrow J/\Psi K_S^0$ ,  $B \rightarrow \pi^+\pi^-$  and  $B \rightarrow D^+D^-$  ( $D^\pm \rightarrow K^\mp \pi^\pm \pi^\pm$ ), since the  $CP$  side vertex can be reconstructed from charged particles produced in the vicinity of the interaction point. For the study of the first two physics modes, 50,000 events were simulated, while for the latter we used 100,000 simulated events, all without the beam background. Here the fitting parameters used in this study are the same as those defined in the subsection IV B.

The following simulation conditions are examined by modifying the GEANT3-based full detector simulation.

- (A) The densities of the silicon sensors in the SVD and the wires in the CDC are set to the nominal values.
- (B) The densities of the silicon sensors in the SVD and the wires in the CDC are multiplied by a factor of three
- (C) The densities of the silicon sensors in the SVD and the wires in the CDC are multiplied by a factor of two.
- (D) The density of the silicon sensors in the SVD is multiplied by a factor of two, but that of the wires in the CDC is set to the nominal value.
- (E) The density of the silicon sensors in the first and second innermost layers in the SVD is multiplied by a factor of two, while the densities of the other layers in the SVD and the wires in the CDC are unmodified.

- (F) The density of the silicon sensors in the two outermost layers (i.e., fourth and third layers) in the SVD is multiplied by a factor of two, while the densities of the other layers in the SVD and the wires in the CDC are unmodified.
- (G) The same as the condition for (F), with the addition of two  $4\text{mm} \times 4\text{mm}$  solid CFRP rods, which are attached on each silicon sensor to model the coolant materials for the chip-on-sensor as shown in Fig. 54.

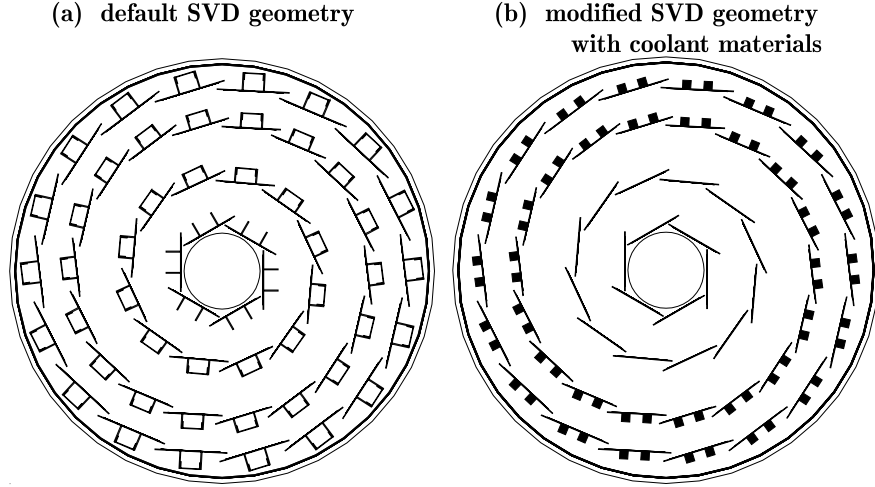


FIG. 54: (a) the  $r$ - $\phi$  view of the current SVD geometry, four layers of units, each of which is composed of several double-sided silicon strip detectors. The support materials, the so-called “ribs” made from “Zylon”, are attached on each unit to reinforce the unit structure. The effect of the material in the “ribs” is negligible. (b) the modified SVD geometry by replacing the “ribs” on the third and outermost layer with two cooling tubes made from CFRP.

Figure 55 shows the fitted vertex resolutions for case(A) (left) and (B) (right). Tables XIX and XX also show the vertex resolution and the efficiency for each case listed above. Moreover the estimated  $\Delta z$  vertex resolution for each mode is summarized in Table XXI.

These results imply that the additional material in the CDC does not affect the vertex resolution at all. Another crucial point is that, as expected, the material in the innermost and the second SVD layers degrades the vertex resolution while those in the outermost and third layers do not affect it. Furthermore, the effect of the material attached to the outer layers such as the coolant is not large. The reconstruction efficiency including the vertexing efficiency decreases at most by roughly 6% because of the extra material. Note, however, that it is expected that this loss can be partially recovered from the SVD stand-alone tracking (under development). This is especially important for the  $B \rightarrow D^+ D^-$  mode.

Therefore, the chip-on-sensor on the outer layers is a possible technology for the vertex detector as far as the physics modes discussed above are concerned. However, a chip-on-sensor for the inner layers does not seem to be a viable solution.

As a next step, the  $B$  vertex resolution of a mode that could be more sensitive to the material in the SVD outer layers has to be checked. For this purpose, we use the  $B \rightarrow K^{*0} \gamma (K^{*0} \rightarrow K_S^0 \pi^0)$  decay mode. One reason is that only two charged pions from the  $K_S^0$  decay can be used for the  $B$  vertex reconstruction, and in addition we require at least two SVD hits to reconstruct the  $K_S^0$ . That is, the  $B$  vertex of some events could be reconstructed from two tracks, each of which has only

TABLE XIX:  $CP$  side vertex resolution. (A)-(G) are explained in the text.  $\downarrow$  and  $\uparrow$  represent the degradation and improvement, respectively. The relative degradation or improvement with respect to the nominal density case is also shown.

Case	$B \rightarrow \pi^+\pi^-$		$B \rightarrow J/\Psi K_S^0$		$B \rightarrow D^+D^-$	
	res. ( $\mu\text{m}$ )	# of events	res. ( $\mu\text{m}$ )	# of events	res. ( $\mu\text{m}$ )	# of events
(A) nominal $\rho$	$31.4 \pm 0.3$ —	38,731 —	$35.6 \pm 0.4$ —	24,859 —	$43.0 \pm 0.6$ —	13,225 —
(B) $3 \times \rho$ : all SVD & CDC layers	$35.4 \pm 0.3$ 13% $\downarrow$	36,268 6.4% $\downarrow$	$44.5 \pm 0.5$ 25% $\downarrow$	23,853 4.0% $\downarrow$	$57.6 \pm 1.0$ 34% $\downarrow$	11,777 10.9% $\downarrow$
(C) $2 \times \rho$ : all SVD & CDC layers	$33.5 \pm 0.3$ 7% $\downarrow$	37,441 3.3% $\downarrow$	$40.0 \pm 0.4$ 12% $\downarrow$	24,369 2.0% $\downarrow$	$51.2 \pm 0.8$ 19% $\downarrow$	12,366 6.5% $\downarrow$
(D) $2 \times \rho$ : all SVD layers only	$33.0 \pm 0.3$ 5% $\downarrow$	38,153 1.5% $\downarrow$	$40.1 \pm 0.4$ 13% $\downarrow$	24,316 2.2% $\downarrow$	$51.6 \pm 0.8$ 20% $\downarrow$	12,520 5.3% $\downarrow$
(E) $2 \times \rho$ : SVD 1st & 2nd layers only	$33.7 \pm 0.3$ 7% $\downarrow$	38,289 1.1% $\downarrow$	$40.0 \pm 0.4$ 12% $\downarrow$	24,556 1.2% $\downarrow$	$50.6 \pm 0.8$ 18% $\downarrow$	12,713 3.9% $\downarrow$
(F) $2 \times \rho$ : SVD 3rd & 4th layers only	$31.3 \pm 0.3$ —	38,162 1.5% $\downarrow$	$36.5 \pm 0.4$ 3% $\downarrow$	24,534 1.3% $\downarrow$	$41.6 \pm 0.6$ 3% $\uparrow$	12,559 5.0% $\downarrow$
(G) assumption (F) + cooling tubes	$30.3 \pm 0.3$ 4% $\uparrow$	37,901 2.1% $\downarrow$	$35.3 \pm 0.4$ —	24,221 2.6% $\downarrow$	$43.5 \pm 0.7$ 1% $\downarrow$	12,388 6.3% $\downarrow$

TABLE XX: The tagging side vertex resolution. (A)-(G) are explained in the text.  $\downarrow$  and  $\uparrow$  represent the degradation and improvement, respectively. The relative degradation or improvement with respect to the nominal density case is also shown.

Case	$B \rightarrow \pi^+\pi^-$		$B \rightarrow J/\Psi K_S^0$		$B \rightarrow D^+D^-$	
	res. ( $\mu\text{m}$ )	# of events	res. ( $\mu\text{m}$ )	# of events	res. ( $\mu\text{m}$ )	# of events
(A) nominal $\rho$	$108.6 \pm 1.1$ —	25,892 —	$108.8 \pm 1.4$ —	15,833 —	$111.0 \pm 1.9$ —	8,564 —
(B) $3 \times \rho$ : all SVD & CDC layers	$124.7 \pm 1.3$ 15% $\downarrow$	24,495 5.4% $\downarrow$	$125.2 \pm 1.6$ 15% $\downarrow$	15,344 3.1% $\downarrow$	$124.4 \pm 2.2$ 12% $\downarrow$	7,729 9.8% $\downarrow$
(C) $2 \times \rho$ : all SVD & CDC layers	$119.4 \pm 1.2$ 10% $\downarrow$	25,127 3.0% $\downarrow$	$116.6 \pm 1.5$ 7% $\downarrow$	15,715 0.7% $\downarrow$	$115.0 \pm 1.8$ 4% $\downarrow$	7,989 6.7% $\downarrow$
(D) $2 \times \rho$ : all SVD layers only	$120.2 \pm 1.2$ 11% $\downarrow$	25,609 1.1% $\downarrow$	$118.3 \pm 1.6$ 9% $\downarrow$	15,487 2.2% $\downarrow$	$113.3 \pm 1.9$ 2% $\downarrow$	8,123 5.1% $\downarrow$
(E) $2 \times \rho$ : SVD 1st & 2nd layers only	$119.9 \pm 1.2$ 10% $\downarrow$	25,585 1.2% $\downarrow$	$116.5 \pm 1.4$ 7% $\downarrow$	15,619 1.4% $\downarrow$	$119.1 \pm 2.1$ 7% $\downarrow$	8,301 3.1% $\downarrow$
(F) $2 \times \rho$ : SVD 3rd & 4th layers only	$109.9 \pm 1.1$ 1% $\downarrow$	25,372 2.0% $\downarrow$	$108.7 \pm 1.4$ —	15,590 1.5% $\downarrow$	$107.6 \pm 1.7$ 3% $\uparrow$	8,128 5.1% $\downarrow$
(G) assumption (F) + cooling tubes	$109.0 \pm 0.4$ —	25,322 2.2% $\downarrow$	$106.4 \pm 1.3$ 2% $\uparrow$	15,458 2.4% $\downarrow$	$106.0 \pm 1.8$ 5% $\uparrow$	8,044 6.1% $\downarrow$



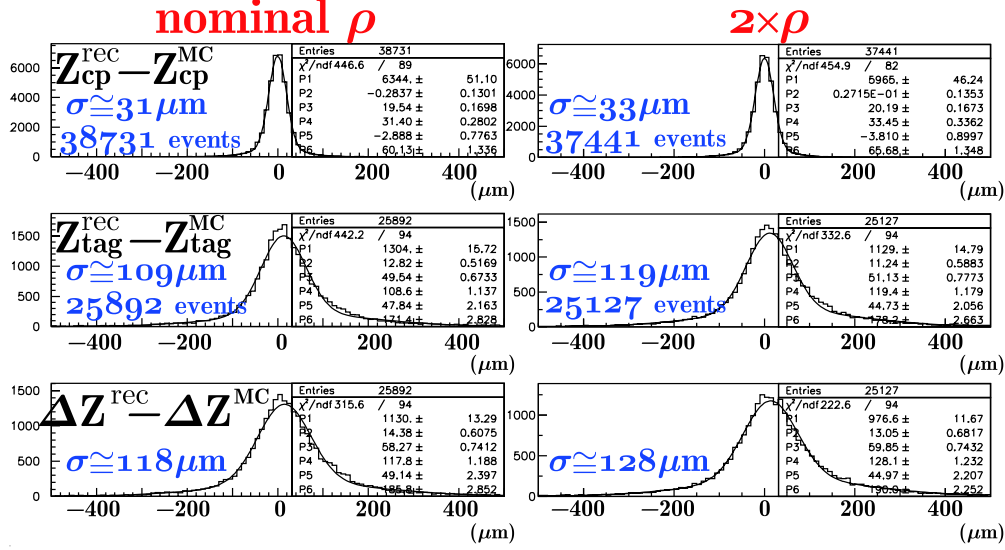


FIG. 55: Distributions of the vertex resolution for different simulation conditions. From top to bottom, the three histograms show the distributions of the difference between the reconstructed  $B$  decay vertex and true decay point for  $CP$ -side (upper), tagging-side (middle) and the difference of the displacement for the two  $B$  decay vertices from the true value (lower). The results for the nominal density case are shown in the left column and the case that the density under consideration is increased by a factor two is shown on the right.

two SVD hits in the outer layers. Therefore, the additional material in the outer part of the SVD, e.g., the chip-on-sensor, could affect the  $B$  vertex resolution for this mode.

The simulation studies for cases (A) and (G) are done in the same way. Table XXII shows the  $CP$  side vertex resolutions for each case. The averaged vertex resolution for the case (G) is degraded by roughly 7% from the nominal density case (A). To clearly see the impact of the material in the SVD outer layers, the reconstructed events are categorized according to the SVD hit pattern. When events are reconstructed by requiring SVD hits in all four layers for each track the vertex resolution for the case (G) is consistent to that for the nominal density case (A) (See “hits in all lyrs” in Table XXII). On the other hand, in cases where SVD hits are required only in the third and fourth layers for each track, the vertex resolution degrades by  $\sim 15\%$  (See “hits in 3 & 4 lyrs” in Table XXII).

From this study an increase in the material in the SVD outer layers is found to be undesirable. However, without applying the chip-on-sensor technique on the outer layers, the S/N ratio could degrade by a factor of four and then the SVD-CDC track-matching efficiency for the tracks from  $K_S^0$  would become much worse as discussed in subsection IVD. Therefore we have to make a compromise.

In conclusion, the amount of material in the outer layers of SVD has to be increased in order to maintain a good S/N ratio, and as a consequence the vertex resolution for the  $B \rightarrow K^{*0}\gamma$  decay channel degrades by 7% on average. For the other physics modes,  $B \rightarrow J/\Psi K_S^0$ ,  $B \rightarrow \pi^+\pi^-$  and  $B \rightarrow D^+D^-$ , the vertex resolution is mainly degraded by the material in the SVD inner layers. Therefore, it is strongly recommended that the amount of material in the innermost and second layers should be minimized.

TABLE XXI:  $\Delta z$  vertex resolution. (A)-(G) are explained in the text.  $\downarrow$  and  $\uparrow$  represent the degradation and improvement, respectively. The relative degradation or improvement with respect to the nominal density case is also shown.

Case	$B \rightarrow \pi^+\pi^-$	$B \rightarrow J/\Psi K_S^0$	$B \rightarrow D^+D^-$
	res. ( $\mu\text{m}$ )	res. ( $\mu\text{m}$ )	res. ( $\mu\text{m}$ )
(A) nominal $\rho$	$117.8 \pm 1.2$ —	$117.8 \pm 1.4$ —	$123.8 \pm 2.0$ —
(B) $3 \times \rho$ : all SVD & CDC layers	$133.0 \pm 1.3$ 13% $\downarrow$	$137.6 \pm 1.6$ 17% $\downarrow$	$147.5 \pm 2.7$ 19% $\downarrow$
(C) $2 \times \rho$ : all SVD & CDC layers	$128.1 \pm 1.2$ 9% $\downarrow$	$127.3 \pm 1.6$ 8% $\downarrow$	$134.1 \pm 2.8$ 8% $\downarrow$
(D) $2 \times \rho$ : all SVD layers only	$128.5 \pm 0.5$ 9% $\downarrow$	$126.5 \pm 1.6$ 7% $\downarrow$	$129.9 \pm 2.2$ 5% $\downarrow$
(E) $2 \times \rho$ : SVD 1st & 2nd layers only	$127.2 \pm 1.2$ 8% $\downarrow$	$127.1 \pm 3.0$ 8% $\downarrow$	$135.7 \pm 1.8$ 10% $\downarrow$
(F) $2 \times \rho$ : SVD 3rd & 4th layers only	$117.3 \pm 1.2$ —	$118.9 \pm 1.5$ 1% $\downarrow$	$121.6 \pm 1.8$ 2% $\uparrow$
(G) assumption (F) + cooling tubes	$116.4 \pm 1.1$ 1% $\uparrow$	$116.4 \pm 1.4$ 1% $\uparrow$	$122.5 \pm 2.0$ 1% $\uparrow$

TABLE XXII:  $CP$  side vertex resolution for  $B \rightarrow K^{*0}\gamma$  decay. (A) and (G) are explained in the text. The results are still preliminary.

Case	$B \rightarrow K^{*0}\gamma$		
	$\geq 2$ lyr hits.	hits in all lyrs	hits in 3 & 4 lyrs
(A) nominal $\rho$	$128 \pm 2$ ( $\mu\text{m}$ ) —	$78 \pm 2$ ( $\mu\text{m}$ ) —	$163 \pm 4$ ( $\mu\text{m}$ ) —
(G) $2 \times \rho$ : SVD 3rd & 4th layers only + coolant	$137 \pm 2$ ( $\mu\text{m}$ ) 7% $\downarrow$	$77 \pm 2$ ( $\mu\text{m}$ ) —	$188 \pm 6$ ( $\mu\text{m}$ ) 15% $\downarrow$

### 3. Effect of the additional layers

To improve the reconstruction efficiency for the  $B \rightarrow K^{*0}\gamma$  decay, we decided to extend the SVD volume in radial direction from the current 4-layer configuration to a 6-layer one. This implies that the amount of the material corresponding to the additional two layers increases. In this section, another simulation study is carried out by modifying the GEANT3-based full detector simulator.

As shown in Fig. 56, the geometry implemented in the current detector simulator is modified for this purpose. The three inner CDC layers are removed and then the new extra two SVD layers are installed in the extended SVD volume. The fifth and sixth layer are located 13 cm and 14 cm from the interaction point in the radial direction, respectively, while the first to the fourth layers remain in their current positions. The 30 additional silicon sensor units of the same type as used for the fourth layer, are placed so that they cover the fourth layer without any gaps in the acceptance.

In this study we assume that the density of the silicon sensors is not modified at all, i.e., they are the nominal density. The thickness of each silicon sensor is set to  $300\text{ }\mu\text{m}$ , which is the same as the silicon sensors installed in the current SVD.

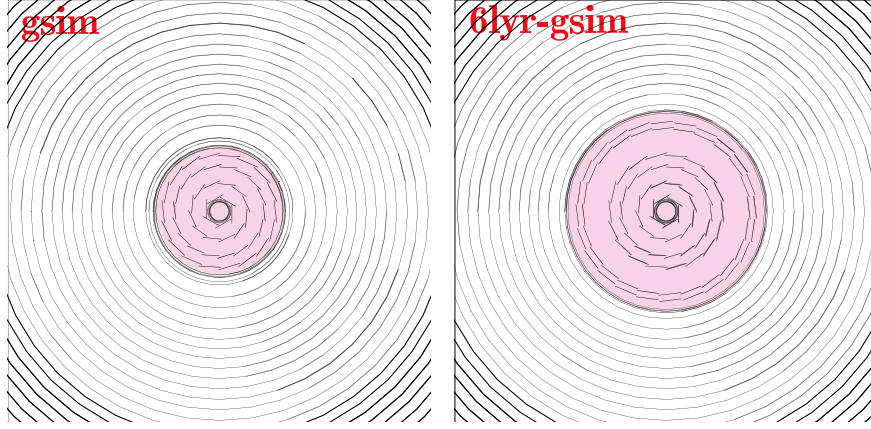


FIG. 56: The figure on the left is the current SVD, which consists of 4 layers. The figure on the right is the 6-layer SVD configuration in which the three inner CDC layers are replaced by two new SVD layers.

The same physics modes are investigated as in the previous section. The resolutions for the  $CP$  and tagging side vertices are evaluated in the same way and summarized in Table XXIII. In this case, no degradation is observed in the vertex resolution. That is, the extra material corresponding to the additional two SVD layers does not change the vertex resolution. The  $B$  vertex resolution for  $B \rightarrow K^{*0}\gamma$  decay with the 6-layer SVD is discussed in the SVD section, because this is related to the optimization of the fifth layer position.

TABLE XXIII:  $CP$  and tagging side vertex resolutions for  $B \rightarrow J/\Psi K_S^0$ ,  $B \rightarrow \pi^+\pi^-$  and  $B \rightarrow D^+D^-$ .

Case	$B \rightarrow \pi^+\pi^-$		$B \rightarrow J/\Psi K_S^0$		$B \rightarrow D^+D^-$	
	$CP\text{ }(\mu\text{m})$	tagging $(\mu\text{m})$	$CP\text{ }(\mu\text{m})$	tagging $(\mu\text{m})$	$CP\text{ }(\mu\text{m})$	tagging $(\mu\text{m})$
default	$31.4 \pm 0.3$	$108.6 \pm 1.1$	$35.8 \pm 0.4$	$108.8 \pm 1.4$	$43.0 \pm 0.6$	$111.0 \pm 1.9$
6-lyr.	$28.5 \pm 0.2$	$106.2 \pm 1.1$	$33.8 \pm 0.3$	$104.6 \pm 1.4$	$40.0 \pm 0.6$	$99.2 \pm 1.7$

## B. Calorimetry

The effect of material on the efficiencies of photons and  $\pi^0$ s are studied using the full simulation described in the previous section. Here the densities of materials in the tracking devices (SVD and CDC) are multiplied by a factor of three to conservatively account for the increase in material due to the upgrade. An A-RICH detector is assumed for the upgraded endcap PID device, while a TOP counter replaces the current barrel ACC and TOF counters. Two types of TOP counter geometry were tested. One has no geometrical overlap between adjacent quartz bars (sBelle geometry) while the bars overlap in the other geometry (sBelle2); these two geometries are shown in Fig. 57.

Single particle Monte Carlo events are generated for photons and  $\pi^0$ s. Beam-induced background data obtained in experiment 49 are overlaid on the event. Generated events are processed with the standard photon and  $\pi^0$  finders.

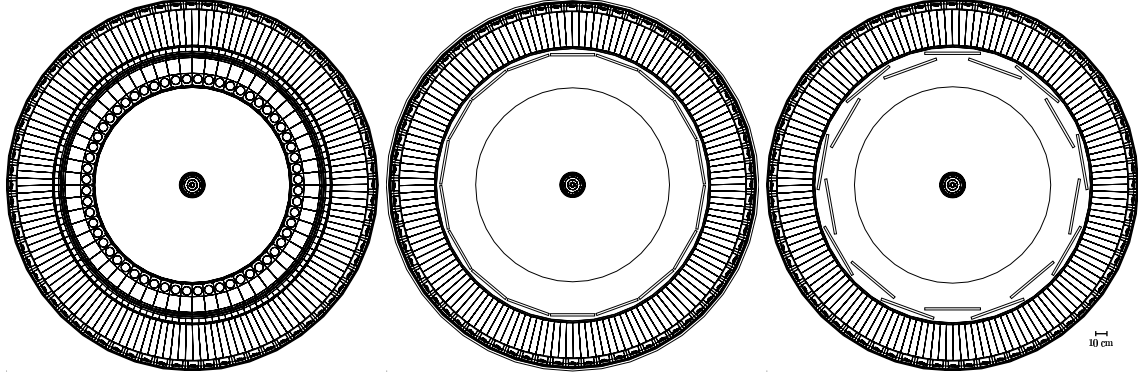


FIG. 57: Barrel PID configurations that were tested to determine the effect of additional material on calorimetry. From left to right, the ACC of Belle, single inlined TOP and staggered TOP.

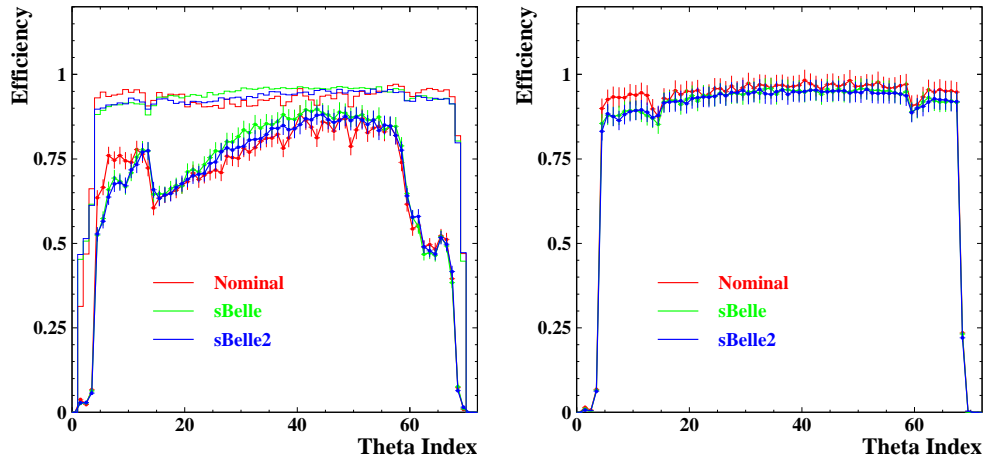


FIG. 58: Photon finding efficiencies as functions of  $\theta$  indices of the calorimeter cell for 100 MeV (Left) and 1 GeV (Right) photons. Open histograms in the left figure show the cluster finding efficiency before photon selection.

Figure 58 shows the photon finding efficiencies for 100 MeV and 1 GeV photons. Three different colors correspond to the three detector configurations. As one can imagine, the efficiency depends on the amount of material. The efficiency for the barrel increases slightly as the amount of material decreases, while the efficiency for the forward endcap decreases because of the extra material in the CDC end plate. Although there are changes due to material, the effect is not very large.

Figure 59 shows the  $\pi^0$  finding efficiencies for 100 MeV and 1 GeV  $\pi^0$ s for combinations of detector regions. One finds that the tendencies are the same as those for photons.

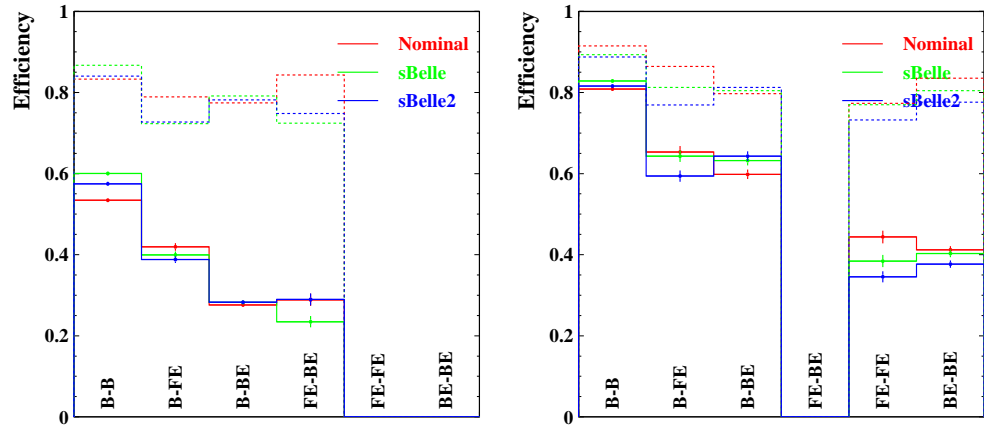


FIG. 59:  $\pi^0$  finding efficiencies for 100 MeV(Left) and 1 GeV(Right)  $\pi^0$ s as functions of combinations of detector regions B(barrel), FE(forward endcap) and BE(backward endcap). The dotted histograms show the efficiency to find two clusters for the two photons from a  $\pi^0$ .

## X. BEAM ENERGY ASYMMETRY

A larger beam energy asymmetry provides larger boost to the  $\Upsilon(4S)$  system with respect to the laboratory frame so that the produced  $B$  meson pair travels further along the beam axis, which allows us to measure the decay time difference ( $\Delta t$ ) between the two  $B$  mesons with higher precision. On the other hand, the additional boost distorts the solid angle, which is uniform in the center-of-mass frame, when seen in the laboratory frame. We place the detectors as close to the beam axis as possible to cover more solid angle with sensitive devices, however, there must be gaps around the beam axis in order to allow the beam and the SR to pass through as well as accommodate the readout electronics and cables from the sensors. Therefore, a larger boost will reduce the total detector coverage, which is not beneficial to any of the analyses.

When the energy asymmetry of the present KEKB was determined, discussions were based on the impact in the  $\sin 2\phi_1$  measurement with  $B^0 \rightarrow J/\psi K_S^0$ , which was the critical measurement in the early stages of the Belle experiment. Now, the  $\sin 2\phi_1$  measurement is already a precision measurement, and there are other important analyses that will be the focus in the sBelle era.

One such analysis is the time-dependent  $CP$  asymmetry measurement in  $B^0 \rightarrow \phi K_S^0$  and related decay modes to search for the effect of new physics. Since this analysis needs good  $\Delta t$  resolution, the optimal beam energy asymmetry is similar to the case of  $B^0 \rightarrow J/\psi K_S^0$ . Analyses that include neutrinos in the final state such as  $B \rightarrow \tau\nu$ ,  $B \rightarrow K\nu\nu$ , and  $B \rightarrow D^*\tau\nu$  are also important. Since detector inefficiency is the source of the peaking background in these modes that drastically degrades the sensitivity, better hermeticity is desired, while better  $\Delta t$  resolution is not required.

In the subsections X A and X B, physics sensitivities for  $B^0 \rightarrow \phi K_S^0$  and  $B \rightarrow \tau\nu$  are examined for various energy asymmetry cases. A summary is given in subsection X C.

### A. $B^0 \rightarrow \phi K_S^0$ and the beam energy asymmetry

For the time-dependent  $CP$  asymmetry measurement, the most important variable is the quantity  $\Delta t$ . Better  $\Delta t$  resolution is also important for extracting  $B^0 \rightarrow \phi K_S^0$  signals from the large  $e^+e^- \rightarrow q\bar{q}$  continuum background. This is because the signal events decay with a finite lifetime of 1.5 ps, while the  $q\bar{q}$  background events decay promptly. So far, we have achieved a  $\Delta t$  resolution of 1.4 ps with the current Belle detector. This corresponds to a  $\Delta z$  resolution of about 180  $\mu\text{m}$  with a  $\beta\gamma$  of 0.425 in asymmetric collisions of 3.5 GeV positrons (LER) on 8.0 GeV electrons (HER).

We study the sensitivity of the  $CP$  asymmetry measurement in  $B^0 \rightarrow \phi K_S^0$  and  $J/\psi K_S^0$  decays for various energy asymmetries with toy MC experiments. We evaluate the cases of  $\beta\gamma = 0.56, 0.425, 0.38$  and  $0.34$ , corresponding to LER $\times$ HER energies of  $3.1 \times 9.0, 3.5 \times 8.0, 3.65 \times 7.67$  and  $3.8 \times 7.36$ . The  $\Delta z$  resolutions and the S/N ratios are fixed to the values obtained from the Belle analysis using 492 fb $^{-1}$  of data[25]. The change in the detector acceptance due to the change of the boost factor is also considered.

The sensitivity is shown as the solid red line for  $B \rightarrow \phi K_S^0$  and the blue dashed line for  $B \rightarrow J/\psi K_S^0$  in Fig. 60. The vertical axis shows the ratio of the luminosity to obtain the same sensitivity with the current Belle boost. The smaller value corresponds to the better sensitivity.

TABLE XXIV: The ratio of the full-reconstruction tagging efficiency and the peaking BG for  $B \rightarrow \tau \bar{\nu}$  depending on the LER energy.

Full-rec. eff.	$1.09 \pm 0.01$	$1.05 \pm 0.01$	$1.02 \pm 0.01$	1	$0.92 \pm 0.01$	$0.86 \pm 0.01$
Peaking BG	$0.90 \pm 0.04$	$0.96 \pm 0.04$	$0.98 \pm 0.04$	1	$0.86 \pm 0.04$	$1.04 \pm 0.04$
$E_{LER}$	4.1	3.8	3.65	3.5	3.1	2.9

### B. $B \rightarrow \tau \nu$ and the beam energy asymmetry

For the  $B \rightarrow \tau \nu$  analysis, detection of all particles from the two  $B$  decays except for neutrinos is required; the absence of additional energy clusters in the ECL is the identifying feature of the signal. The most significant effect of changing the boost factor is the change of the detector acceptance. Figure 61 shows the size of the hole in the acceptance in the forward side of the Belle detector depending on the LER energy. At an LER energy of 3 GeV that is better for time-dependent  $CP$  asymmetry measurement, the hole becomes about 20% larger compared to the case of the present Belle detector, which is not optimal for the  $B \rightarrow \tau \nu$  analysis.

There are two major effects from the change of the detector acceptance. One is the detection efficiency of the tagging-side  $B$  that is fully reconstructed in hadronic  $B$  decays. Another is the peaking background fraction in the remaining ECL energy distribution from the loss of ECL energy cluster reconstruction. We study the change in the full-reconstruction efficiency of the tagging-side  $B$  based on the geometrical acceptance. We assume the reconstruction efficiency of the tagging  $B$  is uniform in the detector acceptance and only examined the distribution at the generator level. The effect of decreasing the detector acceptance on the peaking background fraction is studied using a gsim MC event sample of generic  $B$  decays. For a variety of boost factors, we examine each ECL cluster if it is inside the detector acceptance and estimate the change in the number of events remaining in the ECL energy signal region. The effect on the peaking background fraction from an increase of the detector acceptance is also studied using a toy MC and using the gsim event sample in the ECL signal region of generic  $B$  decays. If there are  $\gamma$ 's in the MC generator information inside of the detector acceptance for a given boost factor, we add the  $\gamma$  energy to the ECL energy based on the reconstruction efficiency obtained from gsim. We then count the number of events remaining in the ECL signal region. Table XXIV shows the ratios of the full-reconstruction tagging efficiencies and the peaking backgrounds to the current Belle boost. The sensitivity in terms of the required luminosity ratio is shown as the purple dotted line in Fig. 60.

### C. Summary of the beam energy asymmetry studies

Figure 60 shows the improvement for one mode results in the loss of the sensitivity for the other mode by a similar amount. If both modes are equally important, we conclude that the current beam energy asymmetry is the best point.



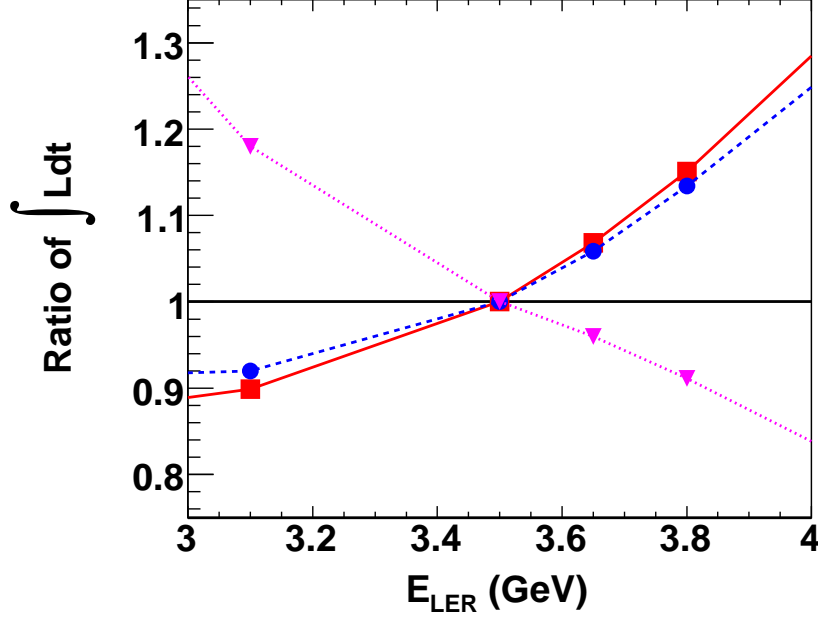


FIG. 60: The sensitivity dependence on the boost factor corresponding to the LER energy. The purple dotted line is the sensitivity for  $B \rightarrow \tau\nu$ , the blue dashed line is for  $B \rightarrow J\psi K_S^0$  and the red line is for  $B \rightarrow \phi K_S^0$ . In the vertical axis is the luminosity ratio to achieve the same sensitivity (smaller is the better).

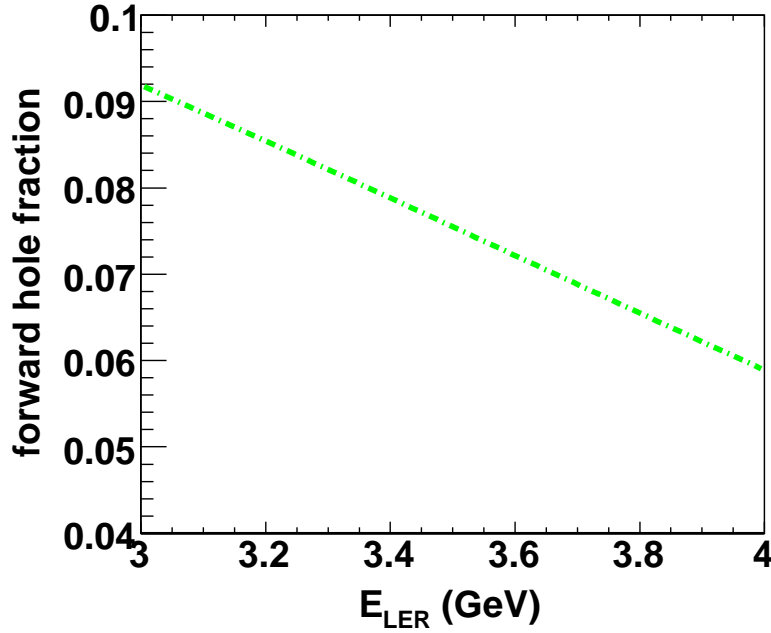


FIG. 61: The dependence of the size of the forward hole in the detector acceptance on the boost factor in terms of LER energy.

## XI. CLOSING REMARKS

Extensive simulation studies have been performed to evaluate the impact of various detector upgrade options and related parameters on several important physics analyses. Studies are based on the current best knowledge of the expected beam background, which is extrapolated from ten years of Belle operation.

This report concentrates on the baseline design that we had when we started this activity in the spring of 2007. There are, in fact, more studies done, but not included in this report. As an example, the detector hermeticity will be extremely important for the analyses that include neutrinos in the final states. The impact of a silicon-based tracker in the very low angle regions in the forward and the backward direction has been studied; these show that an ILC-FCAL-like detector could be very important. Another missing item in this report is a study of a pixel detector. Since we had no feasible option for day one, we did not include the pixel detector in the baseline design. The missing topics as well as updates especially in the background simulation that are consistent with the latest design of the IR will be included in a separate report, or possibly in the technical design report (TDR).

Most of the studies are performed with tentative versions of the sBelle simulator such as an integrated toy simulator and several modified versions of the Belle's full simulator. An integrated full simulator of the sBelle is being prepared, which will be used for studies toward the TDR. Studies in this report will be updated in the TDR; nevertheless, this report provides a clear direction for the pre-TDR design of the sBelle detector. We hope that this report will be helpful for each detector subsystem.

- 
- [1] K. Abe *et al.*, KEK Report 2004-4, "Letter of Intent for KEK Super B Factory", (2004).
  - [2] M. Nakao, C. Schwanda *et al.*, sBN/0002.
  - [3] Particle Data Group <http://pdg.lbl.gov>
  - [4] R. Kleiss, H. Burkhardt, *Comput.Phys.Commun.* **81**, 372-380, (1994).
  - [5] <http://www.geant4.org/geant4/>
  - [6] M. Akatsu *et al.*, *Nucl. Instr. and Meth. A* 440 (2000) 124;  
T. Ohshima, *ICFA Instr. Bull.* 20 (2000) 2;  
T. Ohshima, *Nucl. Instr. and Meth. A* 453 (2000) 331;  
M. Hirose *et al.*, *Nucl. Instr. and Meth. A* 460 (2001) 326;  
S. Matsui *et al.*, *Nucl. Instr. and Meth. A* 463 (2001) 220;  
T. Hokuue *et al.*, *Nucl. Instr. and Meth. A* 494 (2002) 436;  
Y. Enari *et al.*, *Nucl. Instr. and Meth. A* 494 (2002) 430;  
M. Akatsu *et al.*, *Nucl. Instr. and Meth. A* 502 (2003) 133;  
P. Coyle *et al.*, *Nucl. Instr. and Meth. A* 343 (1994) 292;  
M. Selen and K. Honscheid, *Nucl. Instr. and Meth. A* 343 (1994) 306.
  - [7] H. Kichimi, H. Sagawa, Y. Yoshimura, T. Kishida, N. Tamura, H. Suzuki and T. Taguchi, *Nucl. Instrum. Meth. A* **325**, 451 (1993).
  - [8] C. Gustavino, A. Candela, M. De Deo, M. D'Incecco, N. Redaelli, A. Tonazzo and G. C. Trincherio, *Nucl. Instrum. Meth. A* **527**, 471 (2004).
  - [9] G. Bondarenko *et al.*, *Nucl. Phys. Proc. Suppl.* **61B** 347 (1998);  
G. Bondarenko *et al.*, *Nucl. Instr. Meth.* **A442** 187 (2000).

- [10] W. Innes, TRACKERR: a program for calculating tracking errors, Tech. Rep. SLAC-BABAR-Note-121, 1993.
- [11] Y. Kuroki, thesis for master's degree : "Performance Evaluation of Readout Chip for Silicon Vertex Detector for SuperBelle", <http://osksn2.hep.sci.osaka-u.ac.jp/theses/master/2007/kurokimthesis.pdf>
- [12] T. Kawasaki *et al.*, Nuclear Science, IEEE Transactions on, Vol. 44, Issue: 3, Part 1, p708-712 (1997).
- [13] K. Abe *et al.* (Belle Collaboration), Phys. Rev. D **66**, 032007 (2002).
- [14] H. Miyake, M. Hazumi *et al.* (Belle Collaboration), Phys. Lett. B **618**, 34 (2005).
- [15] I. Adam *et al.* [BABAR-DIRC Collaboration], Nucl. Instr. and Meth. A 538 (2005) 281.
- [16] M. Akatsu *et al.*, Nucl. Instr. and Meth. A 528 (2004) 763.
- [17] N. Kishimoto *et al.*, Nucl. Instr. and Meth. A 564 (2006) 204.
- [18] T. Matsumoto *et al.*, Nucl. Instr. and Meth. A 521 (2004) 367; P. Križan *et al.*, Nucl. Instr. and Meth. A 533 (2005) 58.
- [19] T. Iijima, S. Korpar *et al.*, Nucl. Instr. and Meth. A 548 (2005) 383.
- [20] P. Križan, Super B Factory Workshop, 19-22 Jan 2004, Honolulu, Hawaii, <http://www.phys.hawaii.edu/superb04>.
- [21] A. Danilyuk *et al.*, Nucl. Instr. and Meth. A 533 (2005) 70.
- [22] P. Križan, S. Korpar, T. Iijima, Nucl. Instr. and Meth. A 565 (2006) 457.
- [23] I. Adachi *et al.*, Nucl. Instr. and Meth. A 533 (2005) 146.
- [24] R. Pestotnik *et al.*, Proceedings of the RICH07 symposium, Trieste 2007, to be published in Nucl. Instrum. Meth. A.
- [25] K. F. Chen *et al.* [Belle Collaboration], Phys. Rev. Lett. **98**, 031802 (2007) [arXiv:hep-ex/0608039].
- [26] H. Ozaki, Belle Note # 111 (1996).